



Technical University of Munich

Using high-resolution optical satellite imagery
to observe glaciers and rock glaciers
in Northern Tien Shan, Central Asia

Master's Thesis

Alexandra Strel

Matriculation number: 03658149

Course of Study: Cartography M.Sc.

Date Submitted: May 29, 2017

Supervisors:

Dr. habil. Tobias Bolch (University of Zurich)

Dr. Holger Kumke (Technical University of Munich)

STATEMENT OF AUTHORSHIP

I hereby declare that the thesis submitted is my own unaided work. All direct or indirect sources used are acknowledged as references.

I am aware that the thesis in digital form can be examined for the use of unauthorized aid and in order to determine whether the thesis as a whole or parts incorporated in it may be deemed as plagiarism. For the comparison of my work with existing sources I agree that it shall be entered in a database where it shall also remain after examination, to enable comparison with future theses submitted. Further rights of reproduction and usage, however, are not granted here.

This paper was not previously presented to another examination board and has not been published.

Munich 28.05.2017

Place and date



Signature

ABSTRACT

Glaciers and rock glaciers are important features in the Northern Tien Shan mountains, where they contribute to dry-season water resources and are also related to a number of natural hazards. The investigated study area (42.92°-43.14°N, 76.93°-77.21°E) in the Ile Alatau range, at the border of Kazakhstan and Kyrgyzstan, contains a high concentration of rock glaciers, and is situated immediately upstream of a large urban population. High-resolution optical stereo satellite imagery from 1971 (CORONA), 2012 (GeoEye-1), and 2016 (Pléiades) was used to generate orthoimages and digital elevation models, allowing for both long-term and recent change detection of glaciers and rock glaciers. Glacier area change was negative throughout the study area with a relative area loss of almost 30% over the 45-year time span (1971-2016). The recent relative average annual area change was more than double the average of the 1971-2012 time period. Geodetic mass balance was -0.34 ± 0.14 m w.e. a^{-1} (1971-2012) and -0.62 ± 0.43 m w.e. a^{-1} (2012-2016), again showing an increased rate of change in recent years. Compared to in situ mass balance measurements at Tuyuksu Glacier, these results underestimate mass change by 35% (1971-2012) and overestimate by 37% (2012-2016). Compared to the rapid retreat of glaciers, the 57 identified rock glaciers in the study area have remained relatively stable with average surface elevation change of -1.51 ± 6.30 m (1971-2016). Surface lowering of rock glaciers is greatest in the “glacier-affected” parts of several features where debris-covered glacial ice from previous glacier advance and retreat cycles is downwasting. In the periglacial parts of rock glaciers, no significant signal of surface elevation change could be measured, and individual features show areas of both surface elevation gains and losses. Horizontal surface displacements of rock glaciers, determined through image matching, show rates as high as 3 m per year (2012-2016). Based on the relatively high concentration of large rock glaciers in this region, and the rapid retreat of glaciers, the freshwater contributions of rock glaciers may become increasingly important in the future.

ACKNOWLEDGEMENTS

I would like to offer heartfelt thanks to Dr. habil. Tobias Bolch at the University of Zurich, for supervising my project and providing guidance and support throughout. I appreciate that you made time for my questions and queries despite your busy schedule and your many other projects and responsibilities. I learned a great deal and am grateful to have had the chance to work with you. Thanks also to Dr. Holger Kumke at the Technical University of Munich for being my local supervisor.

I am grateful for the assistance I received from Franz Georlich and Fabienne Maag at the University of Zurich. And to my dear colleagues in the 4th intake of the Cartography M.Sc. Programme, I wish you success in your future endeavors, cartographic and otherwise. Juliane Cron, thank you for all the work you do to make the program better, and for sanity-saving coffee breaks.

To my folks, Sarah and Richard Strel, thank you for not mentioning “the T-word” too often, and for your eager proofreading and general enthusiasm for my studies. And finally, thank you Eric Schnepf, for putting up with me.

TABLE OF CONTENTS

STATEMENT OF AUTHORSHIP	I
ABSTRACT	II
ACKNOWLEDGEMENTS	III
TABLE OF CONTENTS	IV
LIST OF FIGURES	V
LIST OF TABLES	VIII
LIST OF ABBREVIATIONS	IX
1 INTRODUCTION	1
1.1 Project overview	1
1.2 Motivation	1
1.3 Objectives	2
1.4 Thesis structure	2
2 BACKGROUND INFORMATION	3
2.1 A brief introduction to glaciers.....	3
2.2 Rock glaciers: definition, description and distribution.....	3
2.3 Climate change and rock glaciers	6
2.4 Satellite remote sensing for observing glaciers and rock glaciers.....	7
3 STUDY AREA	14
3.1 Tien Shan	14
3.2 Northern Tien Shan	15
3.3 Specific Study Area.....	19
3.4 A note on place names	24
4 DATA	25
4.1 High resolution optical satellite stereo imagery.....	25
4.2 Additional datasets	30
5 METHODOLOGY	31
5.1 Digital Elevation Model (DEM) generation	31
5.2 DEM co-registration	34
5.3 Surface elevation change.....	41
5.4 Orthoimage generation	43
5.5 Glacier change measurements.....	43
5.6 Rock glacier change measurements.....	45
6 RESULTS AND DISCUSSION	49
6.1 Glaciers	49
6.2 Rock glaciers	54
6.3 Additional identifiable features.....	63
6.4 Discussion of all results and findings.....	66
7 CONCLUSION.....	69
7.1 Key findings	69
7.2 Study limitations.....	69
7.3 Future research	70
8 BIBLIOGRAPHY	71
APPENDIX	77

LIST OF FIGURES

Figure 1: Annotated Google Earth image of East Grasshopper Rock Glacier, Montana (45°03'22"N, 109°33'08"W).....	4
Figure 2: Using Google Earth imagery for rock glacier identification. Rock glacier identifiers in yellow: latitudinal ridge (LR), transverse ridge (TR), front slope (FS). Figure from Kinworthy (2016).	9
Figure 3: Rapid advance of Plator Rock Glacier as delineated from sequential orthoimages. The front advanced 92.1 m between 1981 and 2012. Figure from Scotti et al. (2016).	9
Figure 4: Across-track (left) and along-track (right) stereo satellite imagery acquisition. Figure from Kääb (2005).	10
Figure 5: Worldview example of 4 m CE90. 90% of points are within 4 m of the true location. Figure from DigitalGlobe (2016).	11
Figure 6: Reichenkar rock glacier with surface elevation change (a and b) between a 1996 aerial stereoscopic DEM and a 2006 LiDAR DEM (shown in c). Figure from Abermann et al. (2010).	12
Figure 7: Displacement vectors at Muragle rock glacier, Swiss Alps (1981-1994). Figure from Kääb (2002).	13
Figure 8: Regional overview of Tien Shan.	14
Figure 9: Regional overview of Northern Tien Shan.	15
Figure 10: Geomorphological elevation zones. Figure translated from Bolch (2006).	16
Figure 11: Frontal advance rates of Gorodetsky and Morenny rock glaciers. Figure from Bolch (2006), with base data from Gorbunov et al. (1992) and Marchenko (2003b).	17
Figure 12: Overview of study area. Extent of GeoEye-1 (clipped to cloud-free areas) and Pléiades stereo imagery with pan-sharpened, true-colour Landsat 8 background (Landsat imagery Sept. 15, 2016).	19
Figure 13: Ulken Almaty Valley. Figure translated from Bolch (2006).	20
Figure 14: Kishi Almaty Valley. Figure translated from Bolch (2006).	21
Figure 15: Kishi Almaty glacier mass balance variations (1965-1990). Specific mass balance at the ELA (left) and cumulative mass balance (right).	22
Figure 16: Left Talgar Valley. Figure translated from Bolch (2006).	23
Figure 17: Gorodetsky rock glacier terminus as shown in high resolution imagery (CORONA, GeoEye-1, Pléiades). Medium resolution (15m pixel size) Landsat 8 OLI, panchromatic band 8 (Sept. 15, 2016) is shown for comparison.	25
Figure 18: Pléiades satellite and sensor overview.	26
Figure 19: GeoEye-1 Satellite and Sensor Overview.	27
Figure 20: CORONA camera arrangement and shape of ground footprint showing geometric distortions. Figure from Galiatsatos et al. (2007).	28
Figure 21: CORONA KH-4B satellite and sensor overview (USGS, 2008).	29
Figure 22: Extent of CORONA Imagery frames with Landsat 8 background (Landsat imagery Sept. 15, 2016).	29

Figure 23: Control points (triangles) and check points (circles) identified using the Classic Point Measurement tool in ERDAS IMAGINE Photogrammetry. Pléiades imagery (left) and GeoEye-1 tile outlines (right).	31
Figure 24: Unstable terrain polygon with Landsat background.	35
Figure 25: Co-registration method of Nuth and Kääb (2011).	36
Figure 26: ArcGIS ModelBuilder tool created to iterate co-registration of multiple DEMs.	37
Figure 27: Histograms of the original SRTM-Pléiades elevation differences and the post-co-registration SRTM-Pléiades elevation differences.	38
Figure 28: Co-registration results for an example slave DEM (Cor 3). In the upper left (A), the elevation difference between the original Cor 3 DEM and the co-registered Cor 3 DEM. In the upper right (B) the histograms of elevation differences between the Cor 3 DEM and the Pléiades master DEM before and after co-registration. On the lower row, the elevation difference rasters of Pléiades and Cor 3 before (C) and after (D) co-registration.	40
Figure 29: Glacier delineation CORONA 1971 (left), GeoEye-1 2012 (centre), and Pléiades 2016 (right).	44
Figure 30: Example of rock glacier delineation. Upper images show a slope raster (left) and hillshade (right), which were useful for feature identification/confirmation. In the lower row, the same rock glacier is identifiable in the Pléiades imagery (left) and can be easily viewed from a different angle in Google Earth imagery (right).	46
Figure 31: COSI-Corr displacement results at Gorodetsky rock glacier using different initial/final window size settings in the frequency correlator tool. Window sizes (initial, final) are: A 128, 64; B 64, 32; and C 32, 16.	47
Figure 32: Horizontal Surface Displacement from 1971 – 2016 with glacier areas removed. Results of highlighted rock glaciers are discussed in Chapter 6.	48
Figure 33: Glacier delineations from 1971 (CORONA), 2012 (GeoEye-1), and Pléiades (2016). Background image is pan-sharpened Pléiades true-colour composite.	49
Figure 34: . Relationship between glacier area and relative glacier-area change (%) from 1971 – 2016.	50
Figure 35: Difference between 1971 CORONA DEM and 2012 GeoEye-1 DEM, with glacier areas highlighted.	51
Figure 36: Difference between 2012 GeoEye-1 DEM and 2016 Pléiades DEM, with glacier areas highlighted.	52
Figure 37: Surface elevation change at Tuyuksu Glacier. Note the different colour scales for the long term change (1971-2012 and 1971-2016; left and center) and the recent change (2012-2016; right).	53
Figure 38: Rock glaciers identified in the high resolution imagery. Landsat 8 panchromatic background image.	54
Figure 39: Rock glacier inventory examples. Red line indicates 200 m in each square.	55
Figure 40: Surface elevation change of rock glaciers (1971-2016).	56
Figure 41: Ordzhonikidze Rock Glacier surface elevation change (1971-2016). Surface elevation gains and losses are heterogeneous. Front advance can be seen in high positive values at the toe.	58

Figure 42: Morenny Rock Glacier. Left: surface elevation change (1971-2012). Middle: Surface elevation change (2012-2016).....	59
Figure 43: Overview of COSI-Corr image tracking results showing horizontal surface displacement between 2012 and 2016. Highlighted areas A, B, and C are shown in more detail in Figures 41, 42, and 43, respectively.	59
Figure 44: Horizontal surface displacement (2012 - 2016) at Morenny Rock glacier (inset A from Figure 40). Uncertainty of displacement measurements is \pm 0.69 m E/W and \pm 0.98 m N/S.	60
Figure 45: Horizontal surface displacement (2012 – 2016) at Gorodetsky rock glacier (black outline) and the glacier forefield area above (inset B from Figure 40). Uncertainty of displacement: \pm 0.69 m E/W and \pm 0.98 m N/S.	61
Figure 46: Ordzhonikidze rock glacier average surface speeds. Results of Sorg et al. (2015) in blue. Results from this study in red. Note the different axes for the three regions (lower, middle, and upper). Region divisions were created based on figure S13 from Sorg et al. (2015). Figure modified from Sorg et al. (2015, supplementary materials).....	61
Figure 47: An area of high activity (inset C from figure 40), including Ordzhonikidze rock glacier. Uncertainty of displacement measurements is \pm 0.69 m E/W and \pm 0.98 m N/S.	62
Figure 48: Horizontal surface displacements for 4 regions (1971-2016). Uncertainty of displacement measurements is \pm 5.05 m E/W and \pm 3.15 m N/S.....	62
Figure 49: Comparison of COSI-Corr displacement results for three rock glacier areas for the 2012-2016 time period (top) and 1971-2016 period (bottom).	63
Figure 50: Erosion along a stream in the northwest part of the study area.	64
Figure 51: Lake formation following glacier retreat. Left: two pro-glacial areas as seen in the 1971 CORONA imagery. Right: the same areas in 2012 with multiple lakes. These lakes are potential sources of flood or mudslide hazards.	65
Figure 52: A rock glacier with a large debris flow scar. The lower part of the rock glacier was washed away.	65
Figure 53: CORONA 1971 image of Dmitrieva Glacier, showing position of medial moraines (left). Surface elevation change (1971-2016) showing lowering of ice-cored moraines.	66
Figure 54: Surface elevation change near the Tuyuksu Glacier terminus.	66
Figure 55: Gorodetsky Rock glacier. Top: Orthoimage with numbers corresponding to notes in the text. Middle: Horizontal Surface Displacement (2012-2016). Bottom: Surface elevation change (1971- 2016).	68

LIST OF TABLES

Table 1: Glacier and rock glacier characteristics using ASTER- and SRTM-derived DEM in the Kishi Almaty (Malaya Almatinka), Uken Almaty (Bolshaya Almatinka) and Left Talgar (Lev Talgar) valleys in Northern Tien Shan. Table from Bolch et al. (2005).	24
Table 2: Names used in this study and former/additional names and alternative spellings.....	24
Table 3: CORONA mission information (USGS, 2008).....	27
Table 4: ERDAS IMAGINE Photogrammetry triangulation results for Pléiades (PL) and GeoEye-1 (GE) image blocks.....	32
Table 5: ERDAS IMAGINE Photogrammetry Automatic Terrain Extraction report for Pléiades (PL) and GeoEye-1 (GE) DEMs. (NIMA Absolute LE90 = U.S. National Imagery and Mapping Agency Absolute Linear Error 90.)	32
Table 6: CORONA DEM Image stereo pairs. One forward image (DS115-1104DF118) was used twice, with two separate aft images.....	33
Table 7: Default scene parameters. ω is viewing angle across flight direction, ϕ is forward and backward camera tilt, κ is flight direction (0° = east).....	33
Table 8: GCP residuals following stereo parameter adjustment.	34
Table 9: Co-registration of Pléiades DEM to SRTM DEM using ArcGIS/Excel-based method. The elevation difference (dh) RMSE, mean, and standard deviation were calculated from stable terrain pixels with slope between 10° and 45° and a dh value between -50m and 50m (as a rough method for removing outliers).	37
Table 10: Cumulative raster x-, y-, and z-shifts performed during co-registration based on Nuth and Kääb (2011) to align all CORONA and GeoEye-1 slave DEMs to the reference Pléiades DEM.	39
Table 11: Elevation difference (dh) between Pléiades (master) DEM and CORONA/GeoEye-1 (slave) DEMs before and after co-registration steps. Values are from stable terrain areas, with outliers removed and no-autocorrelation.	39
Table 12: Statistics of elevation differences over stable terrain.....	41
Table 13: Statistics of stable terrain dh values.....	42
Table 14: Glacier and rock glacier surface elevation change.	43
Table 15: East/west and north/south displacement statistics in stable terrain.....	48
Table 16: Glacier area change 1971 – 2016.	50
Table 17: Glacier volume and mass changes.	52
Table 18: Tuyuksu Glacier (Tsentralniy Tuyuksuyskiy) geodetic annual mass balance with comparison to WGMS glaciological record.....	54
Table 19: Surface elevation change of rock glaciers.....	57

LIST OF ABBREVIATIONS

3D	Three dimensional
a.s.l.	above sea level
ASTER	Advanced Spaceborne Thermal Emission and Reflection Radiometer
CE90	Circular Error 90%
COSI-Corr	Co-Registration of Optically Sensed Images and Correlation
CP	Check Point
DEM	Digital Elevation Model
dh	elevation difference
DHM	Digital Height Model
DinSAR	Differential Interferometry Synthetic Aperture Radar
DoD	DEM of Difference
DSM	Digital Surface Model
DTM	Digital Terrain Model
ELA	Equilibrium Line Altitude
ETM+	Enhanced Thematic Mapper Plus
FFT	Fast Fourier Transform
GCP	Ground Control Points
GIS	Geographic Information System
GLOF	Glacier Lake Outburst Flood
GPR	Ground penetrating radar
GPS	Global Positioning System
GRACE	Gravity Recovery and Climate Experiment
GSD	Ground Sampling Distance
InSAR	Interferometric Synthetic Aperture Radar
IPCC	Intergovernmental Panel on Climate Change
IQR	Inter-quartile range
LE90	Linear Error 90%
LIA	Little Ice Age
LIDAR	Light Detection and Ranging
MAAT	Mean Annual Air Temperature
MAGT	Mean Annual Ground Temperature
MAP	Mean Annual Precipitation
MED	Mean Elevation Difference
NMAD	Normalized Median Absolute Deviation
OLI	Operational Land Imager
PDGL	Potentially Dangerous Glacial Lake
RFM	Rational Function Model
RGI	Randolph Glacier Inventory
RMS	Root Mean Square
RMSE	Root Mean Square Error
RPC	Rational Polynomial Coefficients
RSG	Remote Sensing Software Package Graz
SAR	Synthetic Aperture Radar
SE	Standard Error
SNR	Signal-to-Noise Ratio
SRTM	Shuttle Radar Topography Mission
STDV	Standard deviation
TP	Tie Point
USGS	United States Geological Survey
UTM	Universal Transverse Mercator
w.e.	water equivalent
WGMS	World Glacier Monitoring Service

1 INTRODUCTION

1.1 Project overview

Rock glaciers and glaciers are important components of the cryosphere and the hydrologic cycle in high mountain environments. Rock glaciers are cryogenic landforms, comprising a mixture of ice and rock, which creep downslope due to gravity (Haeberli et al., 2006). They can be found in many dry-cold, mountainous regions, including the periglacial zone of Northern Tien Shan in Central Asia. Glaciers, rock glaciers and permafrost have been studied in this region for decades, both through field-based research and remote sensing. This project focuses on using high-resolution optical satellite imagery to observe changes in rock glaciers and glaciers in a select region of Northern Tien Shan, near the border of Kazakhstan and Kyrgyzstan. Stereo imagery acquired in 2016 (Pléiades), 2012 (GeoEye-1) and 1971 (CORONA), provide the opportunity to observe both recent and multi-decadal changes of these landforms in this region.

1.2 Motivation

Glaciers and rock glaciers are of scientific and practical interest for a variety of reasons. In geomorphology, they play an important role in debris transport and landscape evolution (Humlum, 2000). From a geotechnical perspective, permafrost change can affect slope stability, potentially increasing the risk of debris flows, rock falls, and flood hazards (e.g. Noetzli et al., 2003). Likewise, glaciers are associated with a number of natural hazards including glacier lake outburst floods and seasonal flooding. Rock glaciers, as permafrost features, are naturally influenced by changes in climate, but their response is more conservative than that of glaciers, and the interaction between climate and rock glaciers is relatively poorly understood (Sorg et al., 2015). This link is an important one: how rock glaciers react in a changing climate will have impacts on water resource availability as well as periglacial hazards in the future (Bolch & Marchenko, 2006; Sorg et al., 2015). Furthermore, relict rock glaciers can be used to reconstruct regional paleoclimate by providing evidence of former temperature and permafrost conditions (e.g. Hughes et al., 2003).

Perhaps most critical is the role that glaciers and rock glaciers play in regional hydrology and water availability. Glacier runoff provides water for drinking, irrigation, and hydroelectric power generation, acting as a water tower for downstream communities in Northern Tien Shan (Bolch & Marchenko, 2006). Runoff from rock glaciers and other periglacial features also contributes to local freshwater resources, and the high concentration of rock glaciers in this region suggests that this contribution is not negligible. In the context of a changing climate, retreating glaciers will alter hydrology patterns (Azócar & Brenning, 2010), initially providing additional stream flow but eventually contributing less to summer runoff, when water resources are most stressed (Sorg et al., 2012). If this occurs, the relevance of rock glaciers and permafrost, which react more slowly to changes in the climate, may become increasingly significant (Bolch & Marchenko, 2006; Rangecroft et al., 2015).

While rock glaciers and glaciers have been studied in this region, previous satellite-based studies relied primarily on medium resolution imagery and elevation data. High-resolution stereo imagery may provide a tool for more detailed mapping, and more accurate measurement of cryospheric change.

1.3 Objectives

The primary focus of this project is the observation and visualization of rock glacier and glacier change in a selected region of Northern Tien Shan through the use of high resolution stereoscopic optical satellite imagery. Specifically, the aims with respect to glaciers are to:

- i. Calculate glacier area change over time.
- ii. Calculate geodetic mass balance.

And with respect to rock glaciers, the aims are to:

- i. Identify and map rock glaciers within the study area.
- ii. Detect and measure surface elevation change over time.
- iii. Detect and measure horizontal surface displacements.

The information gained from these measurements will provide insight into how the cryosphere is changing in this region and implications this may have for future water resources and hazard risks. Finally, as this thesis is undertaken in the context of a cartography master's program, an overarching objective is the cartographic visualization of processes and results.

1.4 Thesis structure

Chapters 2 and 3 together provide background information and an overview of existing research and methods that form the basis of this thesis. This includes a brief introduction to glaciers (2.1), a discussion of rock glaciers (2.2) and how they are related to climate change (2.3), as well as relevant remote sensing approaches (2.4). Chapter 3 describes the study area (3.1-3.3) and an overview of rock glaciers (3.2.1) and glaciers (3.2.2) in Northern Tien Shan, based on existing literature. Section 3.4 gives a clarification of place names which may have recently changed, or may have multiple spellings/translations in the literature.

Chapter 4 outlines the data used for this project, including specifications of the satellite sensors and imagery (4.1) and information about other datasets used in this work (4.2). Chapter 5 details the methods used to achieve the objectives outlined above. The results and discussion (Chapter 6) is separated into glacier-specific results (6.1), rock glacier results (6.2), and additional features noted in the study area (6.3), with a summarizing discussion in 6.4. Chapter 7 is the conclusion, including key findings (7.1), study limitations (7.2) and future research (7.3). The list of references is provided in Chapter 8. The appendix contains full-figures which were shown in part earlier in the thesis.

2 BACKGROUND INFORMATION

2.1 A brief introduction to glaciers

Glacial ice, including ice sheets, ice caps, and glaciers, cover approximately 10 % of the earth's surface and contain about 75 % of all fresh water on earth. Glaciers are persistent masses of land ice which flow downslope under the influence of gravity (IPCC, 2014). Sensitive to changes in the climate, nearly all glaciers have been shrinking in area and mass in recent years (IPCC, 2014). The retreat of mountain glaciers provides one of the most visible indications of the effects of climate change. The volume of ice loss from mountain glaciers is disproportionately large compared to the Antarctic and Greenlandic ice sheets and is a major contributor to sea level rise (Gardner et al., 2013). The IPCC (2014 p. 342) reports with high confidence that “current glacier extents are out of balance with current climatic conditions, indicating that glaciers will continue to shrink in the future even without further temperature increase”.

Studies of glacier mass balance (the sum of snow/ice accumulation and ablation) rely on a number of different methods. The glaciological method is based on in situ measurements of accumulation and ablation. Long-term glaciological mass balance records are limited to a relatively small number of glaciers worldwide, but provide an important dataset of field-based measurements. Data available through the World Glacier Monitoring Service (WGMS) date back more than six decades (Zemp et al., 2009). In contrast to the glaciological method, remote sensing allows for a much larger area of study and calculations of mass balance at a regional scale. Remote sensing methods include observations of elevation changes, ice flux, glacier area change, snowline elevation, and accumulation-ablation area ratio estimation (Bamber & Rivera, 2007). The geodetic method, based on multi-temporal observations of glacier surface elevation, is used in this study. Geodetic mass balance is estimated from observations of elevation change over time (dh/dt), which requires surface elevation measurements from at least two time periods separated by a sufficient interval for the magnitude of the change to be significant relative to the uncertainty of the measurements.

2.2 Rock glaciers: definition, description and distribution

The scientific definition of a rock glacier has evolved over time and has been a matter of recurring debate (Berthling, 2011). Some definitions in the literature have focused on the genesis of rock glaciers (e.g. Haeberli, 1985) and others on the morphology (e.g. Potter, 1972), or some combination of the two (e.g. Barsch, 1992). A lengthy discussion of this debate is provided by Berthling (2011), with a proposed definition of rock glaciers as cryo-conditioned landforms. By this definition, “active rock glaciers are the visible expression of cumulative deformation by long-term creep of ice/debris mixtures under permafrost conditions” (p. 105). Alternatively, the definition by Barsch (1992, p. 176) defines rock glaciers by form,

material and process, calling them “lobate or tongue-shaped bodies of perennally frozen unconsolidated material supersaturated with interstitial ice and ice lenses that move down slope by creep as a consequence of the deformation of ice contained in them and which are, thus, features of cohesive flow”. Although the definitions vary, rock glaciers are phenomena of *permafrost* and *creep*. Permafrost, or perennally cryotic ground, is defined on the basis of temperature as ground that remains at or below 0°C for at least two years (Harris et al., 1988). Permafrost creep is the slow, long-term deformation of cohesive, ice-rich sediments (Harris et al., 1988), which allows rock glaciers to move downslope under the influence of gravity.

Large rock glaciers are impressive landform features, often with a morphology resembling the viscous flow of lava (Figure 1). The appearance and characteristics may vary greatly between features, but a general morphological classification divides rock glaciers as tongue-shaped, lobate, or spatulate, based on the length to width ratio (Wahrhaftig & Cox, 1959). Rock glaciers with multiple parts, lobes, sources or ages may also be classified as complex (Barsch, 1996). Additional categorizations focus on dynamic status, labeling rock glaciers as *active* (actively creeping downslope), *inactive* (not moving but still containing frozen material) or *fossil/relict* (formerly active, no longer containing ice) (Barsch, 1992). Active and inactive rock glaciers are also referred to as *intact*. Alternatively these landforms may be divided by their debris source as either talus rock glaciers (found below talus slopes) or debris/moraine rock glaciers (found below glacial till deposits) (Barsch, 1996).

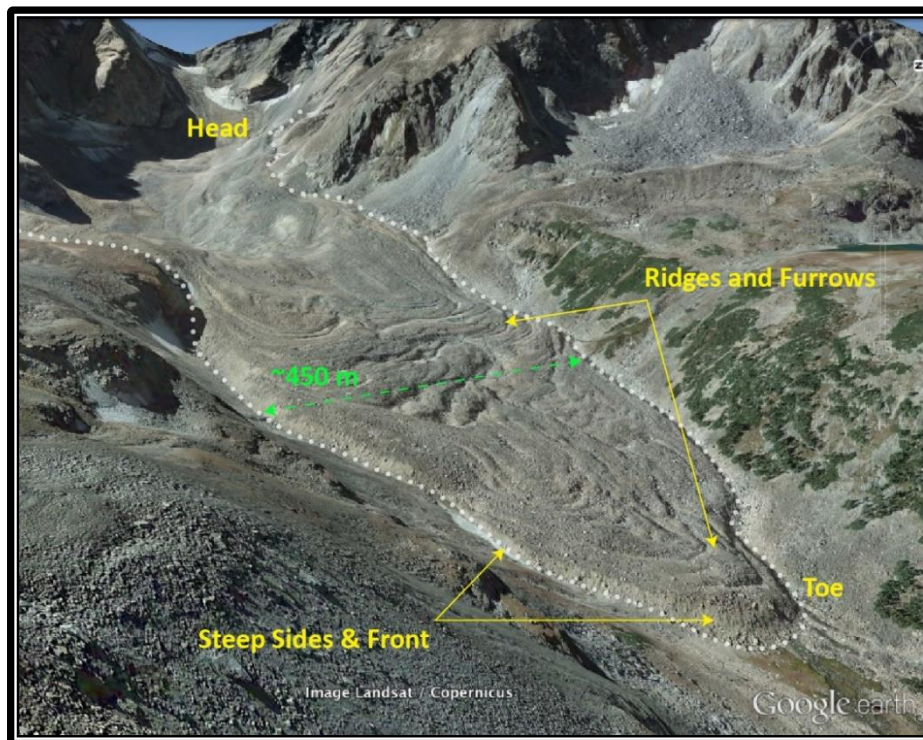


Figure 1: Annotated Google Earth image of East Grasshopper Rock Glacier, Montana (45°03'22"N, 109°33'08"W).

Ranging in size from tens of metres to several kilometres in length (Humlum, 2000), rock glaciers may appear as small protalus lobes or extremely large, complex features, flowing from a high-elevation *head* to a low-elevation *terminus* or *toe* (Kinworthy, 2016). They typically move at rates of several centimetres to several metres per year and are thousands to tens of thousands of years old (Kääb et al., 2007). A blocky debris mantle covers the surface and, when active, rock glaciers exhibit steep slopes along the sides and front which may appear lighter in colour due to the recent exposure of this material (Barsch, 1996). These slopes are usually at, or steeper than, the angle of repose and may stand up to 100 m above the surrounding terrain (Barsch, 1996). Below the 2-5 m thick boulder mantle, one can find finer-grained materials which may also be visible along the exposed side and front slopes (Barsch, 1992; 1996). The surficial morphology comprises small-scale, irregular features produced by ice formation and melt near the surface, as well as larger deformation features – regular furrows and ridges – caused by extending and compressing flow (Haeberli, 1985).

The genesis and composition of rock glaciers has also been a topic of scientific debate, particularly regarding the origin of the internal ice as either glacial or periglacial (Hamilton & Whalley, 1995). That is, can rock glaciers be formed from glaciers, either as the main source of ice or by a transition from a debris-covered glacier? Or do rock glaciers arise from periglacial processes and ice sources only (e.g. frozen material from talus slopes or moraines with embedded non-glacial ice)? Following decades of discussion, this debate has been deflated, with an acceptance that both options are possible (Kinworthy, 2016), and that in any case, the “semantic dispute... never provided any insight which would be considered remarkable or useful” (Haeberli, 2000, p. 290). Regardless of origin, ice content ranges from 20 to 80% by volume (Marchenko et al., 2007) and exists as interstitial ice, ice lenses or massive ice (Barsch, 1996).

Rock glaciers are found in cold, dry environments in high mountain systems around the world (Barsch, 1992). Haeberli (1985) estimates there may be several million rock glaciers worldwide, although no global inventory exists. Numerous regional inventories can give an idea of the frequency of these features in other regions (e.g. parts of the Alps: Kellerer-Pirklbauer et al., 2012; Krainer & Ribis, 2012; Seppi et al., 2012; Sierra Nevada (CA): Millar & Westfall, 2008; Bolivian Andes - Rangecroft et al., 2014) and in Northern Tien Shan (Gorbunov, 1998). The formation of rock glaciers requires the presence of an adequate debris source, permafrost conditions, and slope to induce flow (Haeberli, 1985). Boundary conditions are therefore related to climate, including mean annual air temperature (MAAT) and mean annual precipitation (MAP), as well as large-scale and local topography, local debris sources, and ground thermal conditions (Haeberli, 1985). In general, rock glaciers exist within the alpine permafrost/periglacial belt: the region below the local snow line or equilibrium line altitude (ELA) and above the lower permafrost limit (Haeberli, 1985). Continental climates are therefore favourable, as low precipitation rates limit glaciers to higher

elevations while cold temperatures allow for a larger extent of the mountain permafrost zone (Imbery, 2014). However, the coarse mantle cover of a rock glacier alters the surface thermal regime, creating a colder environment than the surrounding MAAT and allowing rock glaciers to potentially exist below the regional permafrost limit (Gorbunov et al., 2004).

2.3 Climate change and rock glaciers

Multi-decadal, human influenced climate warming has been observed worldwide and is expected to continue through the 21st century (IPCC, 2014). The cryosphere is naturally sensitive to changes in climate and the impacts can be seen in glaciers, ice sheets, snow cover, sea ice, and permafrost (IPCC, 2014). Dramatic retreat rates of glaciers provide a particularly visible indicator of a changing climate. By contrast, the interaction between climate and rock glaciers is less visible and relatively poorly understood (Sorg et al., 2015). Signs of rock glacier destabilization, including observed velocity changes, subsidence, and landform degradation have been attributed to climate change (IPCC, 2014).

Several studies have examined the relationship between rock glacier speeds and air or ground temperatures over seasonal to millennial time scales (e.g. Delaloye et al., 2008; Frauenfelder & Kääb, 2000; Kääb et al., 2007; Wirz et al., 2016). Over relatively short time spans, rock glacier velocities in Switzerland were found to vary seasonally, by gradually slowing with the onset of winter and speeding up relatively rapidly following temperature rise or water input (Wirz et al., 2016). Dendrochronology and remote sensing data show decadal-scale synchronicity of several Tien Shan rock glaciers, coinciding with summer temperature variations (Sorg et al., 2015). Kääb et al. (2007) found that rock glaciers with ground temperatures closer to 0°C generally flow faster than colder ones, and that many Swiss rock glaciers have accelerated in recent decades. Similar observations of speed increases at other rock glaciers (e.g. Bodin et al., 2015), suggest a climatic control (Kääb et al., 2007; Roer et al., 2005). Modelling by Müller et al. (2016) indicates that a 1°C increase in rock glacier temperature could increase velocities by 1.5 to 3 times, with greater impacts on rock glaciers which are already close to 0°C.

Along with acceleration, other signs of rock glacier destabilization have been observed, including surface lowering, collapse features, and the formation of cracks (e.g. Bodin et al., 2010; Roer et al., 2008). Rock glacier destabilization is not driven solely by temperature, but rather by a complex combination of factors, making the relation between climate change and rock glacier dynamics difficult to decipher (Müller et al., 2016; Sorg et al., 2015).

Understanding mountain permafrost in light of climate change is significant for geohazard risk management (e.g. Noetzli et al., 2003) and for water resource management (e.g. Bellisario et al., 2013). The potential of rock glaciers as water resources has been identified in dry regions such as the Chilean Andes

(Azócar & Brenning, 2010), the Bolivian Andes (Rangecroft et al., 2013; 2014; 2015) and Northern Tien Shan (Bolch & Marchenko, 2006). However, the contributions of rock glaciers and permafrost to regional water cycles are not well quantified, and this topic has been flagged by multiple authors as requiring additional research (e.g. Sorg et al., 2012; Unger-Shayesteh et al., 2013). Climate change poses a threat to water security through changes in temperature and precipitation patterns, as well as through the eventual decrease, or altogether loss, of glaciers as high mountain water reservoirs – a particularly important water resource, as peak runoff is in the hottest summer months when water stress is usually highest (Rangecroft et al., 2013). Therefore, a possible increase in runoff from rock glaciers and other permafrost features due to climate change may become increasingly significant in the future (Bolch & Marchenko, 2006).

2.4 Satellite remote sensing for observing glaciers and rock glaciers

Terrestrial, aerial, and spaceborne remote sensing systems are critical tools of cryosphere research, including glaciers and mountain permafrost (Dozier, 2009; Kääb, 2005; Rees, 2005; Tedesco, 2014). The size, distribution, and characteristics of glaciers and rock glaciers limit the number of field-based studies to a relatively small number of sites and necessitate the use of aerial- and satellite-based sensors to gain regional and global information. Remote sensing can be used to identify and map features (2.4.1), create digital elevations models (2.4.2), detect terrain elevation change (2.4.3), and measure horizontal surface displacements (2.4.4) (Westermann et al., 2015).

The effectiveness of optical remote sensing techniques for these tasks depends on the spatial and temporal resolution of the data. *Spatial resolution* can be defined as the smallest detectable object in an image, and is often approximated by the pixel size (Kääb, 2005). *Temporal resolution* refers to the frequency of acquisition, or the interval between acquisitions (Kääb, 2005). Medium spatial resolution imagery (5-100 m pixel dimension), such as ASTER or Landsat, have been employed to investigate glaciers and also rock glaciers (e.g. Bolch, 2004), but some smaller features are undetectable. To achieve higher-resolution for permafrost studies, many studies have relied on aerial imagery (e.g. Kääb et al., 1997), but spatial coverage of such datasets with appropriate temporal resolution for change-detection are limited. In 2002, Kääb stated that the relatively small size of rock glaciers and their slow deformation rates meant that they could “hardly be monitored by optical satellite imagery” and that “[a]erial photography is, therefore, a prior tool for deriving thickness changes or horizontal displacements on rock glaciers” (Kääb, 2002, p. 46). This is however changing, with the increasing availability of high-resolution (< 5 m pixel dimension) optical satellite imagery such as Worldview, GeoEye-1, Quickbird, Pléiades and SPOT-6/7. The declassification of spy imagery from the 1960s and 1970s has also extended the temporal range of high- and medium-resolution optical satellite data, allowing for change detection over several decades.

2.4.1 Remote sensing for identifying and mapping glaciers and rock glaciers

Glacier delineation based on optical satellite imagery is a common step in many glacier investigations, and accurate mapping of glaciers is necessary for calculating area change and mass balance. Delineation of glaciers is not always straight forward and may be complicated by seasonal snow cover, debris cover, clouds, or shadows (Paul et al., 2013). A number of different methods for automatic or semi-automatic glacier delineation exist, and the accuracy of glacier outlines derived from remote sensing data is discussed by Paul et al. (2013). For this thesis, glaciers were delineated manually using panchromatic and pan-sharpened optical satellite imagery (section 5.5.1).

Regionally identifying, inventorying and mapping rock glaciers has relied on aerial and/or satellite imagery since early research such as that by Wahrhaftig and Cox (1959) in Alaska. Many other regional rock glacier inventories have been undertaken in the Alps, Rockies, Andes and Tien Shan using remote sensing (e.g. Northern Tien Shan: Gorbunov et al., 1998; parts of the Alps: Kellerer-Pirklbauer et al., 2012; Krainer & Ribis, 2012; Seppi et al., 2012; Sierra Nevada (CA): Millar & Westfall, 2008; Bolivian Andes: Rangecroft et al., 2014). While imagery can be expensive to purchase, freely available medium-resolution imagery such as Landsat can be used for rock glacier identification (Brenning, 2009). Alternatively, Google Earth imagery, sourced from various sensors and dates, has also been employed as a dataset for rock glacier inventories (Figure 2; e.g. in New Mexico: Kinworthy, 2016; Bolivian Andes: Rangecroft et al., 2014; Hindu Kush - Himalayan: Schmid et al., 2014; Northern Tien Shan: Wang et al., 2017). Google Earth imagery is also recommended by Paul et al. (2013) as an additional tool for improving delineation of debris-covered glaciers based on other imagery. Schmid et al. (2014) developed a “Manual for Mapping Rock Glaciers in Google Earth”, providing specific guidelines for identifying and classifying rock glacier features and characteristics such as flow structures and front steepness. An alternative list of suggested characteristics for identification of rock glaciers in satellite imagery is given by Kinworthy (2016, pp. 30-31):

- i. Lobate structures.
- ii. Steep frontal slope at lowest point of talus accumulation.
- iii. Longitudinal and transverse ridges and furrows.
- iv. Positive relief.
- v. Vegetation located primarily above the frontal lobe.
- vi. Subsidence morphology.
- vii. Tonal change between frontal and side slopes and the greater body of talus.
- viii. Proximity to other rock glaciers.

Multi-temporal mapping can be used to monitor change in frontal position (Figure 3; Scotti et al., 2016), or with sufficiently high spatial resolution, it is also possible to map smaller features such as the development of cracks (Roer et al., 2008).

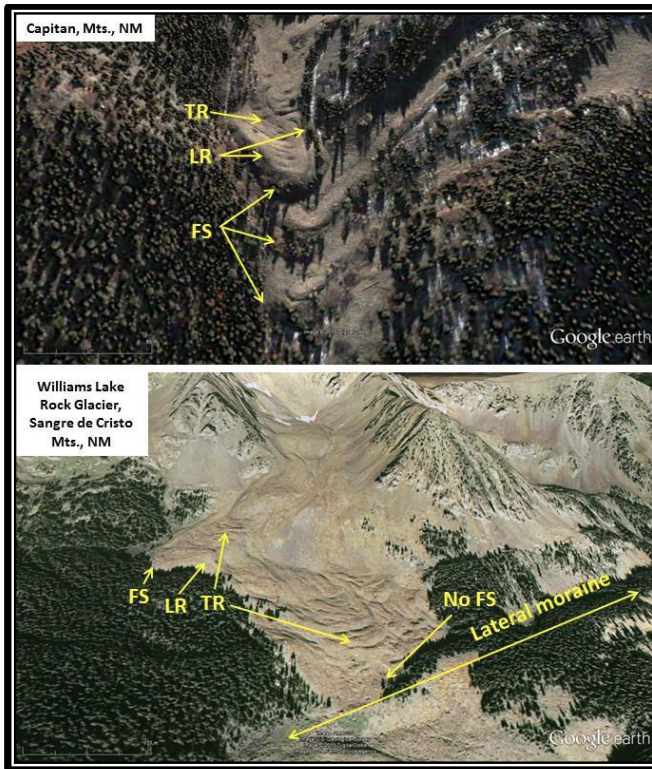


Figure 2: Using Google Earth imagery for rock glacier identification. Rock glacier identifiers in yellow: latitudinal ridge (LR), transverse ridge (TR), front slope (FS). Figure from Kinworthy (2016).

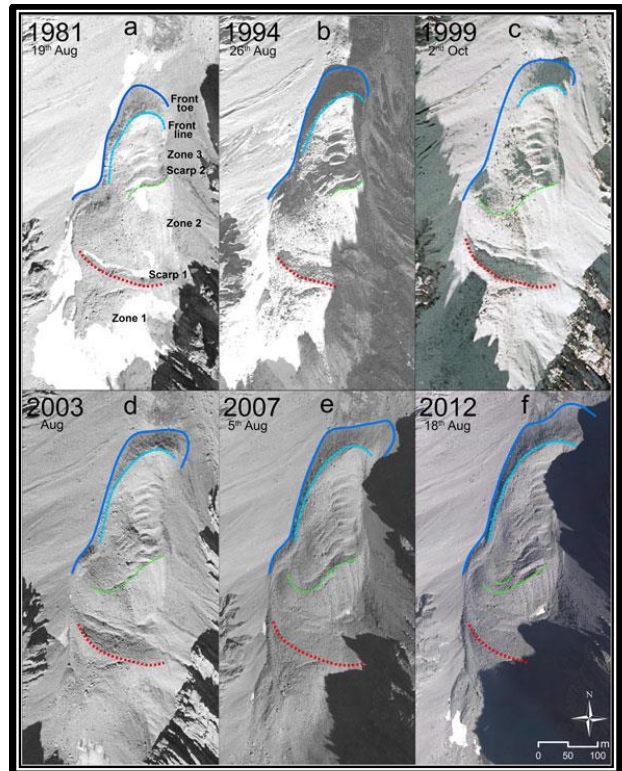


Figure 3: Rapid advance of Plator Rock Glacier as delineated from sequential orthoimages. The front advanced 92.1 m between 1981 and 2012. Figure from Scotti et al. (2016).

2.4.2 Optical remote sensing for generating digital elevation data

Digital elevation data can be derived from both active and passive sensors using spaceborne, aerial or terrestrial platforms (Kääb, 2005). A brief overview of DEM generation from optical satellite stereo imagery is given here – for a summary of other methods such as InSAR and LIDAR, see Westermann et al. (2015, section 13.2.2). A *digital elevation model* (DEM), sometimes also referred to as a *digital height model* (DHM), is often a key dataset for cryosphere research. Additional terms for elevation data include *digital surface model* (DSM), which generally includes features such as buildings and trees, and *digital terrain model* (DTM), in which these features have been removed and only the terrain surface remains. For simplicity, only the term DEM is used here.

Generating a DEM from optical satellite imagery requires a set of two or more overlapping images, recorded from different viewing angles, known as stereo(scopic) imagery. Stereo satellite imagery is obtained either by cross-track acquisition (images from adjacent orbits) or along-track acquisition (images from a single orbit pass) (**Figure 4**). Along-track stereo is generally preferable as the near-simultaneous acquisition ensures similar lighting, atmospheric, and ground conditions in both images (Kääb, 2005). Digital 3D information can be derived from the stereo parallax between images, using photogrammetry software

such as PCI Geomatica or ERDAS IMAGINE. This process relies on manual and/or automated selection of specific features identifiable in both images, known as tie points (TPs).

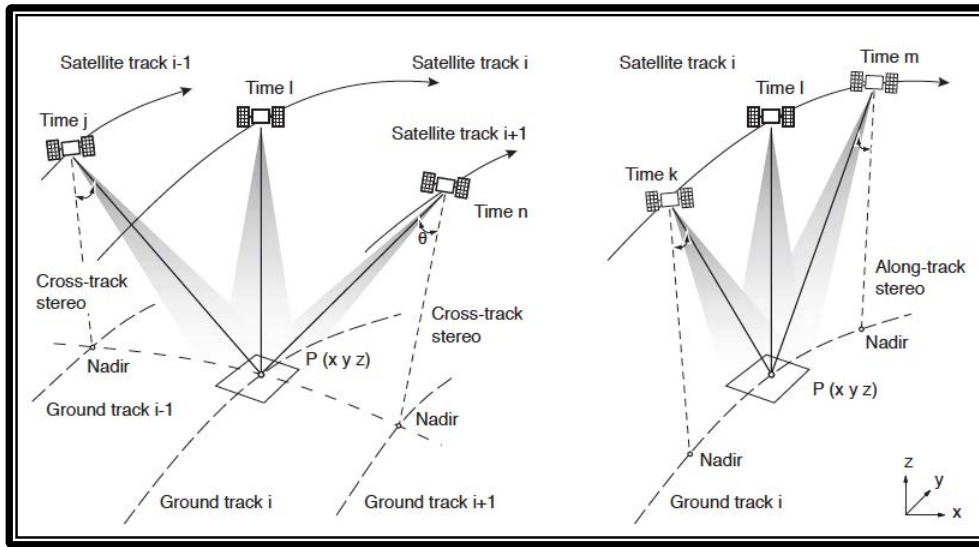


Figure 4: Across-track (left) and along-track (right) stereo satellite imagery acquisition. Figure from Käab (2005).

Additional information is required for the geometric correction and accurate geolocation of a DEM. Sensor-specific rational function models (RFMs) define the relationship between image coordinates and ground coordinates and they can be approximated through the use of rational polynomial coefficients (RPCs) (Astrium, 2012). Pre-computed RPCs are provided with most modern high-resolution imagery and can be directly incorporated in photogrammetry software. RPCs relate image pixel locations (x,y) to a corresponding latitude, longitude and elevation using a third-order rational polynomial (Astrium, 2012). Geolocation based solely on RPCs will however be of limited accuracy. To improve on this, an existing reference DEM can be employed to provide more accurate elevation data. Still, in most cases DEM generation relies on the identification of ground control points (GCPs) which are geographic features with known location coordinates which can be identified in the imagery. GCPs may be obtained in the field through global positioning system (GPS) measurements, or from topographic maps, orthorectified photos, air photo surveys, or other geospatial datasets (Toutin, 2004). Including even a small number of GCPs can greatly improve the vertical and horizontal accuracy of a DEM, and ideally GCPs should be well-distributed throughout the area of interest (Toutin, 2004).

The accuracy of a stereo DEM is influenced by a number of factors including the sensor parameters, image resolution, acquisition viewing angle and base-to-height ratio, ground topography, and the number/accuracy of GCPs (Toutin, 2004). Geolocation accuracy is a measure of the location of an object as it appears in an image compared to its true location on Earth (Astrium, 2012). This is often quantified using root-mean-square error (RMSE) which defines the level of dispersion of the frequency distribution of the differences between the DEM and a reference dataset (Weng, 2002). The larger the RMSE, the greater

the uncertainty/error of the DEM. This may be calculated through the use of Check Points (CPs) where the derived DEM point is compared to a known value (e.g. a reference DEM or a measured GCP).

The locational accuracy of satellite imagery may also be expressed using CE90 and LE90, which describe the 90% confidence interval for horizontal and vertical accuracy, respectively. CE90 gives the Circular Error in the horizontal plane at 90% confidence, meaning the actual location of an object is within this distance for 90% of the points (Figure 5). LE90 gives the Linear Error in the vertical plane at 90% confidence, meaning the actual elevation of an object is within this distance for at least 90% of the points. High resolution imagery such as GeoEye-1 have different specified CE90 and RMSE values for different products (e.g. 5m CE90 and 3 m RMSE for 0.5 m resolution imagery). However, these values do not include terrain and off-nadir effects which cause additional error and therefore lower accuracy in high mountain environments. The use of GCPs can improve the overall DEM accuracy.

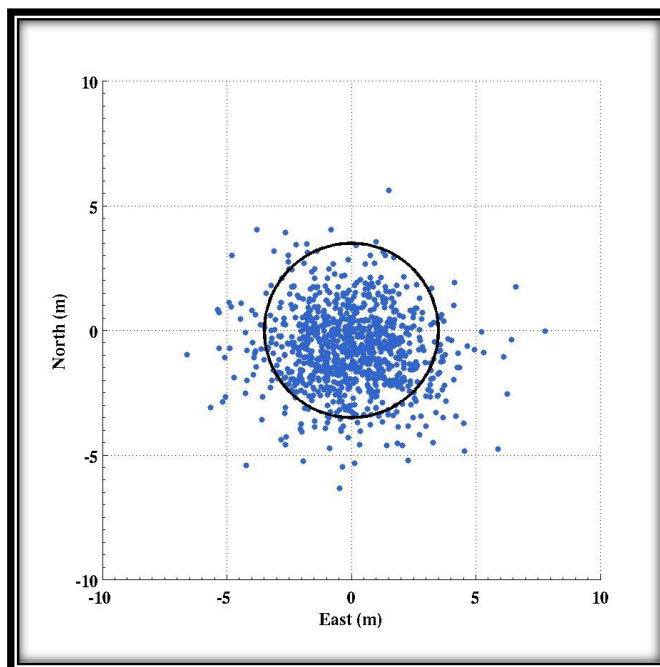


Figure 5: Worldview example of 4 m CE90. 90% of points are within 4 m of the true location. Figure from DigitalGlobe (2016).

2.4.3 Surface elevation change detection through DEM Differencing

Multi-temporal elevation datasets enable the detection of change in surface height over time ($\delta h/\delta t$). Subtracting repeat DEMs from one another gives a DEM of Difference (DoD), showing areas of local surface lift or lowering. Other remote sensing methods of measuring surface elevation change over time, such as Differential SAR Interferometry (DInSAR), are discussed by Kääb (2005, Chapter 4).

Before differencing DEMs, the rasters must first be accurately co-registered and corrections may be necessary to remove elevation-dependent or sensor-specific bias (Nuth & Kääb, 2011). Without accurate co-registration, a DoD may appear as a “false hillshade”, with terrain features still visible due to the elevation differences introduced by horizontal and/or vertical misalignment (Paul et al., 2015). Co-registration methods vary and may include translational shifts, rescaling, rotating, detrending, and/or additional bias correction. A comparison of several DEM co-registration methods used for glacier change analysis is given by Paul et al. (2015), finding that all methods found similar results but with different efficiencies. The recommended analytical method of Nuth & Kääb (2011), based on slope and aspect, is used in this thesis.

In glaciology, estimating mass balance by measuring surface elevation change is referred to as the geodetic method and has been employed for individual glaciers (e.g. Rees & Arnold, 2007) and regional areas and ranges (e.g. Arendt et al., 2002; Pieczonka & Bolch, 2015; Pieczonka et al., 2013). Elevation measurements must be sufficiently accurate and must be acquired with sufficient time separation so that the measured change is significant relative to measurement errors (Bamber & Rivera, 2007). Better vertical accuracy and higher horizontal resolution of the DEMs allows for change detection with greater temporal resolution (Abermann et al., 2010).

Rock glacier surface elevation changes are generally modest compared to glaciers and therefore most elevation change detection has relied on terrestrial or aerial remote sensing methods (Kääb, 2005). For example, multi-temporal DEMs derived from stereo aerial imagery were used by Kääb (2002) to show surface lowering of up to -0.5 m/year in the upper part of Muragl rock glacier between 1981 and 1994. Smaller heaving and settlements (± 0.1 m/a) were found in the lower part of the rock glacier. Similarly, Abermann et al. (2010) identified rock glacier frontal advance, surface lowering, and ridge propagation using multi-temporal DEMs derived from LiDAR and aerial photogrammetry (Figure 6). Surface elevation differencing cannot always give a clear signal of a rock glacier's total mass gain or loss, but information about thermokarst features, zones of ice melt, and rock glacier dynamics may be detected with suitable elevation data (Haeberli et al., 2006). This can also be used to identify the “glacier-affected” versus “periglacial” parts of a rock glacier (Kääb et al., 1997). Kääb et al. (1997) describes the glacier-affected part of the Gruben rock glacier in Switzerland as the area which was repeatedly overridden by glacier advances, leaving behind debris-covered dead ice deposits which affect the dynamics in the upper part of the rock glacier.

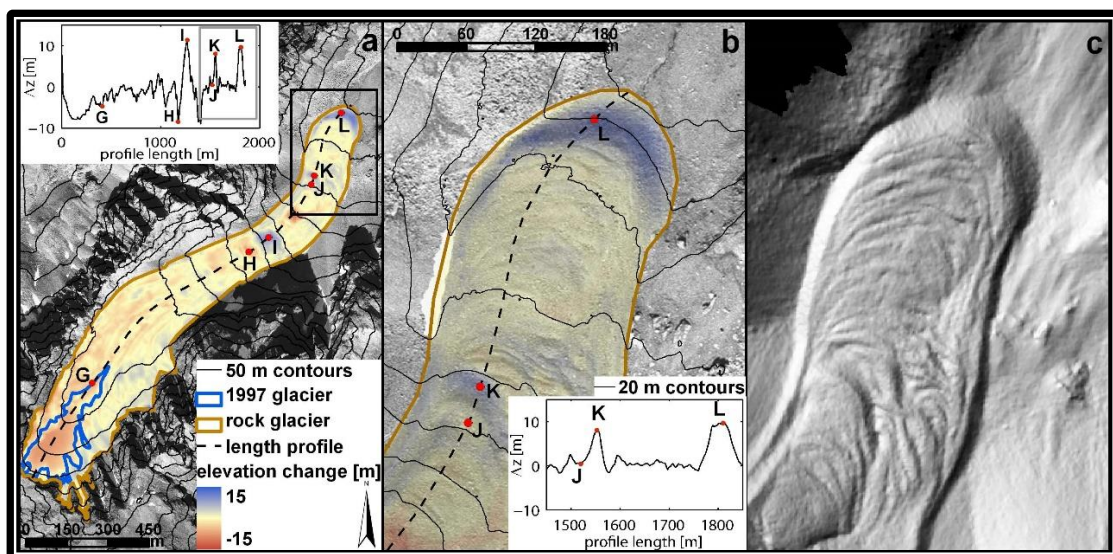


Figure 6: Reichenkar rock glacier with surface elevation change (a and b) between a 1996 aerial stereoscopic DEM and a 2006 LiDAR DEM (shown in c). Figure from Abermann et al. (2010).

2.4.4 Horizontal surface displacement

Horizontal surface displacements can be determined using multi-temporal, co-registered, optical satellite imagery with sufficient resolution for tracking surface features (Heid & Kääb, 2012). The time in between images must be long enough for detectable surface movement, but also short enough for objects to be repeatedly recognizable (Heid, 2011). As with other applications of satellite imagery, this method has many advantages over in situ measurements or terrestrial/aerial remote sensing, especially for monitoring large, remote areas. Other methods of determining surface displacements for rock glaciers, such as DInSAR or SAR image matching, are not discussed here (see e.g. Kääb, 2005).

Glacier surface velocities have been measured and monitored for decades using satellite imagery, originally by manually identifying specific features like crevasses and tracking their movement between consecutive images (e.g. Lucchitta & Ferguson, 1986). The digital automation of this process through image matching algorithms has made it faster and more accurate, with up to sub-pixel accuracy (Heid & Kääb, 2012). Applying these algorithms to determine rock glacier horizontal surface displacements can provide insight into the flow dynamics (Figure 7) and how surface velocities are changing over time.

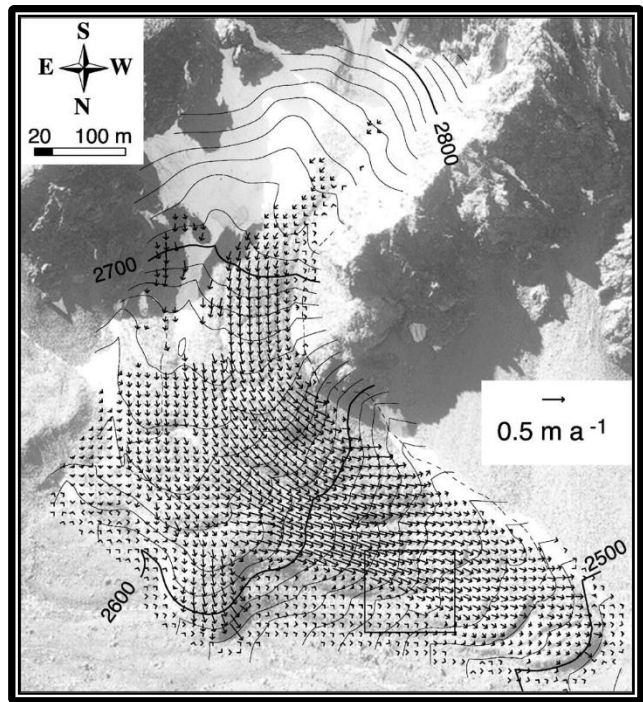


Figure 7: Displacement vectors at Muragle rock glacier, Swiss Alps (1981-1994). Figure from Kääb (2002).

Several image matching algorithms are commonly employed for glacier monitoring, the benefits and drawbacks of which are discussed by Heid (2011) as well as Heid and Kääb (2012). These can be divided into two main categories: those operating in the spatial domain, using intensity values in the image space, and those operating in the frequency domain (Heid, 2011). Frequency domain image matching relies on the convolution theorem, by which multiplying the Fast Fourier Transform (FFT) of one image and the complex conjugated FFT of a second image is the same as computing the cross-correlation in the spatial domain (McClellan et al., 2003). The Co-Registration of Optically Sensed Images and Correlation (COSI-Corr) method, which is integrated into ENVI software, is used in this study. COSI-Corr was developed by Leprince et al. (2007), and identified by Heid and Kääb (2012) as the most robust method of several common image matching algorithms used for measuring glacier flow velocities. COSI-Corr operates in the frequency domain, can provide sub-pixel accuracy, and is designed to be less sensitive to outliers than other similar methods (Heid & Kääb, 2012).

3 STUDY AREA

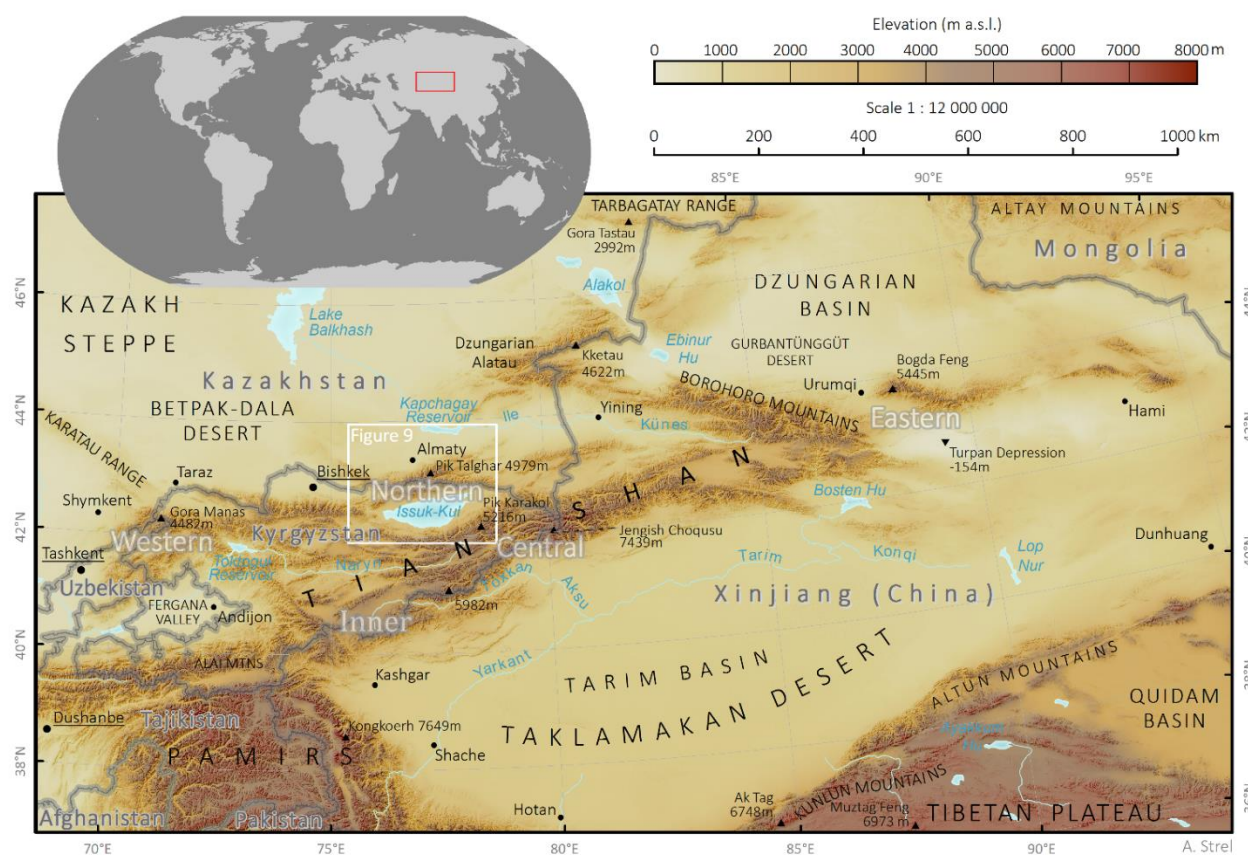


Figure 8: Regional overview of Tien Shan.

Map data sources: ©OpenStreetMap, Natural Earth, SRTM DEM.

3.1 Tien Shan

The Tien Shan Mountains extend from approximately 40 to 46° N and 67 to 95° E, stretching from Uzbekistan, through Kyrgyzstan and south-eastern Kazakhstan, to Xinjiang, China (Figure 8). Reaching 7439 m a.s.l., Jengish Choqus (Victory Peak), on the border of Kyrgyzstan and China, is the highest point of Tien Shan. The region is often divided into five parts: Western, Northern, Eastern, Central and Inner Tien Shan. In southern Tien Shan, the Alai Mountains transition into the Pamir Mountains of Tajikistan. Aside from this, Tien Shan is surrounded primarily by arid and semi-arid plains, basins, and deserts. The Taklamakan Desert lies in the Tarim Basin to the south. The Dzungarian Basin to the northeast of the Borohoro ranges contains the Gurbantünggüt Desert. North of Tien Shan is the vast Kazakh Steppe, and on the western edge is the Fergana Valley and the Kyzylkum Desert of Uzbekistan. The high elevation of Tien Shan creates a climatic barrier for western and northern air masses moving through Central Asia and therefore is a significant driver of regional climate (Takeuchi et al., 2014). The mountains act as a water tower for populations living in the foothills and plains surrounding Tien Shan (Chen et al., 2016).

3.2 Northern Tien Shan

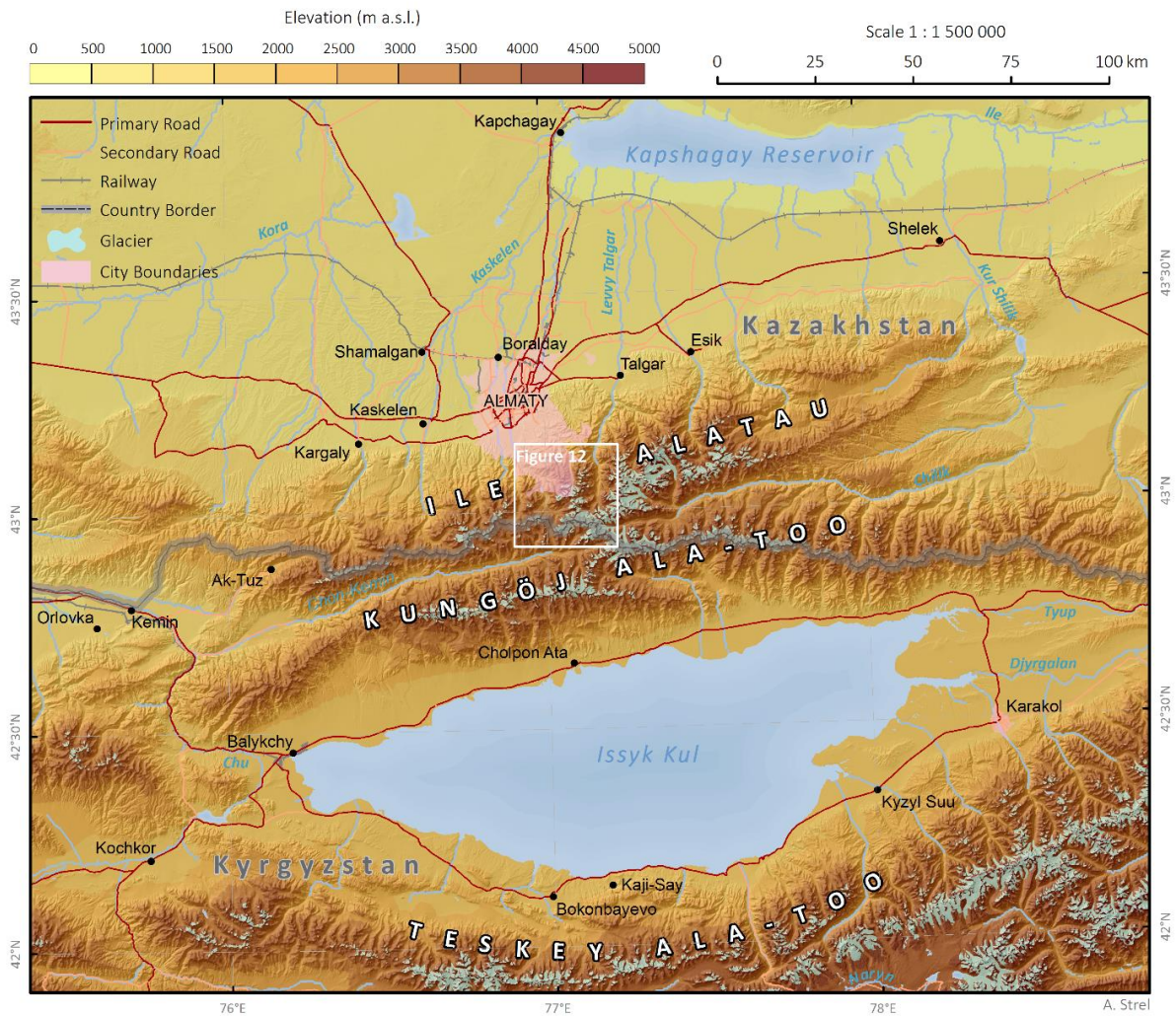


Figure 9: Regional overview of Northern Tien Shan.

Map data sources: ©OpenStreetMap, Natural Earth, RGI 5.0 (Arendt et al., 2015), HydroSHEDS (Lehner et al., 2008), SRTM DEM.

Northern Tien Shan (Figure 9) straddles the border between Kazakhstan and Kyrgyzstan with two predominant parallel ranges running east-west: Ile Alatau (Zailiyskiy Alatau) and Kungöj Ala-Too (Kungey Alatau). Ile Alatau reaches elevations of nearly 5000 m a.s.l. and is separated from the slightly lower Kungöj Ala-Too range by the large valley of the Chon-Kemin and Chilik Rivers (Figure 10). South of this is Issyk-Köl (Issyk-Kul), a large, endorheic Lake (1608 m a.s.l.), beyond which is the Teskey Ala-Too (Terskej Alatau) range. Both Ile Alatau and Kungöj Ala-Too originate from the Caledonian orogenesis and are still slightly uplifting (Chediya, 1986 cited in Bolch & Gorbunov, 2014). The lithology is mostly granite of Devonian, Silurian and Carboniferous age as well as Cambrian gneisses in the Kungöj Ala-Too (Chediya, 1986 cited in Bolch & Gorbunov, 2014).

The climate of Northern Tien Shan is highly variable, with greater precipitation (> 1000 mm/a at 3000m a.s.l.) on windward northern slopes compared to leeward southern valleys (< 800 mm/a) (Bolch &

Gorbunov, 2014). Precipitation is generally lowest in the winter due to the Siberian anticyclone and greatest in early summer (Bolch & Gorbunov, 2014). This climate gives way to a pronounced periglacial zone with frequent freeze-thaw cycles (Bolch & Gorbunov, 2014). Permafrost distribution can be expressed in relation to altitude as sporadic: 2700-3200 m a.s.l.; discontinuous: 3200-3500 m a.s.l.; and continuous: above 3500 m a.s.l. (Marchenko et al., 2007).

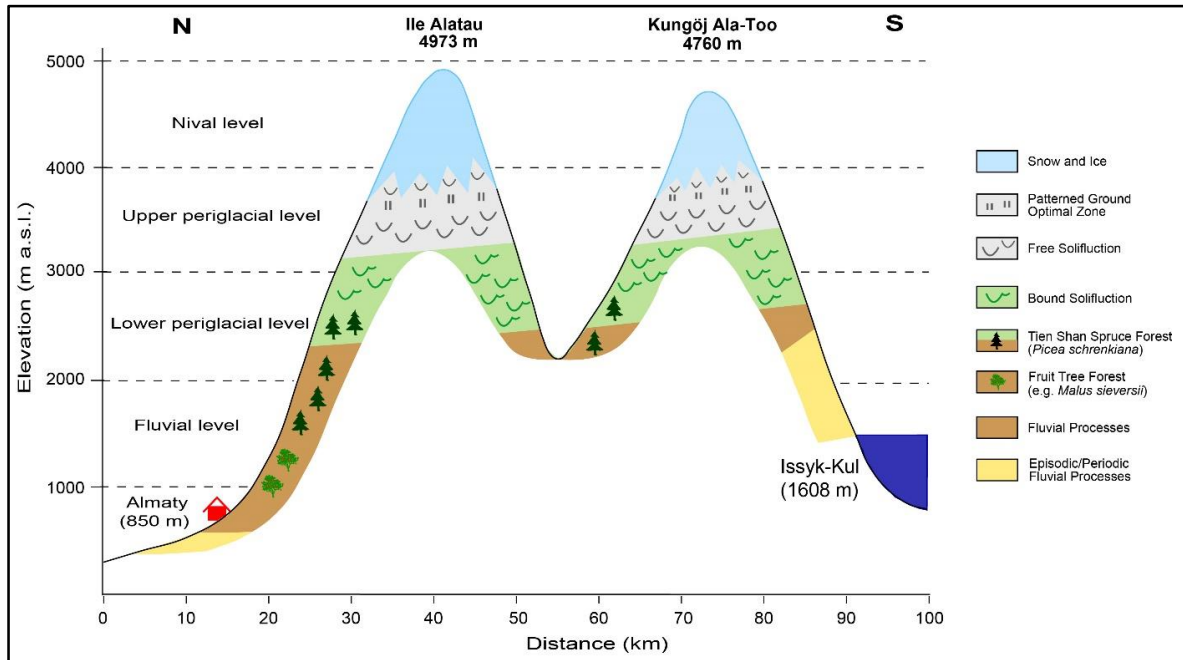


Figure 10: Geomorphological elevation zones. Figure translated from Bolch (2006).

Ice core analysis from Griegoriev Ice Cap in the Teskey Ala-Too Range suggests that present day Tien Shan glaciers are not remnants of the Last Glacial period but were formed during the Younger Dryas and the Holocene, and that mean summer temperatures during the Bølling-Allerød period were 2.7°C warmer than now (Takeuchi et al., 2014). Climate station records from 1879 to 2000 show a temperature increase with a sharp rise at the beginning of the 1970s (Bolch, 2007). From 1950-2000 the trend coefficient was approximately 2.0 K/100a, about twice the global average, although mountainous areas were less affected than lower regions (Bolch, 2007).

3.2.1 Rock Glaciers in Northern Tien Shan

Northern Tien Shan has a high concentration of rock glaciers and some particularly large and impressive examples. Over 1000 rock glaciers (about 850 of which were identified as active) were inventoried in Northern Tien Shan in the 1970-80s using aerial photography and field observations (Gorbunov et al., 1992; 1998). Gorbunov (1983) estimated there are 10 000 active rock glaciers in the mountains of Central Asia as a whole. Research of rock glaciers in Northern Tien Shan dates back as far as 1923, with descriptions of the size, morphology, lithology, genesis, and dynamics published primarily in Russian (e.g. Palgov, 1948; Goloskokov, 1949; Iveronova, 1950; Glazovskiy, 1978; Gorbunov, 1979;

Gorbunov & Titkov, 1989; Marchenko 2003). Usually found within an elevation range of 3000 to 3800 m a.s.l., rock glaciers in Northern Tien Shan have predominantly north-facing aspects in Ile Alatau and mostly south-facing aspects in Kungöj Ala-Too (Bolch & Gorbunov, 2014; Gorbunov et al., 1998).

Ongoing permafrost research in this region has been undertaken for over 40 years and is continued today by the Kazakhstan Alpine Permafrost Laboratory, which investigates and monitors permafrost and periglacial phenomena (Marchenko, 2003a; Marchenko et al., 2007) including borehole measurements which are part of the Circumpolar Active Layer Monitoring (CALM) initiative. Gorbunov and Severskiy (1998) estimated that the total ground ice volume for Northern Tien Shan is 56 km³, or about 62% of the surface ice volume for the same region. This large volume of permafrost is being affected by climate warming: observations over a 30-year timespan show an increase in permafrost temperatures from 0.3° to 0.6° C and an active-layer thickness increase of 23% (Marchenko et al., 2007). Modelling suggests the lower elevation limit of permafrost in the Ulken Almaty (Bolshaya Almatinka) and Kishi Almaty (Malaya Almatinka) valleys has shifted upwards by 150-200 m with an 18% loss in area over the course of the 20th century (Marchenko et al., 2007).

The most studied rock glaciers in this region are the Gorodetsky and Morenny, both found in the Ulken Almaty Valley. These two active, moraine-type rock glaciers are 750 m and 1200 m long, respectively (Gorbunov et al., 1992), and frontal advance rates have been previously published (Figure 11). The long term record of Gorodetsky rock glacier in particular shows a significant acceleration beginning around 1970 which may be related to concurrent air temperature warming (Bolch, 2006). Surficial velocities measured using traditional photogrammetric techniques at five rock glaciers in Northern Tien Shan, including Gorodetsky and Morenny, in the 1970s and 1980s ranged from 0.16 m/a to 14 m/a (Gorbunov et al., 1992). The surficial velocities are both spatially and temporally variable (Gorbunov et al., 1992).

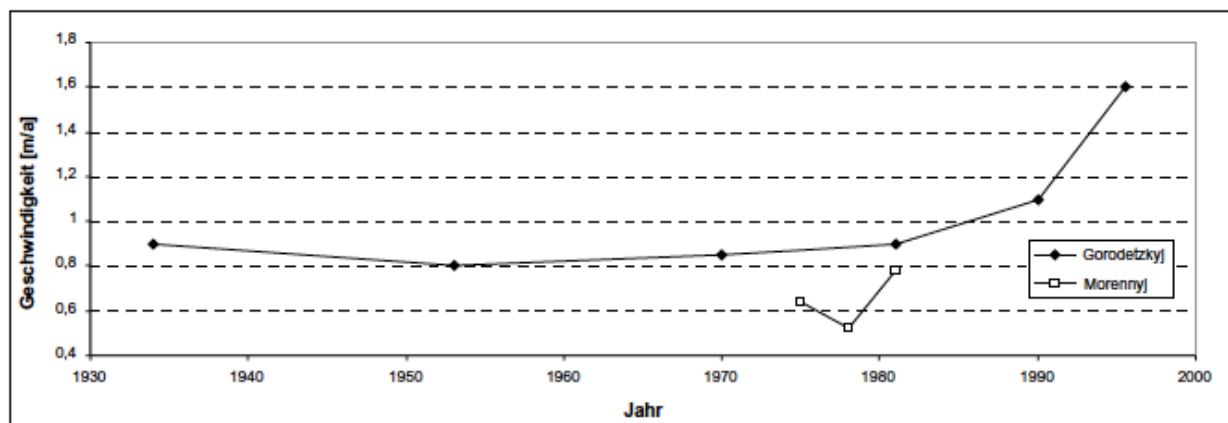


Figure 11: Frontal advance rates of Gorodetsky and Morenny rock glaciers. Figure from Bolch (2006), with base data from Gorbunov et al. (1992) and Marchenko (2003b).

3.2.2 *Glaciers in Northern Tien Shan*

Tien Shan Mountains are very dry but still have a relatively high concentration of glaciers for a mid-latitude region. In the entire Tien Shan, 7590 glaciers cover an area of 13 271 km² and comprise 1840 km³ ice (Aizen, 2011). The ELA is approximately 3800 m a.s.l. on northern slopes and slightly higher (3900-4000 m a.s.l.) on southern slopes (Bolch, 2007). Like most glaciated areas of the world, Tien Shan has experienced significant glacier retreat since the end of the Little Ice Age (LIA) (Solomina et al., 2004). Accelerated ice loss in Northern Tien Shan has been observed since 1970, corresponding to an increase in MAAT more so than a significant change in mean annual precipitation (MAP) (Aizen et al., 2007). Glacier change observations include a few *in situ* mass balance records (see Sorg et al., 2012 supplementary information), moraine-based glacier reconstructions (Solomina et al., 2004), remote sensing monitoring with comparisons to earlier maps and glacier inventories (e.g. Bolch, 2007; Narama et al., 2010), as well as GRACE gravimetric analyses (Jacob et al., 2012; Baumann, 2017). All results indicate a general trend of glacier frontal retreat, area loss, and volume wastage. For example, Bolch (2007) found that the glaciers in 6 valleys in Northern Tien Shan lost 32.6% of their total area from 1955 to 1999, with heterogeneous retreat rates influenced by size, location, and local climatic factors.

Glacier retreat in this region is likely to have ecological, social and economic implications, as discussed by Sorg et al. (2012). Large downstream populations depend on water resources originating in the Tien Shan Mountains for irrigation and hydropower (Bolch, 2017; Pritchard, 2017). These arid regions benefit from the buffering mechanism of glacially influenced river systems which shifts peak water flow towards the hot, dry summer months when ice melt runoff is greatest (Hagg et al., 2006). A loss of this mechanism would cause seasonal redistribution of runoff, and increase annual variability (Sorg et al., 2012). A complete loss of glacier ice in these catchments is predicted to cause summer water shortages (Hagg et al., 2006), exacerbated by rapidly growing water demand (Sorg et al., 2012). Potential downstream ecological impacts include desertification, and river/wetland ecosystem collapse (Sorg et al., 2012).

Glacier loss is also expected to impact geohazard risks in the region. With a hydrological regime shift from glacial-nival to nival-pluvial, extreme runoff events in spring may increase the frequency of floods and debris flows (Hagg et al., 2006). Glacier retreat is also associated with an increase in the number of potentially dangerous glacier lakes (PDGLs), increasing the likelihood of an outburst flood (Bolch et al., 2011).

3.3 Specific Study Area

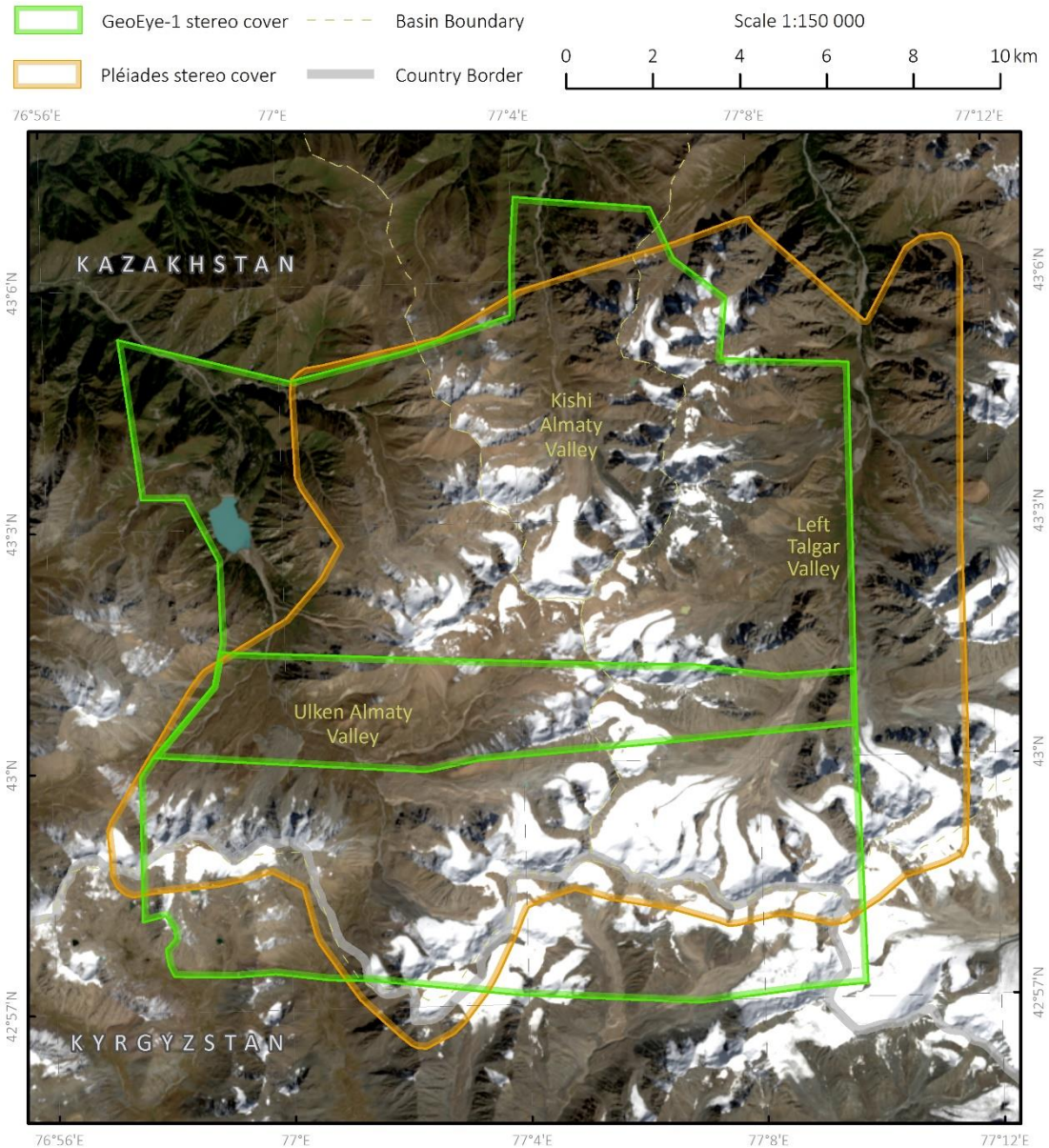


Figure 12: Overview of study area. Extent of GeoEye-1 (clipped to cloud-free areas) and Pléiades stereo imagery with pan-sharpened, true-colour Landsat 8 background (Landsat imagery Sept. 15, 2016).

The specific study area (Figure 12) lies on the northern side of Ile Alatau in Northern Tien Shan between 42.9° and 43.1° N and 76.9° and 77.2° E. The region comprises parts of three valleys, Ulken Almaty (Figure 13), Kishi Almaty (Figure 14) and Left Talgar (Lev Talgar; Figure 16), and in total covers approximately 200 km². While most of the study area is located in Kazakhstan, the southern edge includes the border and a small sliver of northern Kyrgyzstan. The study area is also partially within Ile-Alatau National Park, a protected area of Kazakhstan established in 1996. Water from this region flows via the Ile River to Lake Balkhash, about 350 km to the north. In the foothills of Ile-Alatau, only about 30 km from the study area, is the city of Almaty (population ~1.4 million). The high alpine environment provides important water

resources for the city as well as other nearby communities such as Talgar (population ~50 000), which lies about 25 km east of Almaty. This region was selected due to the presence of numerous glaciers and rock glaciers of varying sizes and the existence of previous research in these valleys which provides a background of information and data.

On the western side of the study area is the Ulken Almaty Valley (**Figure 13**) which contains the largest rock glaciers of the study area as well as numerous glaciers and the Bolshaya Almatinka Lake. The southern boundary ridge of this valley forms a section of the Kazakhstan-Kyrgyzstan border with elevations around 4200 m a.s.l. The high concentration of rock glaciers, including the previously discussed Morenny and Gorodetsky rock glaciers (3.2.1), may be related to slightly drier conditions (Bolch, 2006).

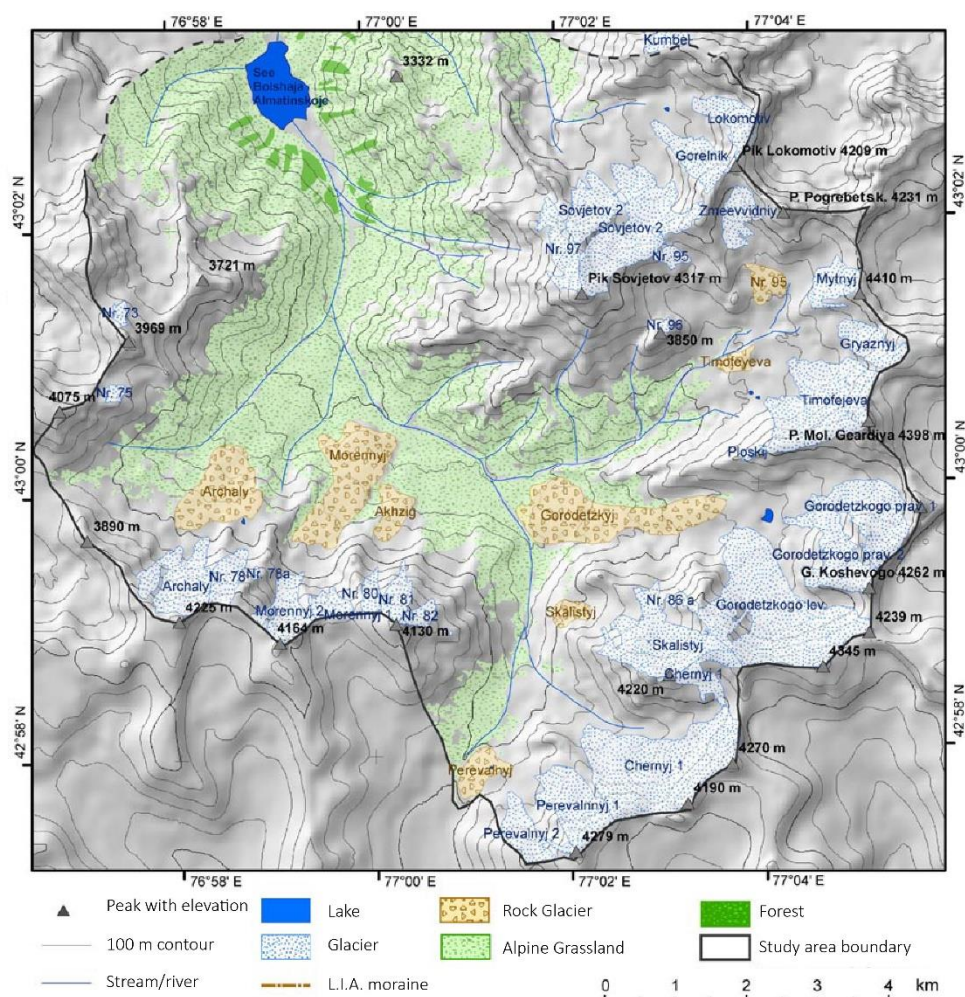


Figure 13: Ulken Almaty Valley. Figure translated from Bolch (2006).

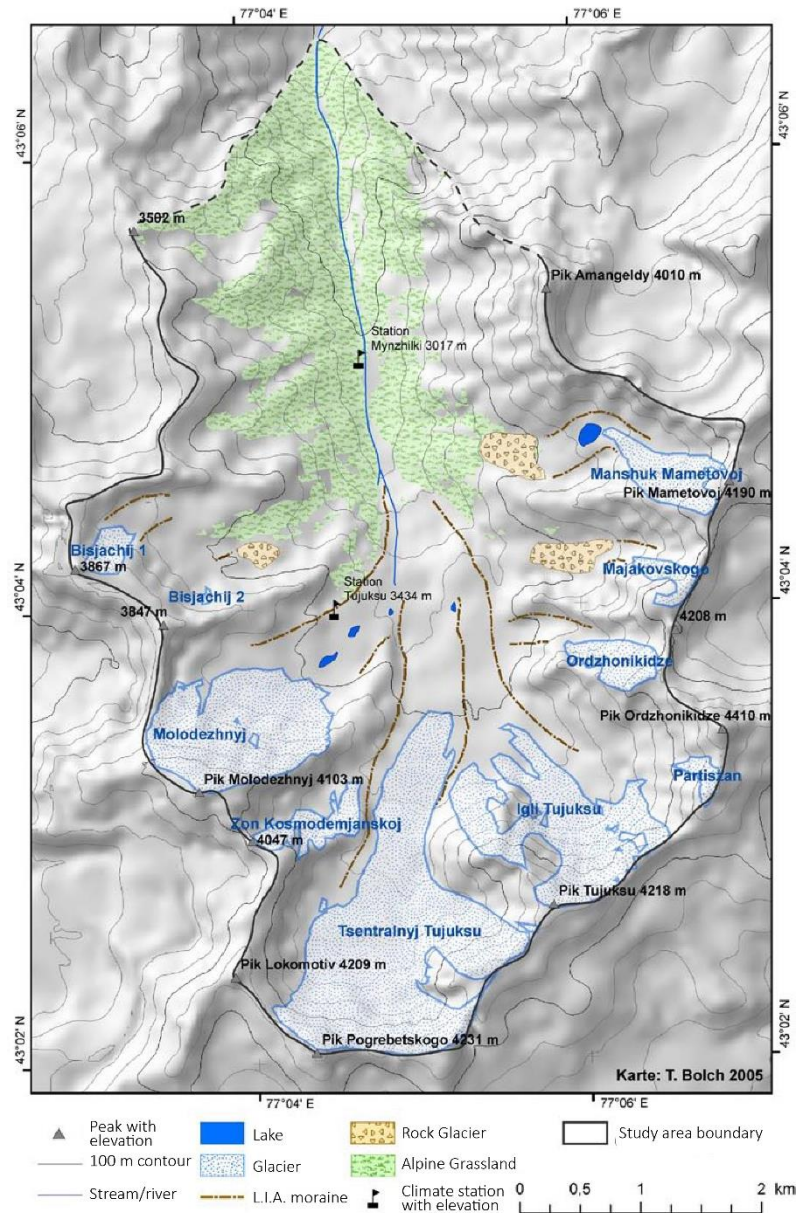


Figure 14: Kishi Almaty Valley. Figure translated from Bolch (2006).

In comparison, the slightly more humid Kishi Almaty Valley (Figure 14) has only a few small rock glaciers. Of the several glaciers in Kishi Almaty, the largest is the Tuyuksu Glacier (Tsentralniy Tuyuksuyskiy), a WGMS benchmark glacier, where a long-term mass balance record dates back to 1957 - the longest mass balance time series in Central Asia (Hagg et al., 2004). The Tuyuksu Glacier Station has collected stake measurements of accumulation and ablation, as well as snow density, ELA, glacier area, and climatic parameters such as temperature, precipitation, sunshine hours and cloudiness (Kogutenko et al., 2015). MAAT at the station (3434 m a.s.l.) is -4°C and the zero degree isotherm in the area is at just above 2700 m a.s.l. (Bolch & Gorbunov, 2014). Additional climate and data is collected at the Mynzhilki Climate Station (3017 m a.s.l.) further down valley. The Tuyuksu Glacier mass balance record shows a negative cumulative mass balance, the rate of which increased around 1970, corresponding to the regional shift in temperature

(Hagg, 2004). Kogutenko et al. (2015) compared this data to regional values and determined that the record does reliably reflect the regional trends of deglaciation. However, Savoskul and Smakhtin (2013) argued the high degree of variability even within the Kishi Almaty Valley alone (**Figure 15**), suggests a very high level of uncertainty when extrapolating single glacier measurements to the larger regional area.

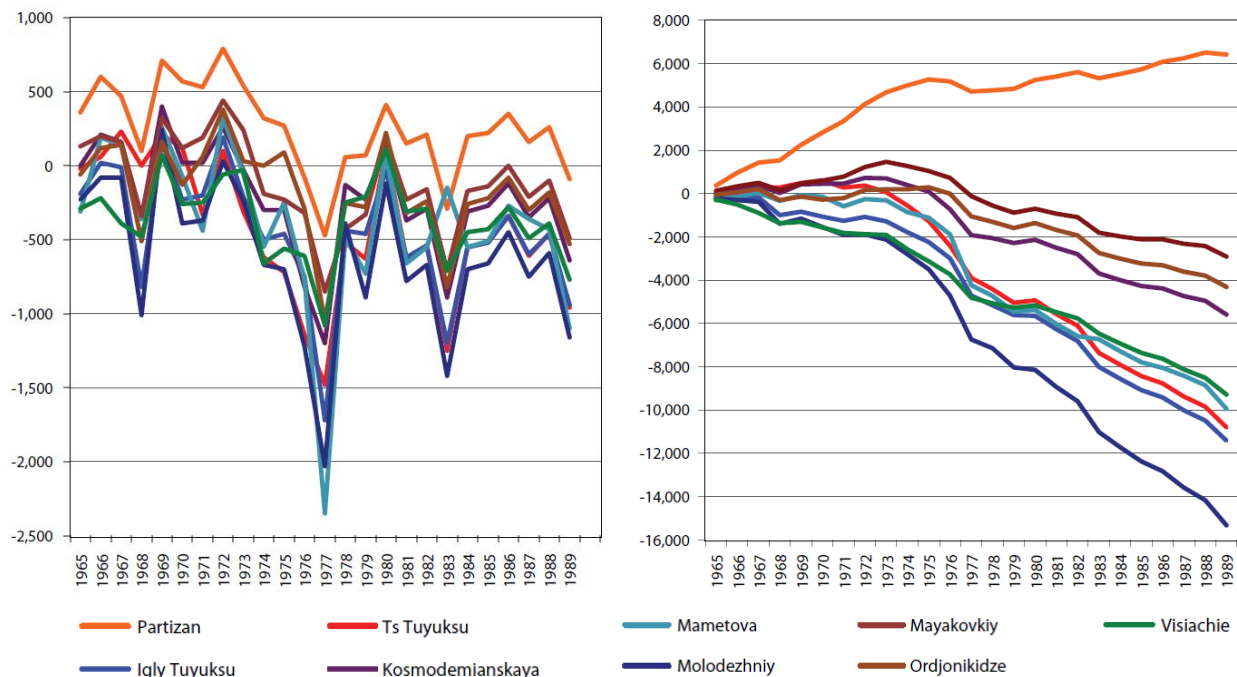


Figure 15: Kishi Almaty glacier mass balance variations (1965-1990). Specific mass balance at the ELA (left) and cumulative mass balance (right). Although correlation between the annual mass balance records is high, the cumulative difference between Tuyuksu Glacier and Partizan Glacier, for example, is very large. Figure from Savoskul and Smakhtin (2013).

The high resolution imagery also covers part of the Left Talgar Valley (**Figure 16**) on the eastern side of the study region. The crest of this valley, at an elevation of about 4300 m, also forms a section of the Kazakhstan-Kyrgyzstan border. Several large glaciers originate in the upper basin, including the Dmitrieva Glacier which was once one large glacier but has now split into several parts (Bolch, 2006). Left Talgar also contains several rock glaciers including the large Ordzhonikidze rock glacier on the western side of the valley.

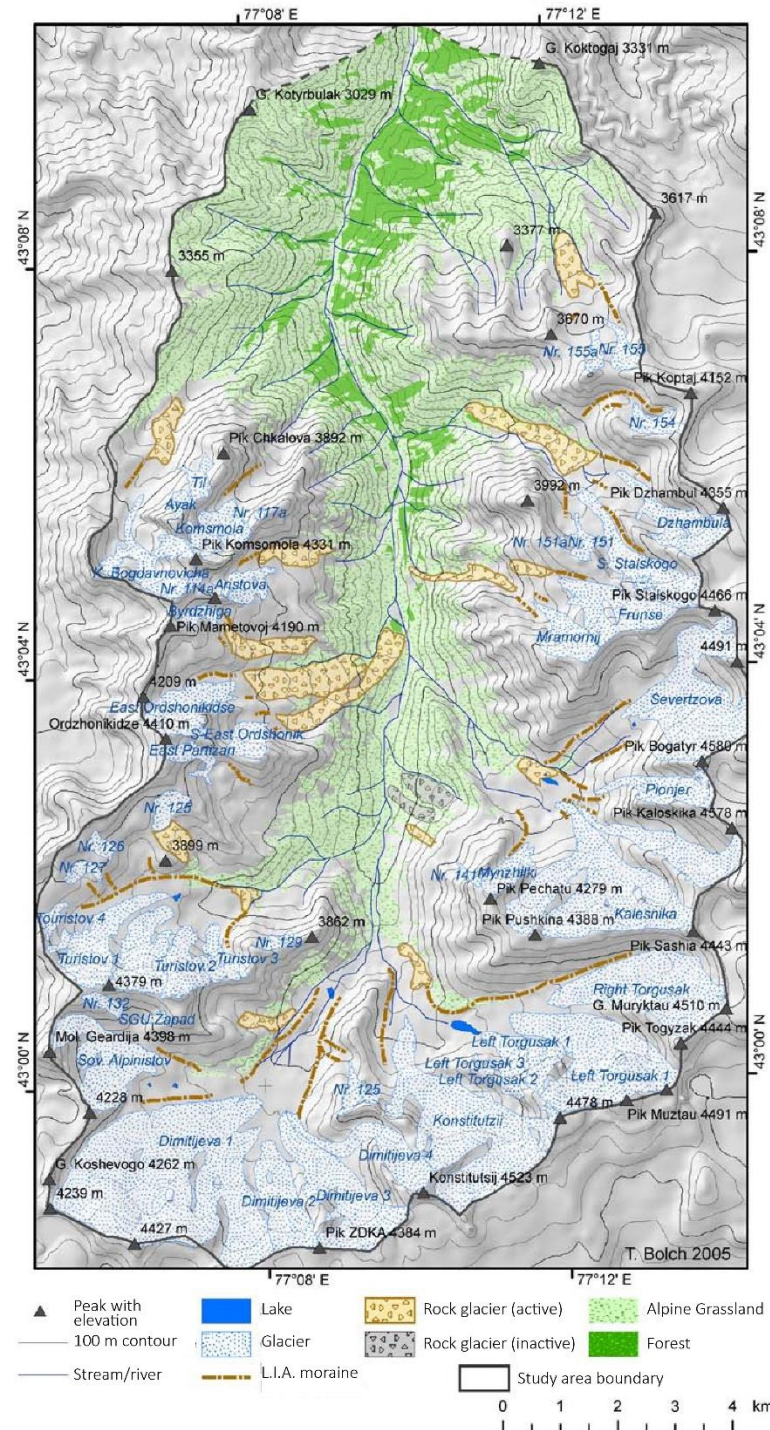


Figure 16: Left Talgar Valley. Figure translated from Bolch (2006).

Previous studies in this region used medium resolution satellite imagery and elevation models to investigate glaciers and rock glaciers. The maps above from Bolch (2006), include fewer rock glaciers and a lower level of detail than what is possible through the use of high-resolution imagery in this study. Bolch et al. (2006) used a 30 m resolution ASTER- and SRTM-based digital elevation model (DEM) for determining geomorphic parameters (elevation, aspect, slope angle, vertical curvature and tangential curvature) of glaciers and rock glaciers in Kishi Almaty, Ulken Almaty and Left Talgar (Table 1). Landsat ETM+, ASTER and

SRTM data were also used to examine the relationship between rock glacier size and contributing area parameters, finding that topographic characteristics could only partly explain rock glacier occurrence or area (Bolch & Gorbunov, 2014).

Table 1: Glacier and rock glacier characteristics using ASTER- and SRTM-derived DEM in the Kishi Almaty (Malaya Almatinka), Uken Almaty (Bolshaya Almatinka) and Left Talgar (Lev Talgar) valleys in Northern Tien Shan. Table from Bolch et al. (2005).

	Malaya Almatinka	Bolshaya Almatinka	Lev Talgar
Glaciers			
Total Area [km ²]	6,1	17,7	43,6
Portion of Study Area [%]	27,3	18,5	36,9
Elevation [m asl.]	3443 – 4329 Avg.: 3811	3390 – 4570 Avg.: 3870	3440 – 4575 Avg.: 3984
Slope [°]	0,3 – 64 Avg.: 24,3	0,1 – 79 Avg.: 27,5	0,1 – 79 Avg.: 22,4
Rockglaciers			
Total Area [km ²]	0,4	7,5	4,2
Portion of Study Area [%]	1,7	7,9	5,0
Elevation [m asl.]	3439 – 3654 Avg.: 3521	3000 – 3900 Avg.: 3425	2730 – 3882 Avg.: 3286
Slope [°]	4,4 – 27,8 Avg.: 11,7	0,2 – 53,3 16,5	0,9 – 44,5 15,6

3.4 A note on place names

Place names in this region have been changing since the dissolution of the Union of Soviet Socialist Republics (USSR). Alternative translations and spellings also lead to further variations in place names found on maps and in scientific literature. Where possible, up to date place names have been used. **Table 2** gives the names used in this study and former/variations of place name spelling as found in other sources.

Table 2: Names used in this study and former/additional names and alternative spellings.

Place names used in this study	Former/alternative place names in English & German publications
Almaty	Alma-Ata
Ulken Almaty	Bolshaya Almatinka, Bolschaja Almatinka, Big Almatinka, Großes Almatinka
Gorodetsky	Gorodetskyj, Gorodetskij
Isyk-Köl	Issyk-Kul
Ile Alatau	Zailiyskiy Alatau, Zailijskij Alatau, Sailsiiskii Alatau, Transili Alatau
Ile River	Ili River
Jengish Choqusu	Victory Peak, Pik Pobedy
Kungöj Ala-Too	Kungey Alatau, Kungej Alatau, Kungoy Alatau
Left Talgar	Lewyi-Talgar, Levyy-Talgar, linkes Talgar
Kishi Almaty	Malaya Almatinka, Malaja-Almatinka, Small Almatinka, kleines Almatinka
Morenny	Morennyj, Morennij
Teskey Ala-Too	Terskej Alatau
Tien Shan	Tianshan, Tian Shan, Tienschan, Tyen-Shan
Tuyuksu (Tsentralniy Tuyuksuyskiy)	Tujuksu, Tuyuk su

4 DATA

4.1 High resolution optical satellite stereo imagery

The primary datasets for observing glacier and rock glacier changes in the study area are high resolution imagery from Pléiades (4.1.1), GeoEye-1 (4.1.2), and CORONA (4.1.3) sensors.

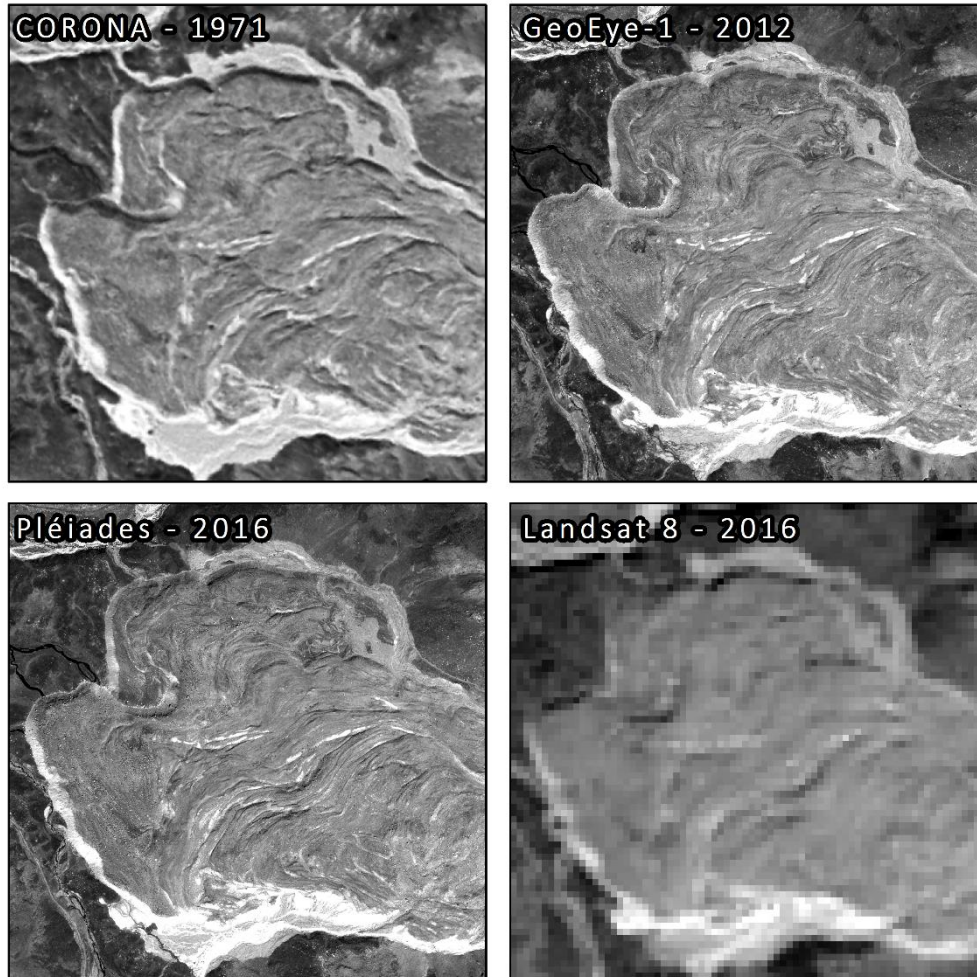


Figure 17: Gorodetsky rock glacier terminus as shown in high resolution imagery (CORONA, GeoEye-1, Pléiades). Medium resolution (15m pixel size) Landsat 8 OLI, panchromatic band 8 (Sept. 15, 2016) is shown for comparison.

4.1.1 Pléiades Stereo Imagery

The Pléiades constellation consists of two satellites (Pléiades 1A and Pléiades 1B) operating in the same orbit with a 180° phase difference. These satellites are part of a larger constellation comprising SPOT 6 and 7 satellites as well. Launched in 2011 and 2012 under a program headed by CNES, the Pléiades satellites are designed for both military and civilian use and offer high resolution imagery and an agile acquisition system. Single-pass stereo and even tri-stereo acquisition is possible, with daily access to any point on the globe.

Orbital Parameters	Bands	Optical System Parameters
Altitude: 694 km Period: 98.79 minutes Cycle: 26 days Sun-synchronous 10:30am descending node	Panchromatic: 0.47-0.83 μm Blue: 0.43-0.55 μm Green: 0.50-0.62 μm Red: 0.59-0.71 μm Near Infrared: 0.74-0.94 μm	Aperture diameter: 65 cm Focal length: 12.905 m Swath width: 20 km Dynamic range: 12 bit

Resolution	Acquisition Scenarios
Panchromatic: Nadir GSD = 0.7 m Resampled product = 0.5 m Multispectral: Nadir GSD = 2.8 m Resampled product = 2.0 m	Target collection Multiple acquisitions Single-pass strip mapping Stereo & Tri-stereo Corridor acquisition Persistent surveillance mode

Figure 18: Pléiades satellite and sensor overview.

The Pléiades imagery for this project covers an area of approximately 257 km² and was acquired by Pléiades 1B on August 27th, 2016 at 5:45 GMT. The primary product is corrected for radiometric and sensor distortions using internal calibration parameters, ephemeris, and attitude measurements (Astrium, 2012). The imagery is provided in sensor geometry with equalized radiometry and is resampled by a factor of 7/5 (Astrium, 2012). It is not orthorectified or pan-sharpened. The product is provided in DIMAP V2 format with the associated Rational Polynomial Coefficients (RPCs). Image files are JPEG 2000 with 12-bit pixel depth encoding.

4.1.2 GeoEye-1 Stereo Imagery

The GeoEye-1 satellite, launched in 2008, has a slightly finer ground sampling distance (GSD) than the Pléiades satellite but the imagery is also resampled to 0.5 m (panchromatic) and 2.0 m (multispectral). Similar to the Pléiades satellites, GeoEye-1 can collect single-pass stereo imagery (although not tri-stereo) and collects both panchromatic and 4-band multispectral images.

The GeoEye-1 imagery for this project covers an area of approximately 400 km² and was acquired on August 9th, 2012 at 5:37 GMT. The stereo images are radiometrically corrected and rectified to an epipolar projection. Images are provided in TIFF format with the associated Rational Polynomial Coefficients (RPCs). The images are tiled: one stereo pair covers the northern portion of the study area and one stereo pair covers the southern portion. Clouds obscure some of the outer areas, especially in the northern and western parts of the imagery.

Orbital Parameters	Bands	Optical System Parameters
Altitude: 681 km Period: 98 minutes Cycle: 26 days Sun-synchronous, 10:30am descending node	Panchromatic: 0.45-0.80 μm Blue: 0.45-0.51 μm Green: 0.51-0.58 μm Red: 0.655-0.69 μm Near Infrared: 0.78-0.92 μm	Aperture diameter: 110 cm Focal length: 13.3 m Swath width: 15.3 km Dynamic range: 11 bit

Resolution	Acquisition Scenarios
Panchromatic: Nadir GSD = 0.41 m Resampled product = 0.5 m Multispectral: Nadir GSD = 1.65 m Resampled product = 2.0 m	Long strip Large area collection Multiple point targets Stereo area collection

Figure 19: GeoEye-1 Satellite and Sensor Overview.

4.1.3 CORONA Stereo Imagery

The CORONA reconnaissance satellites operated between 1960 and 1972, flying 94 successful missions (Table 3) which provided the earliest stereoscopic imagery from space. Several mission iterations (designated by 'keyhole' naming KH-1 to KH-4B) carried successively improved sensor systems reaching ground resolution as high as 1.83 m (USGS, 2008). The CORONA missions were followed by ARGON (KH-5) and LANYARD (KH-6). Developed for the purpose of military reconnaissance, the images remained classified until they were released to the public in 1995, providing an extended record of medium to high resolution imagery for a wide range of applications. Scanned digital images are distributed by the USGS for low costs.

Table 3: CORONA mission information (USGS, 2008).

Keyhole Name	Dates	Best Ground Resolution	Cameras	Frames	Mission Numbers
KH-1	Jun. 1959 – Sep. 1960	12.2 m (40 ft)	Single panoramic	1,432	9009
KH-2	Oct. 1960 – Oct. 1961	9.1 m (30 ft)	Single panoramic	7,246	9013, 9017, 9019
KH-3	Aug. 1961 – Jan. 1962	7.6 m (25 ft)	Single panoramic	9,918	9022, 9023, 9025, 9028, 9029
KH-4	Feb. 1962 – Dec. 1963	7.6 m (25 ft)	Two panoramic cameras (stereo)	101,743	9031, 9032, 9035, 9037-9041, 9043-9045, 9047, 9048, 9050, 9051, 9053, 9054, 9056, 9057, 9062
KH-4A	Aug. 1963 – Oct. 1969	2.7 m (9 ft)	Two panoramic cameras (stereo)	517,688	1001, 1002, 1004, 1006-1031, 1052
KH-4B	Sep. 1967 – May 1972	1.8 m (6 ft)	Two panoramic cameras (stereo)	188,526	1101-1112, 1114, 1006-1117

The last CORONA mission, KH-4B, had forward- and aft-facing panoramic cameras tilted at 15° , giving 30° convergent stereo images. Although this system achieved high ground resolution and had a sufficient base to height ratio for stereoscopic elevation extraction, DEM generation from this imagery is more complicated than from modern optical stereo sensors. The panoramic cameras produced non-planar image geometry with a characteristic bow-tie shaped distortion pattern (**Figure 20**). Image and satellite metadata such as fiducial marks, principle point, and ephemeris data are not available, making correction of these geometric distortions more difficult. Wilson (2015) provides an overview of photogrammetric approaches used in various studies to correct CORONA imagery for DEM generation. Rigorous mathematical modelling can be applied to solve interior and exterior orientation parameters (e.g. Sohn et al., 2004). Alternatively, an empirical approach approximates camera parameters based on known values (flying height, focal length, film scanning resolution) and GCPs in a non-metric cameral frame model (e.g. Altmaier & Kany, 2002; Schmidt et al., 2001).

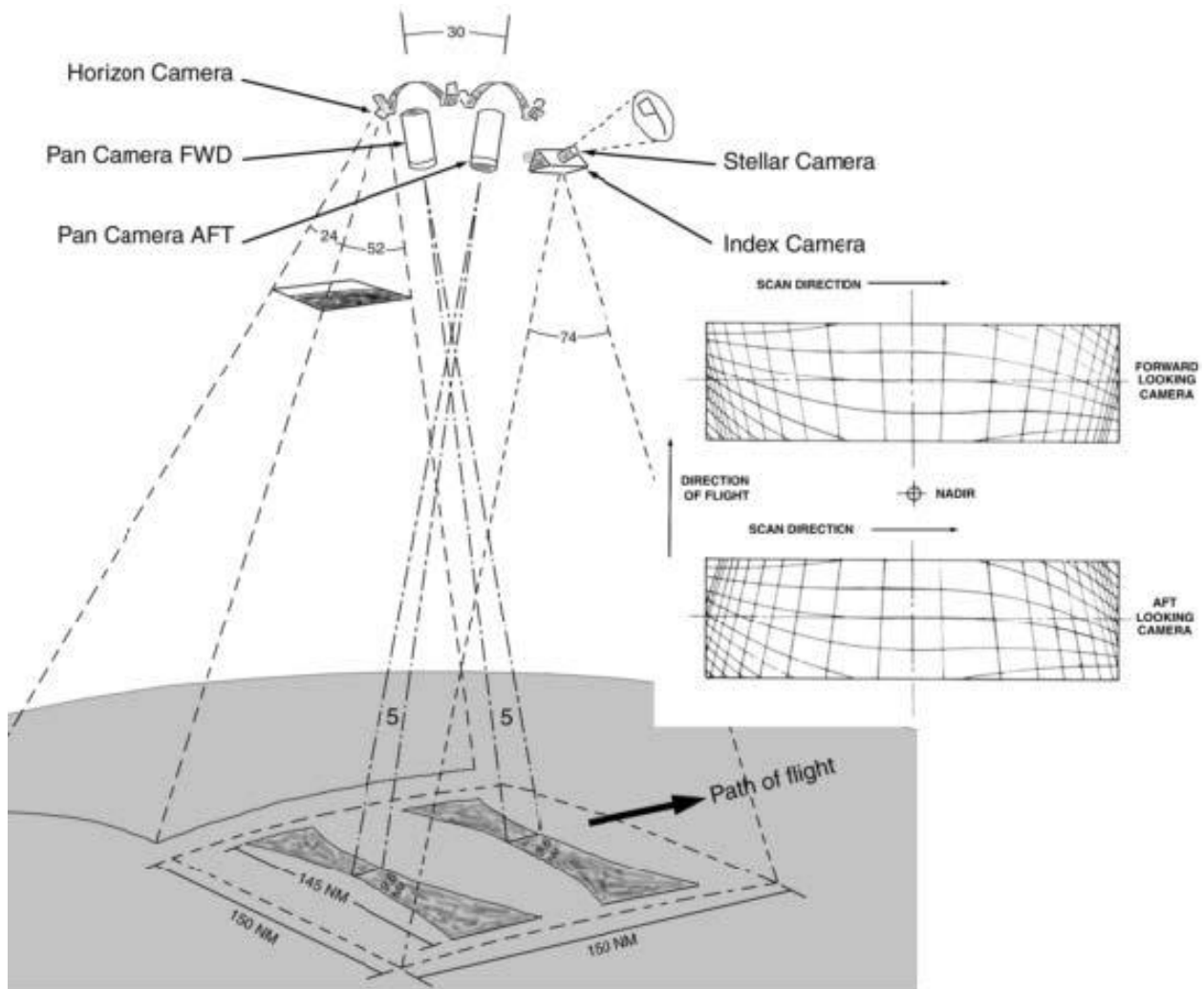


Figure 20: CORONA camera arrangement and shape of ground footprint showing geometric distortions. Figure from Galiatsatos et al. (2007).

For this project, four CORONA images (Figure 22) acquired on September 17, 1971, are used to produce elevation data and ortho-imagery to allow for multi-decadal change detection. The study area is located near the center for the images meaning that image distortion is relatively low. The imagery is available through the USGS, and is provided as a tiled image in four parts, with a scan resolution of 21 μm . Each frame covers a ground area of 14 km x 188 km, and therefore a subsection was established for the region of interest.

Satellite & Mission	Optical System Parameters	Images
System: CORONA KH-4B Mission: 1115-1 Date: September 17, 1971 Flying Altitude: 150 km	Camera type: Panoramic Bands: 1, panchromatic Focal length: 60.69 cm Frame format: 5.54 x 75.69 cm	Ground area: 14 x 188 km Scan resolution: 7 or 14 μm Spatial reference: none

Figure 21: CORONA KH-4B satellite and sensor overview (USGS, 2008).

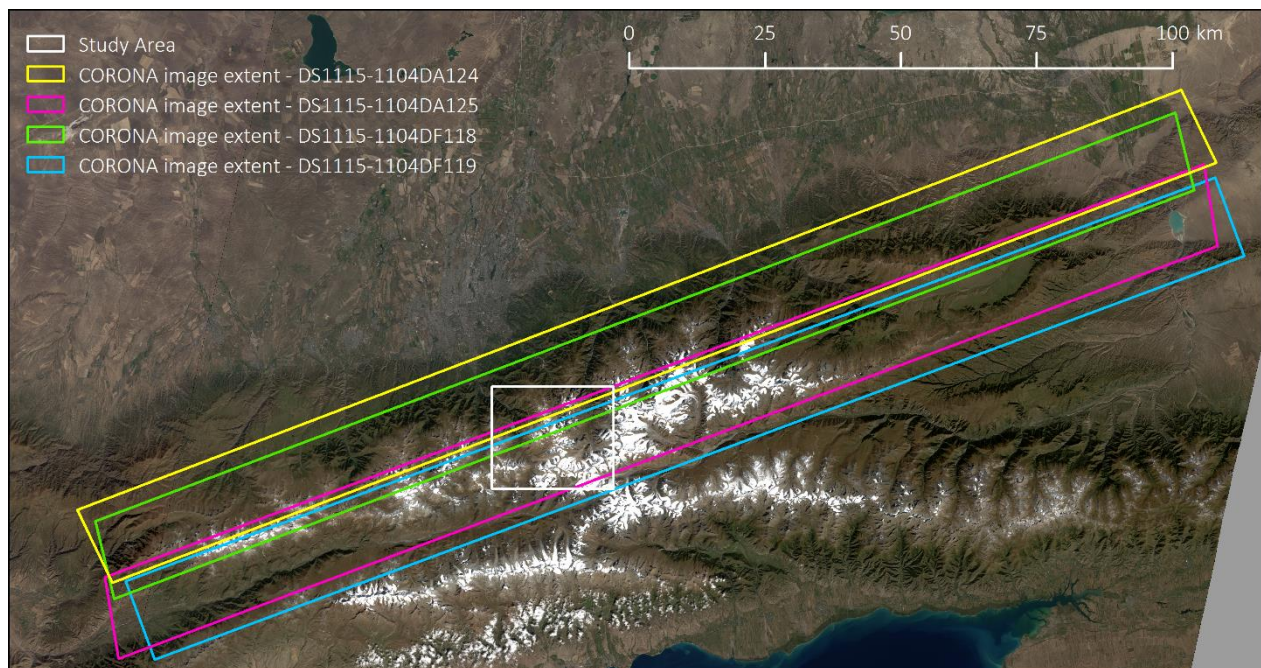


Figure 22: Extent of CORONA Imagery frames with Landsat 8 background (Landsat imagery Sept. 15, 2016).

4.2 Additional datasets

Field collected GCPs

GCPs were measured in the summer of 2016 using an Ashtech GPS receiver. Accuracy of these GPS measurements is estimated to be about 1 m horizontal and about 3 m vertical. Only a few of the points were within the study area and some were not identifiable in the earlier imagery. Where possible, they were incorporated into the DEM generation process.

SRTM 1 Arc-Second DEM

The Shuttle Radar Topography Mission was flown in February, 2000, and used synthetic aperture radar (SAR) to produce a near global DEM. The 1 arcsecond (30m) resolution DEM, available from USGS, was used as reference elevation data for GCP collection and DEM generation. The SRTM DEM has been used in similar studies as a reference for DEM generation or as a comparison to other elevation data for surface elevation change detection (e.g. Galiatsatos et al., 2007; Bolch, 2015).

Landsat imagery – LC81490302016259LGN00

The Landsat program has collected imagery of earth's surface for over four decades. The most recent satellite, Landsat 8, is equipped with the Operational Land Imager (OLI) and the Thermal Infrared Sensor (TIRS). The panchromatic OLI band 8 has the highest resolution (15m pixel size) and orthorectified images are freely available from the USGS. An image from September 15, 2016 (LC81490302016259LGN00) was used as a reference for GCP collection and mapping.

Google Earth imagery

Google Earth satellite imagery is freely available and easy to view in 2D or 3D online. Imagery sources and resolution varies spatially and information about spectral and spatial properties is not easily available, making accuracy more difficult to quantify (Schmid et al., 2014). In this study, Google Earth imagery was used to aid in GCP identification and for mapping of rock glaciers where delineation was unclear.

Randolph Glacier Inventory (RGI) 5.0

The Randolph Glacier Inventory (Arendt et al., 2015) is a global collection of digitized outlines of the world's glaciers, not including the polar ice sheets (Pfeffer et al., 2015). In this region, the data is sourced from the GAMDAM inventory (Nuimura et al., 2015). These shapefiles were used for reference, but new glacier delineations were manually completely based on the high imagery.

InSAR-derived rock glacier inventory

Using interferometric synthetic aperture radar (InSAR), this inventory includes rock glaciers and other periglacial processes, including solifluction, dead ice/subsidence, debris covered glaciers, and landslides (Strozzi et al., 2017; Wang et al., 2017). A classification of displacement rates divides these features into cm/year, cm/month, dm/month, or undefined. These polygons were used to help identify areas of stable vs. unstable terrain for DEM co-registration, and also to aid in rock glacier identification from the optical imagery.

Tuyuksu (Tsentralniy Tuyuksuyskiy) Glacier mass balance record

A consecutive mass balance record for Tuyuksu glacier in Kishi Almaty valley dates back to 1957. The principal investigators are N. Kasatkin, K. Makarevich & Colleagues at the Institute of Geography, National Academy of Science of the Kazakh Republic. The data was accessed through the WGMS website which compiles and disseminates glacier data from around the world.

5 METHODOLOGY

5.1 Digital Elevation Model (DEM) generation

5.1.1 Pléiades and GeoEye-1 DEM generation

DEMs were generated using the ERDAS IMAGINE Photogrammetry (Hexagon Geospatial) workflow. GCP coordinates were first identified in ArcMap and were based on a combination of a few field-collected GPS points and points identifiable in Landsat 8 panchromatic imagery (15 m resolution), with elevation data from the 1 arcsecond SRTM DEM (projected to UTM 43N with 30m pixel size). In some instances, Google Earth was used to improve point location within a 15m Landsat pixel. Approximately 10 GCPs were used per image pair. The following workflow was completed for the Pléiades imagery and the two GeoEye-1 tiles:

- i. Setup new photogrammetric project:
 - Create block file and choose appropriate sensor-specific geometric model.
 - Set horizontal coordinate system and vertical reference system (UTM 43N, WGS84).
- ii. Import panchromatic images.
- iii. Attach RPC files to set interior and exterior orientation parameters.
- iv. Import GCPs in Classic Point Measurement tool and locate positions in both images (**Figure 23**).
- v. Perform Automatic Tie Point Generation and Tie Point Uncertainty Analysis – manually check, add, and remove tie points as necessary.
- vi. Perform Triangulation to refine rational functions and check RMSE results (**Table 4**).
- vii. When total image RMSE is sufficient, perform Automatic Terrain Extraction (ATE).
- viii. Clip resulting DEMs in ArcMap to remove edge artifacts.

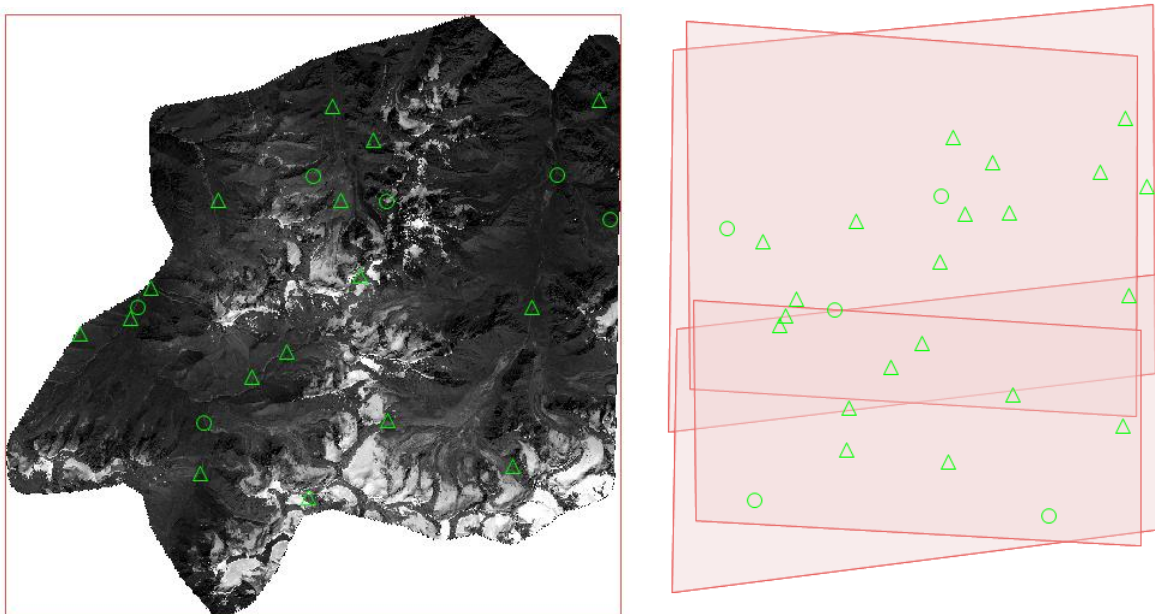


Figure 23: Control points (triangles) and check points (circles) identified using the Classic Point Measurement tool in ERDAS IMAGINE Photogrammetry. Pléiades imagery (left) and GeoEye-1 tile outlines (right).

Table 4: ERDAS IMAGINE Photogrammetry triangulation results for Pléiades (PL) and GeoEye-1 (GE) image blocks.

Image Block	Total Image RMSE (pixel)	Point Type (#)	X Residuals (m)			Y Residuals (m)			Z Residuals (m)			CE90 (m)	LE90 (m)
			Mean	RMSE	Min Max	Mean	RMSE	Min Max	Mean	RMSE	Min Max		
PL	1.44	GCP (12)	-0.23	1.67	-3.34 3.44	-0.01	2.37	-2.91 6.40	-0.00	5.06	-7.84 8.18	4.55	8.72
		CP (3)	-1.78	2.62	-3.39 0.93	-1.89	2.08	-3.09 -1.17	2.16	3.62	-0.42 6.21	5.16	4.84
GE	1.01	GCP (19)	-0.04	2.40	-5.00 5.99	-0.03	1.82	-2.75 3.55	-0.19	4.07	-5.82 8.26	4.65	6.86
		CP (5)	-0.47	1.93	-3.33 1.57	-0.03	1.21	-1.09 1.90	0.57	5.05	-5.61 7.57	3.80	9.17

The DEM generation process was repeated multiple times using variations of different settings, different numbers of GCPs and TP, and different output resolutions. In the end, mostly default values were used for the Automatic Terrain Extraction (ATE). Attempts to use the Enhanced Automatic Terrain Extraction (eATE) repeatedly failed for unknown reasons. The final DEMs used in later analysis were generated at 5m resolution. ERDAS IMAGINE Photogrammetry DEM Extraction Reports show generally good accuracy results for GCPs, CPs and TP (Table 5). One exception is the accuracies reported for the TP of GE 2, which were heavily influenced by 6 tie points near the image border where edge effects caused erroneous values. The other 200 TP values are within a normal range and the problematic edge region was later removed.

Table 5: ERDAS IMAGINE Photogrammetry Automatic Terrain Extraction report for Pléiades (PL) and GeoEye-1 (GE) DEMs. (NIMA Absolute LE90 = U.S. National Imagery and Mapping Agency Absolute Linear Error 90.)

DEM Designation	General Mass Point Quality	Point Type (#)	Block Point to DTM vertical accuracy (m)				Absolute LE90 (m)	NIMA Absolute LE90 (m)
			Mean Error	Mean Absolute Error	RMSE	Min, Max		
PL	Excellent (1-0.85): 69.2 % Good (0.85-0.70): 30.6 % Fair (0.70-0.5): 0.2 % Isolated: 0.0 % Suspicious: 0.0 %	GCP (12)	-1.68	4.70	5.34	-10.13, 5.98	8.22	± 4.18
		CP (3)	0.09	2.87	3.04	-4.17, 2.74	4.17	± 1.67
		TP (185)	-0.19	1.34	1.88	-8.30, 5.88	3.06	± 2.16
GE 1	Excellent (1-0.85): 61.5 % Good (0.85-0.70): 37.7 % Fair (0.70-0.5): 0.9 % Isolated: 0.0 % Suspicious: 0.0 %	GCP (14)	-0.60	2.93	3.90	-5.85, 10.21	5.85	± 4.22
		CP (4)	-2.52	4.14	5.62	-10.37, 3.23	10.37	± 6.25
		TP (237)	-0.12	1.37	2.01	-9.51, 10.33	3.09	± 2.41
GE 2	Excellent (1-0.85): 69.0 % Good (0.85-0.70): 30.5 % Fair (0.70-0.5): 0.5 % Isolated: 0.0 % Suspicious: 0.0 %	GCP (8)	-0.30	4.70	4.85	-8.07, 6.78	8.07	± 2.02
		CP (1)	7.58	7.58	7.58	7.58, 7.58	7.58	± 0.00
		TP (206)	-24.89	26.07	149.82	-1049.15, 7.15	3.52	± 242.85

5.1.2 CORONA imagery

For better results creating DEMs from CORONA imagery, the Remote Sensing Software Package Graz (RSG) was used. RSG, developed by Joanneum Research Graz, has previously been shown to produce good results for CORONA DEMs (e.g. Bolch et al., 2008; Goerlich et al., 2017; Pieczonka et al., 2011). The software includes a CORONA-specific image distortion model which allows for correct geometric modelling.

From the four CORONA images, 3 stereo pairs were created to cover the entire study region (Table 6). Tiled CORONA imagery was first merged and subset using Adobe Photoshop and ERDAS IMAGINE. GCPs generated in ArcMap from Landsat and SRTM reference data (14-15 per image) were identified in the CORONA imagery using ERDAS IMAGINE before starting the workflow in RSG. Where possible, the same GCPs were used as for the Pléiades and GeoEye-1 DEMs, although not all GCPs were identifiable in the CORONA imagery due to the lower resolution and changes in the landscape over several decades.

Table 6: CORONA DEM Image stereo pairs. One forward image (DS115-1104DF118) was used twice, with two separate aft images.

DEM designation	Forward Image ID	Aft Image ID	% Overlap
Cor 1	DS1115-1104DF118	DS1115-1104DA124	77
Cor 2	DS1115-1104DF118	DS1115-1104DA125	27
Cor 3	DS1115-1104DF119	DS1115-1104DA125	81

For each image pair, the following steps were taken in the RSG environment:

- Import imagery into RSG.
- Define known exterior orientation parameters (Table 7).
- Import GCPs and image coordinates.
- Perform single image geometric modelling for both images to adjust geometric parameters including camera position/orientation based on GCPs.
- Create stereo model image block and perform stereo parameter adjustment (Table 8).
- Run automatic tie point acquisition for relative orientation.
- Perform epipolar registration to create stereo model in epipolar coordinates.
- Perform forward and backward disparity predictions.
- Run image matching using the disparity prediction method and the output rasters of step viii.
- Filter and interpolate disparity raster.
- Perform disparity to height conversion.
- Interpolate DEM Raster.

Table 7: Default scene parameters. ω is viewing angle across flight direction, ϕ is forward and backward camera tilt, κ is flight direction (0° = east).

Scene	Omega (ω)	Phi (ϕ)	Kappa (κ)	Flying Height (km)	Focal Length (mm)
Forward	0°	15°	61°	200	609.602
Aft		-15°			

Table 8: GCP residuals following stereo parameter adjustment.

Image Block	# GCP	Image Id	Res X (pixels)			Res Y (pixels)			Res Length (pixels)		
			RMS	Min	Max	RMS	Min	Max	RMS	Min	Max
Cor 1	15	DF118	1.93	-2.67	4.10	0.96	-2.01	2.31	2.16	0.51	4.15
		DA124	2.68	-4.70	4.96	2.35	-3.52	3.41	3.56	0.55	5.75
Cor 2	14	DF118	0.64	-1.15	1.10	0.97	-2.08	1.86	1.16	0.01	2.14
		DA125	0.63	-1.02	1.15	0.90	-2.15	1.46	1.10	0.15	2.36
Cor 3	15	DF119	1.32	-3.08	1.77	0.80	-1.68	1.31	1.55	0.48	3.27
		DA125	1.24	-1.98	2.32	0.97	-1.70	2.02	1.57	0.15	2.61

CORONA DEMs were generated at a spatial resolution of 5m. Considering the image resolution and the accuracy of the GCPs, the ideal DEM resolution would likely be 2-3 times larger (~10-15m). Producing 5m DEMs may have introduced some artifacts but in general the results were satisfactory and allowed for a comparison with Pléiades and GeoEye-1 DEMs at 5m resolution instead of resampling the higher resolution results to match the CORONA DEMs. During the DEM raster interpolation, small holes in the data were interpolated and filtered using the tools available in RSG. These holes, which were primarily located in the low contrast areas of the accumulation zone, could have been handled in a more statistically robust way, or left excluded in further processing to avoid introducing additional error. In general, the holes were small and the overall influence of interpolation is likely low. However, errors in the accumulation area are noticeable in the elevation difference rasters suggesting that better management of data gaps would be a possible point for improvement.

5.2 DEM co-registration

DEM co-registration is necessary to ensure accuracy when differencing multi-temporal DEMs, as even a sub-pixel misalignment can lead to significant error (Paul et al., 2015). Two different implementations of co-registration methods based on Nuth and Kääb (2011) were undertaken. The first method (5.2.1) applies x-, y- and z-shifts to reposition one DEM raster relative to another. The second method (5.2.2) first corrects for surface trends and then repositions the DEM.

Both methods rely on a comparison of a *master* DEM and a *slave* DEM in areas which are assumed to be stable terrain, where minimal surface elevation change is expected over decadal time scales. A polygon shapefile was created in ArcMap by combining several geodatasets of likely *unstable* terrain (Figure 24), namely glaciers and rock glaciers. The Randolph Glacier Inventory (RGI) glacier outlines, as well as the manually delineated CORONA glacier outlines, were combined with manually delineated rock glacier

polygons and the InSAR-derived polygons of Strozzi et al. (2007). The polygon files were merged, dissolved, and clipped to create one multi-part feature.

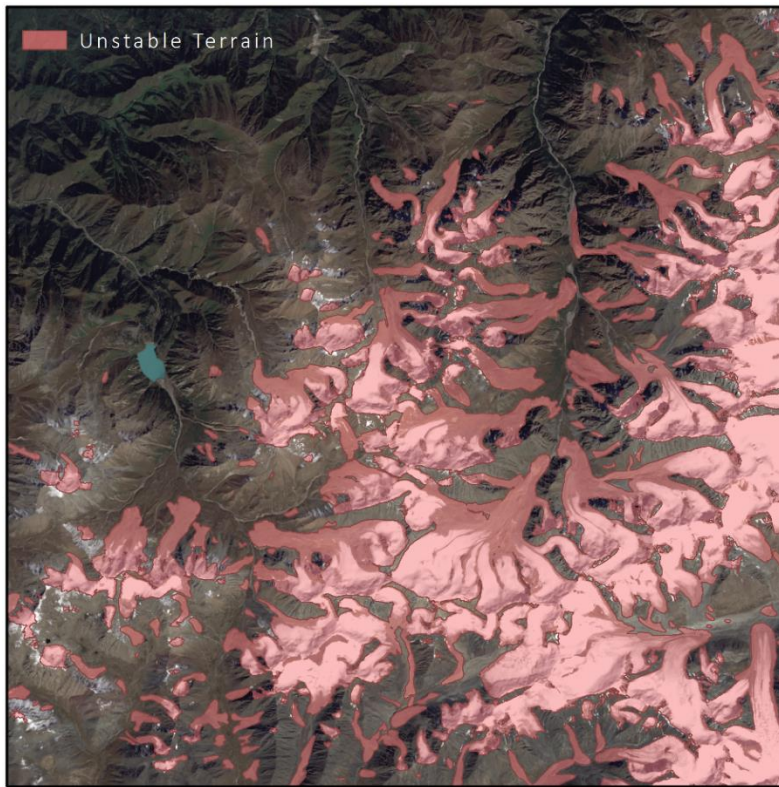


Figure 24: Unstable terrain polygon with Landsat background.

5.2.1 DEM co-registration by horizontal and vertical shifts

This method of co-registration is based on Nuth and Kääb (2011) and relies on the relationship between the elevation difference (dh) of two DEMs and the corresponding slope and aspect at each point. The direction of the horizontal shift is determined by the aspect with the highest positive bias in dh , and the magnitude of the bias is related to the slope (Nuth and Kääb, 2011; Figure 25). The shift is found by minimizing the residuals between the two sides of Equation 1 using a set of locations with dh , slope, and aspect values as shown in Figure 25.

$$\frac{dh}{\tan(\alpha)} = a \cdot \cos(b - \varphi) + c \quad (1)$$

Where: α = terrain slope
 φ = terrain aspect
 a = co-registration vector magnitude
 b = co-registration vector direction
 c = mean bias between the DEMs divided by the mean slope of the selected terrain

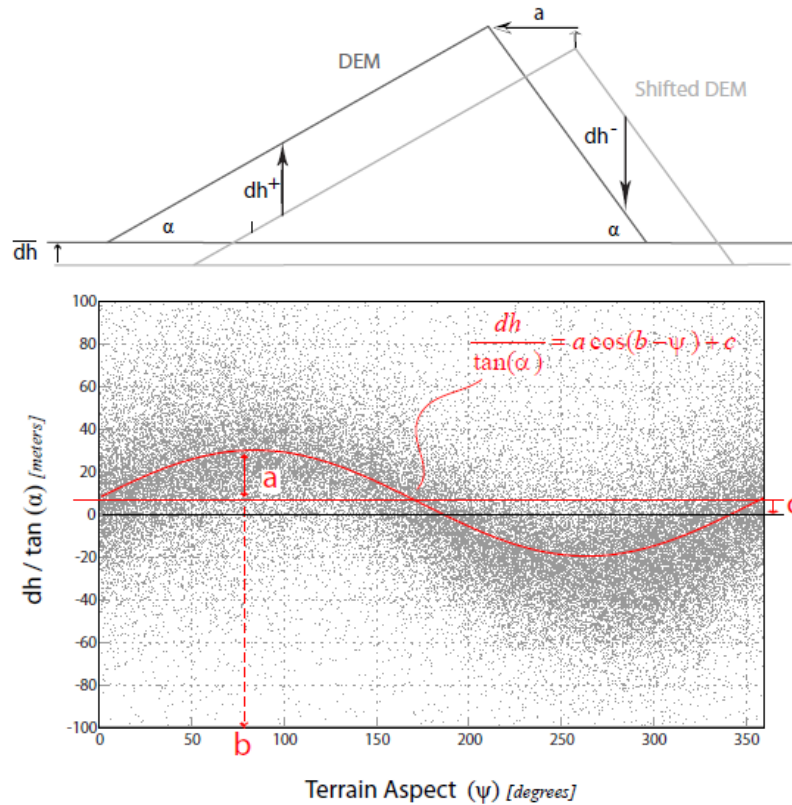


Figure 25: Co-registration method of Nuth and Käb (2011). The top diagram shows how the horizontal/vertical shift of a DEM will affect dh values. The scatter plot illustrates the relationship between dh normalized to the slope tangent (y-axis) and terrain aspect (x-axis). The equation for the sinusoidal curve is shown along with the three unknown solution parameters: a , b , and c . From these parameters the x , y and z shift of the slave raster can be calculated. Figure from Nuth and Käb (2011).

Multiple iterations of this process may be required to find the final solution, and so the process is repeated until the standard deviation of dh values improves by less than 2%, or some other threshold value.

To implement this process, a number of steps were taken in ArcGIS to calculate dh , slope and aspect values before exporting a sample set of values to Excel to find a solution for the above equation. First, the master DEM was clipped to stable terrain and used to create slope and aspect rasters. Only slope values between 10° and 45° were included as DEM errors tend to be greater at steeper slopes.

For easy repetition of steps for multiple slave rasters and multiple iterations, ModelBuilder was used (Figure 26). The input to the model is a directory containing the slave rasters. Each slave is resampled (using bilinear resampling) and snapped to the pixel grid of the master DEM. A raster of dh values is created by subtracting the slave DEM from the master DEM and is limited to values within a range of $\pm 50\text{m}$ using the SetNull function. This range reduces the influence of large dh values and outliers caused by DEM errors rather than from misalignment. A more rigorous handling of outliers is undertaken in the following co-registration method (5.2.2). Each model run outputs a point shapefile with dh , slope, and aspect attributes,

which is limited to valid values using the *Select* tool. From each output shapefile, a random sample of 50 000 points was created using the *Sampling Design Tool*, and the attributes table was exported as a textfile for use in Excel.

An Excel worksheet, created by Christopher Nuth, takes the input of dh, slope and aspect values and uses the Data Solver to find the parameters needed to minimize the residuals of Equation 1, and the corresponding x-, y- and z-shifts. These shifts were then applied using the *Shift Raster* and *Raster Calculator* tools of ArcGIS. The newly shifted rasters could then be input again into the Model Builder tool.

For this co-registration, all rasters were aligned to the reference SRTM DEM at a resolution of 30m pixels. The results were generally not satisfactory, likely because a significant portion of the DEM misalignment was due to tilts and trend surfaces, not horizontal or vertical shifts. This is particularly true for the CORONA DEMs. The lower resolution of the SRTM data is also not ideal. The standard deviation of dh values did not significantly improve for most DEMs following the first iteration. For this reason, the process was only repeated for the Pléiades DEM (Table 9).

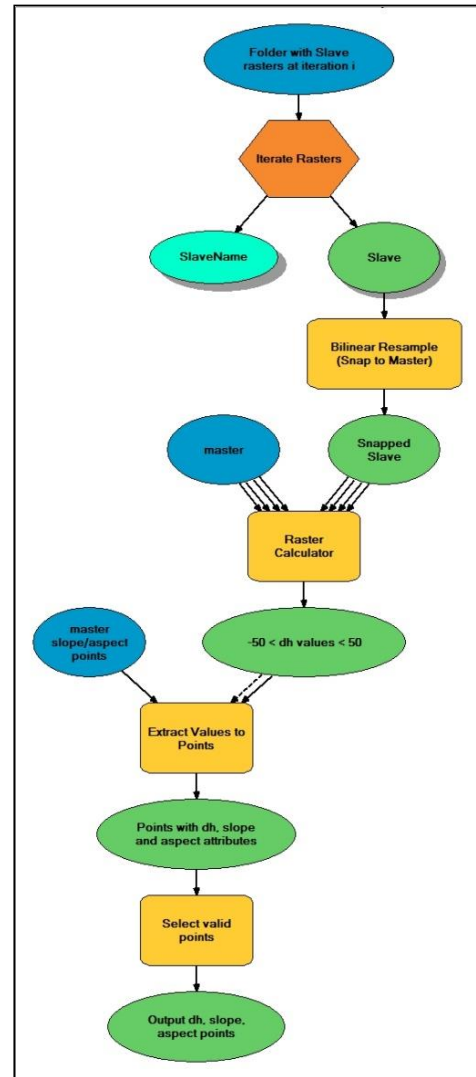


Figure 26: ArcGIS ModelBuilder tool created to iterate co-registration of multiple DEMs.

Table 9: Co-registration of Pléiades DEM to SRTM DEM using ArcGIS/Excel-based method. The elevation difference (dh) RMSE, mean, and standard deviation were calculated from stable terrain pixels with slope between 10° and 45° and a dh value between -50m and 50m (as a rough method for removing outliers).

Iteration	Shift (m)			dh (m)		
	x	y	z	RMSE	Mean	Standard deviation
initial	-	-	-	10.82	2.36	10.57
1	1.11	-2.26	3.01	11.37	-6.47	9.89
2	-0.58	3.39	-7.41	9.14	0.90	9.09
3	0.48	1.07	1.08	9.07	0.02	9.07
cumulative	1.01	2.20	-3.32	-	-	-

The cumulative x-, y- and z- shifts for the Pléiades DEM were 1.01 m, 2.20 m, and -3.32 m, respectively. A small improvement in the RMSE, mean, and standard deviation of dh values was achieved. A comparison of the histograms of elevation differences before and after co-registration (Figure 27) illustrates this change. Of the six DEMs, the co-registered Pléiades DEM showed the best relative accuracy

compared to the SRTM data. The cumulative x-, y-, and z-shifts were applied to the 5m Pléiades DEM which was then used as the reference (master) DEM for the subsequent co-registration of all other DEMs at a finer spatial resolution (5.2.2).

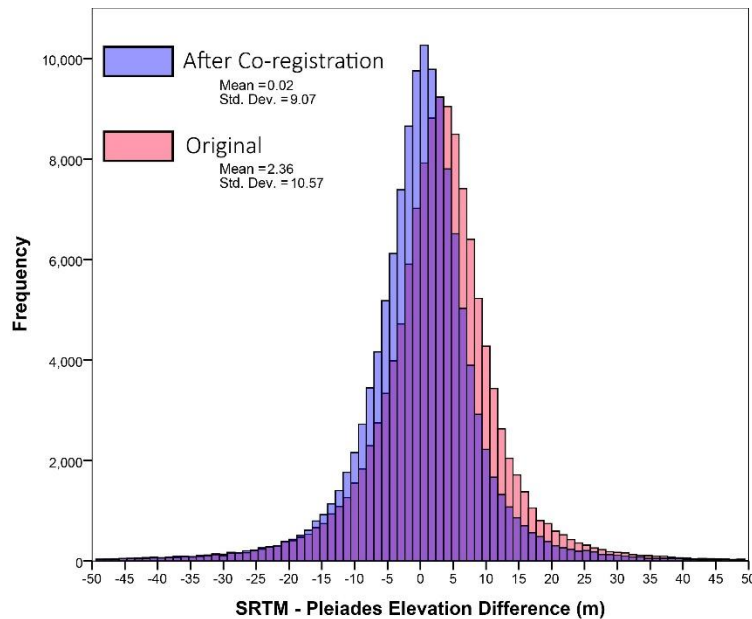


Figure 27: Histograms of the original SRTM-Pléiades elevation differences and the post-co-registration SRTM-Pléiades elevation differences.

5.2.2 DEM co-registration with trend correction

Along with the horizontal and vertical shifts of one DEM raster relative to another, additional error may result from trend surfaces, elevation-dependent bias or sensor-specific bias (Nuth & Kääb, 2011). Tilts and trends were particularly notable for the CORONA imagery, a problem commonly reported by other authors using similar methods (e.g. Pieczonka et al., 2011). If left uncorrected, tilting or bending of the DEMs would lead to significant errors when calculating elevation differences.

A method using Python and R scripts (Pieczonka et al., 2013) was used to perform a more comprehensive co-registration which first removed tilts and trends, and then performed horizontal and vertical shifts based on the same principles of Nuth and Kääb (2011). Using 5m resolution rasters, five slave DEMs (two GeoEye-1 and three CORONA) were co-registered to the master Pléiades DEM. For each slave DEM, the following steps are completed by the Python/R workflow:

- i. Calculate outlier free difference image between master DEM and slave DEM.
- ii. Calculate dh statistics with and without spatial autocorrelation.
- iii. Remove spatial trend from slave DEM.
- iv. Calculate dh statistics with and without spatial autocorrelation.
- v. Perform co-registration based on Nuth and Kääb (2011), until RMS improves by less than 2%. (Cumulative shift values are shown in Table 10.)
- vi. Output trend-corrected and repositioned raster and report.

Table 10: Cumulative raster x-, y-, and z-shifts performed during co-registration based on Nuth and Kääb (2011) to align all CORONA and GeoEye-1 slave DEMs to the reference Pléiades DEM.

Slave DEM	Shift vectors		
	X (m)	Y (m)	Z (m)
Cor 1	1.64	4.73	1.68
Cor 2	1.06	-0.61	3.04
Cor 3	1.91	-0.91	5.88
GE 1	-1.82	0.80	-0.82
GE 2	-0.42	1.13	-0.30

To assess the results of co-registration, the statistics of elevation differences between slave and master DEMs were compared from before and after the corrections (**Table 11**). The values are restricted to areas of stable terrain, with outliers removed. Accounting for trend surfaces resulted in significantly better co-registration results, compared to positional shifts alone. In most cases, trend removal accounted for over 90% of the total change in dh RMS, mean, STDV and median values. Following co-registration, CORONA DEMs showed dh RMS and standard deviation values of ~5.5 m, while the GeoEye-1 RMS and standard deviation are ~1.6 m. Mean dh values became closer to zero for all DEMs, and were within a range of -0.24 - 1.60. Similarly, median dh values approached zero and were within a range of -0.23 - 1.44.

Table 11: Elevation difference (dh) between Pléiades (master) DEM and CORONA/GeoEye-1 (slave) DEMs before and after co-registration steps. Values are from stable terrain areas, with outliers removed and no-autocorrelation.

DEM	Co-registration Step	RMS	Mean	STDV	Med	Min	Max
Cor 1	Original Raster	18.99	14.78	11.92	16.18	-17.18	44.10
	Trend Corrected	6.80	0.67	6.76	0.57	-14.70	16.41
	Trend & Shift Corrected	5.90	0.48	5.88	0.35	-13.10	14.40
Cor 2	Original Raster	9.53	-6.81	6.66	-6.88	-22.00	8.86
	Trend Corrected	5.36	1.27	5.21	1.15	-11.05	13.61
	Trend & Shift Corrected	5.29	1.28	5.13	1.15	-10.75	13.39
Cor 3	Original Raster	9.73	4.69	8.52	4.06	-14.81	23.75
	Trend Corrected	5.36	1.64	5.10	1.51	-9.86	13.01
	Trend & Shift Corrected	5.11	1.60	4.85	1.44	-9.31	12.45
GE 1	Original Raster	4.59	0.58	4.55	0.68	-9.80	11.50
	Trend Corrected	1.90	-0.35	1.87	-0.32	-4.73	4.16
	Trend & Shift Corrected	1.63	-0.24	1.61	-0.23	-4.06	3.64
GE 2	Original Raster	5.49	-4.86	2.56	-4.92	-10.69	0.97
	Trend Corrected	1.73	-0.25	1.71	-0.22	-4.32	3.75
	Trend & Shift Corrected	1.62	-0.18	1.61	-0.19	-4.05	3.55

Figure 28 illustrates results of the co-registration for one slave DEM (Cor 3). The tilt can easily be visualized by subtracting the co-registered DEM from the original DEM (A). This tilt caused higher values on the western side of the Cor 3 DEM and lower values on the eastern side and was the dominant source of

error. Some terrain features are also visible in the before/after difference raster, indicating a horizontal shift as well, which was also corrected by co-registration. The impact of these errors can also be seen when the Pléiades DEM is subtracted from both the pre- and post- co-registration DEMs to create DoDs (C and D, respectively). Using the same colour ramp to depict elevation difference over stable terrain makes it clear that the tilt has been corrected. Remaining errors are mostly small pockets in areas of poor matching and/or steep slopes. The comparison of the histograms of elevation differences (B) shows that the distribution is closer to normal, with a mean value closer to 0 following co-registration.

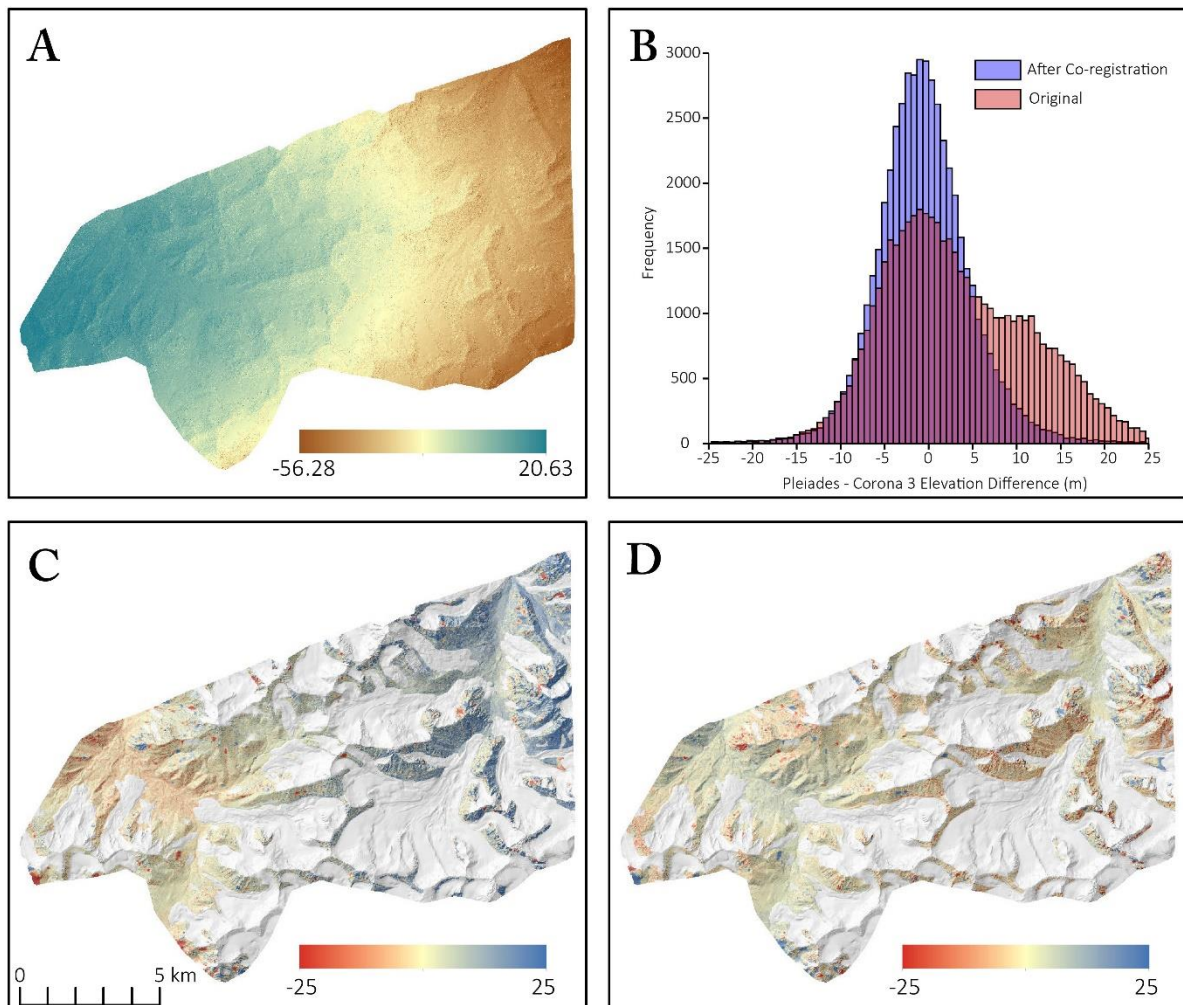


Figure 28: Co-registration results for an example slave DEM (Cor 3). In the upper left (A), the elevation difference between the original Cor 3 DEM and the co-registered Cor 3 DEM. In the upper right (B) the histograms of elevation differences between the Cor 3 DEM and the Pléiades master DEM before and after co-registration. On the lower row, the elevation difference rasters of Pléiades and Cor 3 before (C) and after (D) co-registration.

Following co-registration, the individual GeoEye-1 and the CORONA DEM rasters were mosaicked to create a single GeoEye-1 DEM and a single CORONA DEM.

5.3 Surface elevation change

Co-registered DEMs were subtracted (older from newer) to create three elevation difference images. The DEM errors are notable in these elevation difference rasters, where outlier dh values are in the range of ± 800 m. These errors arise from mismatched pixels, areas of shadow, low image contrast, clouds, and low accuracy in steep slopes. As a first step, the dh values were limited to a range of ± 100 m for multi-decadal change (1971-2012 and 1971-2016) and ± 25 m for short-term change (2012-2016) as these were considered likely valid values. These ranges encompassed >98% of the original pixels for all DoDs, thus removing only outliers in the data.

There are numerous strategies in the literature regarding outlier handling and uncertainty analysis for surface elevation calculations. In this study, two different measures of the uncertainty were calculated based on the elevation difference values over stable terrain (5.3.1). Outliers were handled separately for stable terrain, glacier-covered areas and rock glaciers (5.3.2).

5.3.1 Uncertainty assessment

Two separate uncertainty estimators were tested. The first is based on Bolch et al. (2011) using the standard error (SE) and mean elevation difference (MED) over stable terrain. The elevation difference rasters were clipped to stable terrain areas and the standard error was calculated with a decorrelation length of 400 m (Equation 2).

$$SE = \frac{STDV_{stable\ terrain}}{\sqrt{n}} \quad (2)$$

Where: n = the number of included pixels

The uncertainty is estimated using the SE and MED, according to the law of error propagation (Equation 3).

$$e = \sqrt{SE^2 + MED^2} \quad (3)$$

The resulting uncertainties (Table 12) are all below 1m, significantly lower than uncertainties reported in other similar studies. To avoid underestimating the uncertainty, a second uncertainty analysis was undertaken.

Table 12: Statistics of elevation differences over stable terrain.

DoD	MED (m)	STDV (m)	SE (m)	n	Uncertainty (m)
CORONA - GeoEye-1 (1971 – 2012)	0.051	13.472	0.797	286	0.799
CORONA – Pléiades (1971 – 2016)	0.240	12.431	0.648	286	0.735
GeoEye-1 – Pléiades (2012-2016)	-0.120	5.298	0.319	276	0.341

The second uncertainty is based on, among others, Pieczonka et al. (2013), Pieczonka & Bolch (2015), and Pellicciotti et al. (2015). From the stable terrain difference raster, outliers were removed using the 1.5-fold inter-quartile range (IQR). From this raster, the following statistics were calculated: mean, standard deviation, median, median of absolute values, normalized median absolute deviation (NMAD), and the 68.3% quantile of absolute dh values. The NMAD (Equation 4) is a robust statistical estimator which is the preferred option to the standard deviation if many outliers are present (Höhle & Höhle, 2009). In the case of normality, this will be equivalent to the standard deviation (Höhle & Höhle, 2009).

$$\text{NMAD} = 1.4826 \cdot \text{median}_j(|dh_j - m_{dh}|) \quad (4)$$

Where: dh = individual elevation difference (error) at $j = 1, \dots, n$
 m_{dh} = median of the errors

In the case of non-normality, the 68.3% quantile of absolute dh values can also be used to estimate uncertainty (Pellicciotti et al., 2015; Pieczonka et al., 2013). The 68.3% quantile indicates the limit in which 68.3% of the absolute elevation differences are situated.

Table 13: Statistics of stable terrain dh values.

DoD	1.5 IQR range (m)	Mean (m)	STDV (m)	Median (m)	Median dh (m)	NMAD (m)	68.3% quantile dh (m)	95% quantile dh (m)
CORONA - GeoEye-1 1971 - 2012	-20.388 20.393	0.011	7.047	-0.237	4.16	6.117	6.71	13.036
CORONA – Pléiades 1971 - 2016	-19.211 18.434	-0.140	6.603	-0.314	3.993	5.933	6.299	11.643
GeoEye-1 – Pléiades 2012-2016	-6.373 6.1755	-0.073	2.199	-0.074	1.199	1.794	2.024	4.010

For each DoD, the standard deviation, NMAD and 68.3% quantile values were similar. Determining the best estimate of uncertainty depends on the distribution of the dh values: NMAD can be used with a normal distribution and the 68.3% quantile should be used with non-normal distribution (Pieczonka et al., 2013). Whether or not the distributions are normal could be tested statistically or with QQ-plots. As the difference in uncertainty would be quite small, the 68.3% quantile was chosen over the NMAD as the more conservative estimate, and was used for all DoDs.

5.3.2 Outlier handling

There are a wide variety of methods in the literature for handling outliers and no strategy can be definitely identified as the best practice. In this study, outliers were assessed separately for glacier areas and non-glacier areas. A simple threshold based on the standard deviation was used to remove outliers in the glacier areas. A threshold of 2σ created large data gaps and therefore a value of 3σ was selected instead. Using this threshold, the glacier data gaps were small and were not filled.

More robust outlier handling would likely improve results, especially for glacier mass balance calculations. Some examples in the literature include correcting for or removing values in areas of steep slopes (e.g. Pieczonka et al., 2013), calculating outliers with respect to elevation (e.g. Pieczonka & Bolch, 2015), or calculating outliers for individual features based on the standard deviation of absolute dh values (Pellicciotti et al., 2015).

Table 14: Glacier and rock glacier surface elevation change.

DoD	Terrain	Min, Max (m) (outliers removed)	Mean (m)	STDV (m)
CORONA - GeoEye-1 1971 - 2012	Stable	-20.388, 20.393	0.011	7.047
	Glaciers	-76.010, 41.614	-16.452	18.452
	Rock glaciers	-22.923, 18.697	-1.645	5.503
CORONA – Pléiades 1971 - 2016	Stable	-19.211, 18.434	-0.140	6.603
	Glaciers	-79.743, 42.147	-18.467	19.473
	Rock glaciers	-22.607, 18.731	-1.508	5.547
GeoEye-1 – Pléiades 2012-2016	Stable	-6.373, 6.1755	-0.073	2.199
	Glaciers	-16.274, 10.720	-2.932	3.774
	Rock glaciers	-6.231, 6.841	0.238	1.526

5.4 Orthoimage generation

Pléiades and GeoEye-1 orthoimages were generated in ERDAS IMAGINE using the most nadir image of each pair, at a resolution of 0.5 m. Multi-spectral imagery was pan-sharpened to 0.5 m using the panchromatic imagery. CORONA orthoimages were generated in RSG at a resolution of 5.0 m using the co-registered DEMs. All orthoimages showed a good alignment with each other in most areas. Offsets are greatest in areas of steep slopes or where clouds, shadows or low contrast caused error in the DEMs.

5.5 Glacier change measurements

5.5.1 Glacier delineation

Glaciers were manually delineated for CORONA, GeoEye-1 and Pléiades orthoimages (**Figure 29**). Only glaciers fully within an image were included (i.e. no partial glaciers and no glaciers with partial cloud cover). Delineation was more difficult in areas where glacier termini were debris-covered or where glacier boundaries were obscured by snow, shadow or cloud. Additional imagery (Landsat, Google Earth), topography layers (slope rasters and hillshades), and the elevation difference rasters were used where possible to improve delineations, especially for debris-covered areas.

Numeric glacier IDs were assigned to the individual CORONA polygons and were then given to the corresponding Pléiades and GeoEye-1 outlines (including multipart polygons from glaciers which became dissected). This allowed for area and mass changes to be calculated easily for individual glaciers..

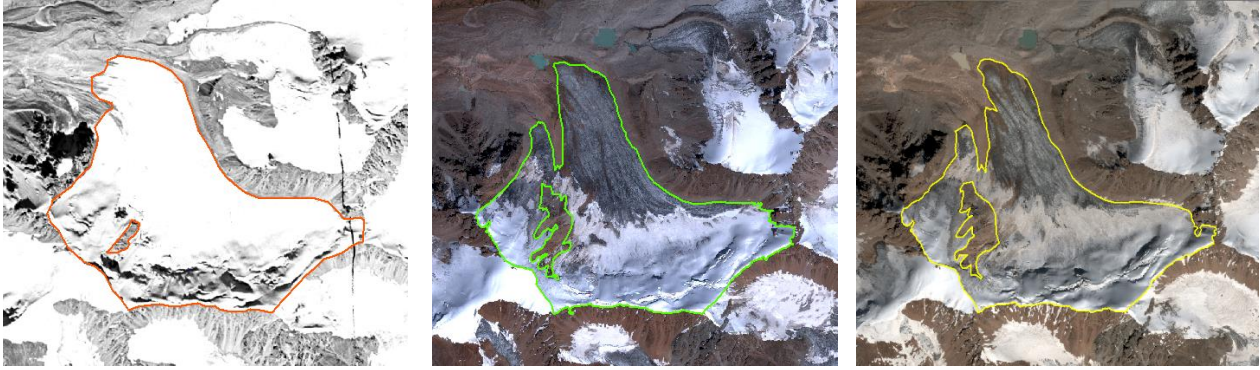


Figure 29: Glacier delineation CORONA 1971 (left), GeoEye-1 2012 (centre), and Pléiades 2016 (right).

The buffer method (Granshaw & Fountain, 2006; Bolch et al., 2010) was used to estimate the uncertainty of glacier delineation and glacier area. A buffer of $\pm 10\text{m}$ was applied to the CORONA outlines and a buffer of $\pm 2\text{m}$ was applied to Pléiades and GeoEye-1 outlines. Many studies used a half-pixel or one-pixel size buffer to estimate uncertainty of medium resolution imagery such as Landsat, when delineating glaciers (e.g. Bolch, 2015). However, with a pixel size of 0.5 m it seems unrealistic to assume the error would be so low, as the ice boundary is not always easily identifiable. Therefore, a higher value was chosen which seemed more appropriate for the actual uncertainty of locating the glacier boundaries in the high resolution imagery. For CORONA imagery, this buffer resulted in a $\pm 4.9\%$ change in total area and for the high resolution imagery, the buffer resulted in a $\pm 1.6\%$ total area change. With this method, the relative uncertainty is greater for small glaciers than large glaciers. These uncertainties do not take into account the uncertainty of the orthoimages themselves, although the overall alignment of all images suggests this error is low. To account for uncertainties due to terminus debris cover, seasonal snow, shadows and image distortions in steep slopes, an additional 2% uncertainty is included in area measurements.

5.5.2 Glacier area change

Using the manually delineated glacier polygons, the total glacier area change was calculated for the full area encompassed by all three imagery sets for three time steps (1971-2012, 1971-2016, 2012-2016). Only glaciers fully within the imagery were included. Uncertainty was calculated using standard uncertainty propagation (Equation 5):

$$\delta a = \sqrt{\sum_{i=1}^n \delta a_i^2} \quad (5)$$

Where:

δa = overall area uncertainty

δa_i = area uncertainty component at specific time step.

Area change for individual glaciers was calculated using the glacier IDs assigned during delineation. The buffer-based uncertainty is significantly greater for smaller glaciers compared to larger glaciers. Some small glaciers visible in the 1971 imagery had completely disappeared in the later imagery.

5.5.3 Glacier volume and mass change

Glacier volume and mass change were calculated for the entire study area as well as for individual glaciers for each DoD. The dh rasters were clipped to the glacier polygons of the delineation of the earlier DEM. Total volume change was calculated by multiplying the average dh value by the number of pixels and the area of a pixel (25m²). To determine the change in mass, a density of 850±60 kg/m³ was adopted (Huss, 2013). This density was multiplied by the average dh value to determine the mass change per unit area in metres water equivalent (m w.e.). The specific mass balance was then calculated by dividing the average mass change per unit area by the number of years between DEMs. The *zonal statistics* tool in ArcGIS was used to calculate values for each individual glacier. Uncertainties were calculated using standard error propagation for multiplication (Equation 6).

$$\frac{\delta m}{m} = \sqrt{\left(\frac{\delta dh}{dh}\right)^2 + \left(\frac{\delta \rho}{\rho}\right)^2} = \sqrt{\left(\frac{Q68.3\%}{dh}\right)^2 + \left(\frac{60}{850}\right)^2} \quad (6)$$

Where: δ refers to the uncertainty of the given value
 m = mass
 dh = average elevation change of glacier area
 ρ = density
 Q68.3% = 68.3% quantile of absolute dh values (see section 5.3.1)

5.6 Rock glacier change measurements

5.6.1 Rock glacier delineation

Rock glacier identification and delineation was done manually for all areas within the extents of the Pléiades and GeoEye-1 orthoimages. Outlines of rock glaciers only partially covered by the high resolution imagery were extended where possible using CORONA or Landsat imagery. Strategies from Schmid et al. (2014) and Kinworthy (2016) were used as guidelines for rock glacier identification. In cases where rock glacier delineation was unclear, a combination of additional sources was useful, including topographic layers from the high resolution DEMs (hillshade, slope raster) as well as Google Earth imagery (Figure 30). The quality of Google imagery varies over the study area, but at least in some locations was useful, particularly for the easily navigable 3D viewing. The InSAR-derived polygons (Strozzi et al., 2017) helped to identify possible rock glacier locations, although not all polygons were confirmed as rock glaciers from the optical imagery.

In general, mapping the toe end of rock glaciers is easier than defining the upper bounds. Steep slopes along the front and sides are often identifiable in the optical imagery or in the topography. However, at the head of the rock glacier there is often no clear boundary. A single rock glacier delineated by two different workers may show a very large difference, even with a well defined strategy, as the process is to

some degree subjective (Schmid et al., 2014). For this reason, no accuracy assessment of rock glacier area measurements was considered.

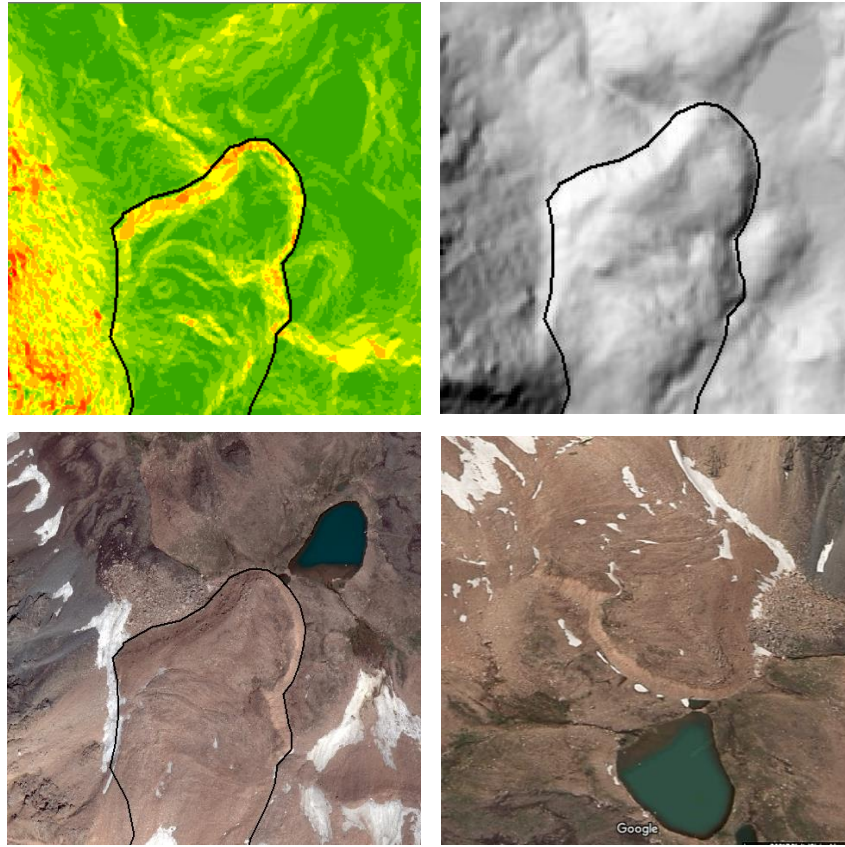


Figure 30: Example of rock glacier delineation. Upper images show a slope raster (left) and hillshade (right), which were useful for feature identification/confirmation. In the lower row, the same rock glacier is identifiable in the Pléiades imagery (left) and can be easily viewed from a different angle in Google Earth imagery (right).

5.6.2 Horizontal surface displacements of rock glaciers

Horizontal surface displacement was measured using the correlation algorithms COSI-Corr (Leprince et al., 2007), an extension to ENVI Classic software (Harris Geospatial Solutions). The 2012 and 2016 0.5 m orthoimages were first combined in an ‘exclusive’ image stack (including only the overlapping areas) in ENVI. The frequency correlator of COSI-Corr operates in two steps. First, it roughly estimates displacement between two patches using the initial sliding window size, input by the user (Ayoub et al., 2009). A second correlation with the final sliding window size is then used to determine subpixel displacement (Ayoub et al., 2009). The displacement is determined in the frequency domain by calculating the phase difference of the Fourier Transform (Ayoub et al., 2009). Multiple combinations of window sizes, step size and other options were tested to determine the most successful settings. The initial and final window sizes had the greatest impact on the output: too large of a window and the level of detail is reduced; too small of a window and the results become too noisy (Figure 31). The most successful parameters were a 64-pixel initial window and a 32-pixel final window.

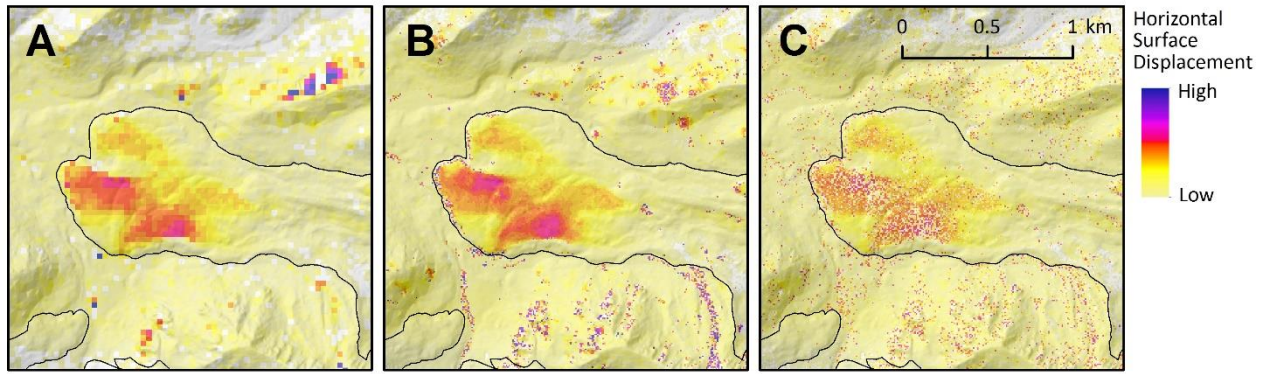


Figure 31: COSI-Corr displacement results at Gorodetsky rock glacier using different initial/final window size settings in the frequency correlator tool. Window sizes (initial, final) are: A 128, 64; B 64, 32; and C 32, 16.

The correlation tool outputs a raster file with three bands: east/west displacement (positive toward the east), north/south displacement (positive toward the north) and signal-to-noise ratio (SNR) which gives an indication of the quality. The SNR band consists of values between 0 and 1, with values closer to 1 indicating a better signal-to-noise ratio. The east/west and north/south bands were converted to horizontal displacement using the band math function and Pythagorean Theorem (Equation 7).

$$d = \sqrt{EW^2 + NS^2} \quad (7)$$

Where: d = displacement
 EW= east/west displacement (band 1)
 NS= north/south displacement (band 2)

The resulting rasters were filtered based on the SNR band to remove values with the lowest quality. Glacier areas were removed because the results in these areas showed only noise (which is expected based on the time interval and the relatively rapid rate of glacier movement). Remaining noise was further reduced by calculating the neighborhood (3 x 3) standard deviation for each pixel using the *focal statistics* tool of ArcGIS. Pixels with a neighborhood standard deviation greater than a certain threshold (decided by visual assessment) were removed.

The COSI-Corr workflow was also performed using the CORONA imagery. Necsoiu et al. (2016) successfully applied COSI-Corr image matching to track rock glacier movement, using precisely orthorectified and co-registered small tiles of CORONA images. The displacement rates of the rock glaciers investigated by Necsoiu et al. (2016) were very small (0.8-2.2 cm/year) compared to some of the highly active rock glaciers in the current study area. In theory, the larger displacements (which are significantly greater than the image resolution), would improve tracking results. However, the high activity of Tien Shan rock glaciers also increases the chances that features are not preserved over time and therefore will not be correctly matched during correlation.

For comparison to the CORONA imagery, the Pléiades and GeoEye-1 imagery was resampled to 5 m pixels. The correlation results between CORONA and GeoEye-1 were less successful than the correlation between CORONA and Pléiades, which shows a discernable pattern at some of the large rock glaciers (**Figure 32**). From these, four glaciers were selected for further investigation: Archaly, Morenny, Gorodetsky, and Ordzhonikidze. Absolute displacements were converted to average annual displacement by dividing by the number of decimal years between images (44.94 years and 4.05 years) to allow for rate comparisons.

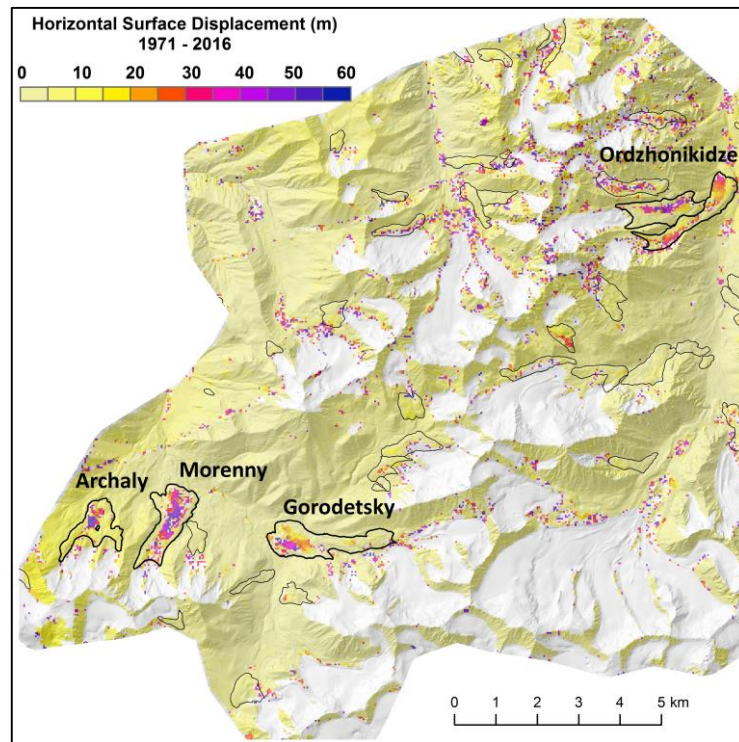


Figure 32: Horizontal Surface Displacement from 1971 – 2016 with glacier areas removed. Results of highlighted rock glaciers are discussed in Chapter 6. See Figure A5 in the appendix for the full data.

Uncertainty of the horizontal displacement values was calculated following Avouac et al. (2014), based on the East/West and North/South measurements in areas of stable terrain. Outliers were removed using the 1.5 fold IQR. The calculated mean and standard deviation values (**Table 15**) are higher than the uncertainties of Avouac et al. (2014), but this is attributed to the time span between images, as that study used images taken only 16 days apart. Slow movement, such as creep, is likely to create larger displacements, even in stable terrain. The uncertainty also speaks to potential misalignment of the images.

Table 15: East/west and north/south displacement statistics in stable terrain.

Image Pair	Time between images (years)	Measure	Min, Max (m) (outliers removed)	Mean (m)	STDV (m)
GeoEye-1 & Pléiades 1971 – 2016	4.05	North/South Displacement	-2.07, 2.20	-0.05	0.69
		East/West Displacement	-3.33, 2.53	-0.41	0.98
Corona & Pléiades 2012 - 2016	44.94	North/South Displacement	-17.502, 13.09	-1.97	5.08
		East/West Displacement	-10.72, 9.86	-1.36	3.15

6 RESULTS AND DISCUSSION

6.1 Glaciers

6.1.1 Glacier area change

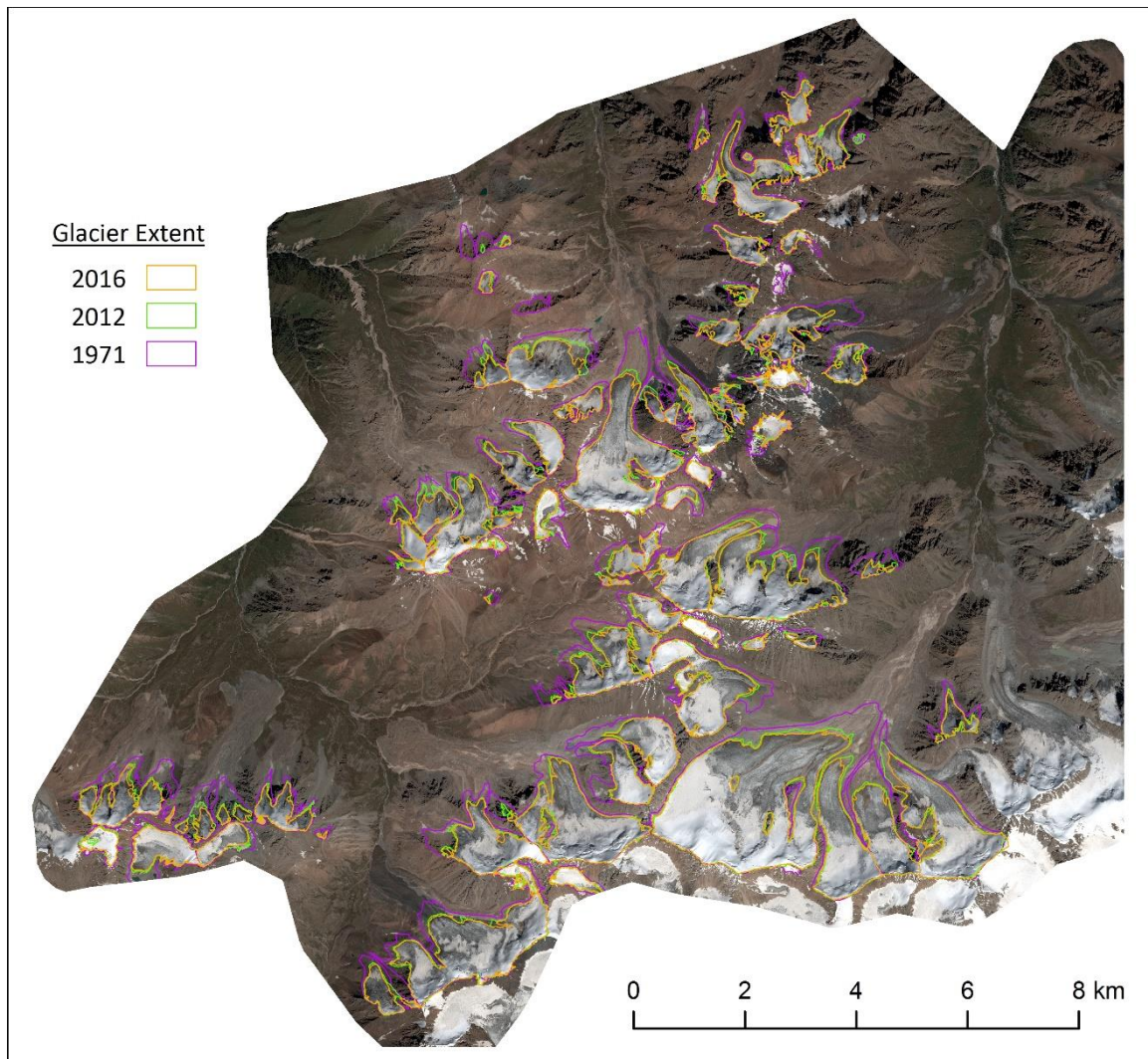


Figure 33: Glacier delineations from 1971 (CORONA), 2012 (GeoEye-1), and Pléiades (2016). Background image is pan-sharpened Pléiades true-colour composite.

Total glacier area over the full 45-year time period of investigation (1971 – 2016) decreased from $55.45 \pm 3.83 \text{ km}^2$ to $39.19 \pm 1.41 \text{ km}^2$, a relative loss of $29.32 \pm 7.36 \%$ (Table 16). This is equivalent to an average annual area change of $-0.65 \pm 0.16 \%$ per year. Bolch (2007) reported a relative annual area change of $\sim -0.8 \%$ per year for the same region for the time period 1955-1999 (Bolch, 2007). However, these values also contained uncertainties related to a Soviet glacier inventory, which may have caused them to be too high (Bolch, 2007). Severskiy et al. (2016) reported an annual area loss of -0.76% per year (1955/56-2008) for the Ile Alatau range, which encompasses the study area. From 2012-2016, the annual relative loss was much greater ($-1.42 \pm 1.24 \%$ per year). Glacier area losses are highly variable throughout the Tien Shan

(Narama et al., 2010; Kutuzov & Shahgedanova, 2009) and lower values of annual area change have been reported for most regions of Central, Inner and Eastern Tien Shan, where results range from about 0.05 % to about 0.40 % area loss per year (e.g. Pieczonka & Bolch, 2015; Narama et al., 2010; Aizen et al., 2007; Li et al., 2006). In general, the outer ranges, including the region of the study area, have faster shrinkage rates than inner ranges (Sorg et al., 2012). The rapid shrinking of glaciers in this study area cannot be assumed to be representative of the larger region.

Table 16: Glacier area change 1971 – 2016.

Measure	1971	2012	2016
Glacier area (km ²)	55.45 ± 3.83	41.54 ± 1.50	39.19 ± 1.41

Measure	1971-2012	2012-2016	1971-2016
Absolute area change (km ²)	-13.91 ± 4.11	-2.35 ± 2.06	-16.26 ± 4.08
Relative area change (%)	-25.09 ± 7.41	-5.66 ± 4.96	-29.32 ± 7.36
Relative area change / year (%)	-0.61 ± 0.18	-1.42 ± 1.24	0.65 ± 0.16

The relationship between glacier area and the relative area change (1971 – 2016) can be seen in **Figure 34**. The pattern is similar to that reported by Narama et al., (2010) for the Pskem and Ili-Kungöy regions. Small glaciers contribute disproportionately to overall glacier shrinkage, and regions with many small glaciers (< 1 km²) show a faster rate of glacier area change (Narama et al., 2010). This may account for the large relative decrease of glacier area in these valleys, where 52 of the 69 CORONA-delineated glaciers (75%) were less than (< 1 km²). These small glaciers make up ~28 % of the total area in 1971, and account for ~38 % of the total area loss between 1971 and 2016.

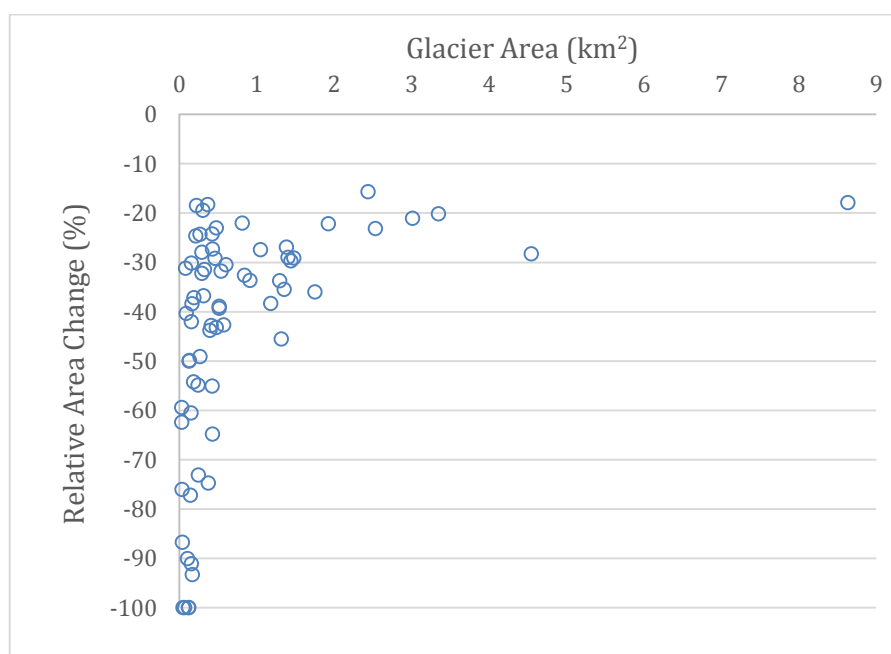


Figure 34: Relationship between glacier area and relative glacier-area change (%) from 1971 – 2016.

6.1.2 Glacier volume and mass change

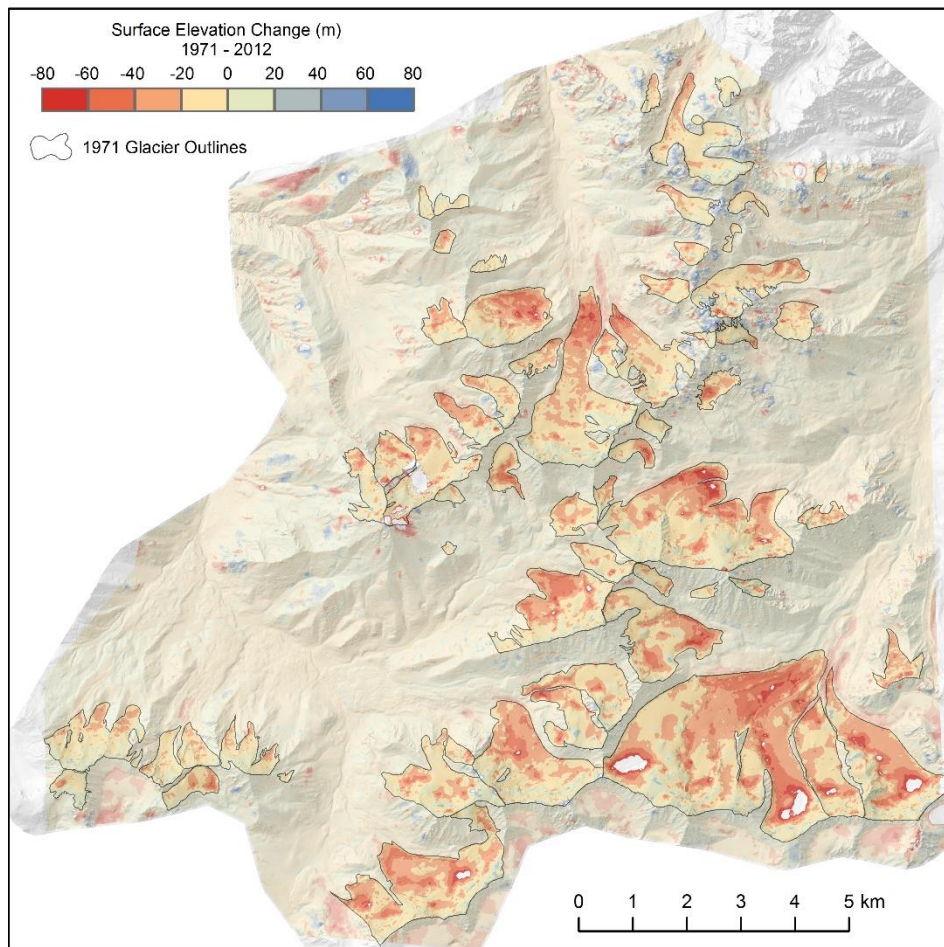


Figure 35: Difference between 1971 CORONA DEM and 2012 GeoEye-1 DEM, with glacier areas highlighted. See Figure A1 in the Appendix for the full data.

Between 1971 and 2016, the investigated glaciers in the study area lost a total of $0.96 \pm 0.33 \text{ km}^3$ of ice (Table 17). For the period of 1971-2012, the annual mass balance was $-0.34 \pm 0.14 \text{ m w.e. a}^{-1}$ (Figure 35). This fits very well with estimates reported by Fairinotti et al. (2015) for the Ile Alatau and Kungöj Ala-Too region for the time period of 1961-2012. Based on satellite gravimetry, laser altimetry and glaciological modelling, Fairinotti et al. (2015) found a specific mass change rate of $-0.31 \pm 0.16 \times 10^3 \text{ kg m}^{-2} \text{ a}^{-1}$ (units comparable to m w.e. a^{-1}).

The mass balance value found in this study is also within the range of reported mass balance estimates for the Tien Shan region as a whole, for example $-0.38 \text{ m w.e. a}^{-1}$ reported by Dyurgerov (2010). And it fits well with the global average based on glaciological records between 1976-2005 (Zemp et al., 2009) which was estimated at $-0.33 \text{ m w.e. a}^{-1}$. However, for this region specifically, the results of the long term mass balance may still be too low, based on comparisons to the in situ measurements (discussed below). The outer ranges of the Tien Shan have been losing mass at a faster rate than the inner ranges (Sorg et al., 2012), and therefore a comparison to the entire region or to other parts of the Tien Shan do not necessarily validate these results.

Table 17: Glacier volume and mass changes.

Measure	1971-2012	1971-2016	2012-2016
Average elevation change (m)	-16.45 ± 6.71	-18.47 ± 6.30	-2.93 ± 2.02
Volume Change (km ³)	-0.85 ± 0.35	-0.96 ± 0.33	-0.11 ± 0.08
Mass Change (m w.e.)	-13.98 ± 5.79	-15.70 ± 5.47	-2.49 ± 1.73
Average Annual Mass Balance (m w.e. a ⁻¹)	-0.34 ± 0.14	-0.35 ± 0.12	-0.62 ± 0.43

For the period of 1912-2016, the annual mass balance was -0.62 ± 0.43 m w.e. a⁻¹ (Figure 36), about 1.8 times the average of the prior four decades.

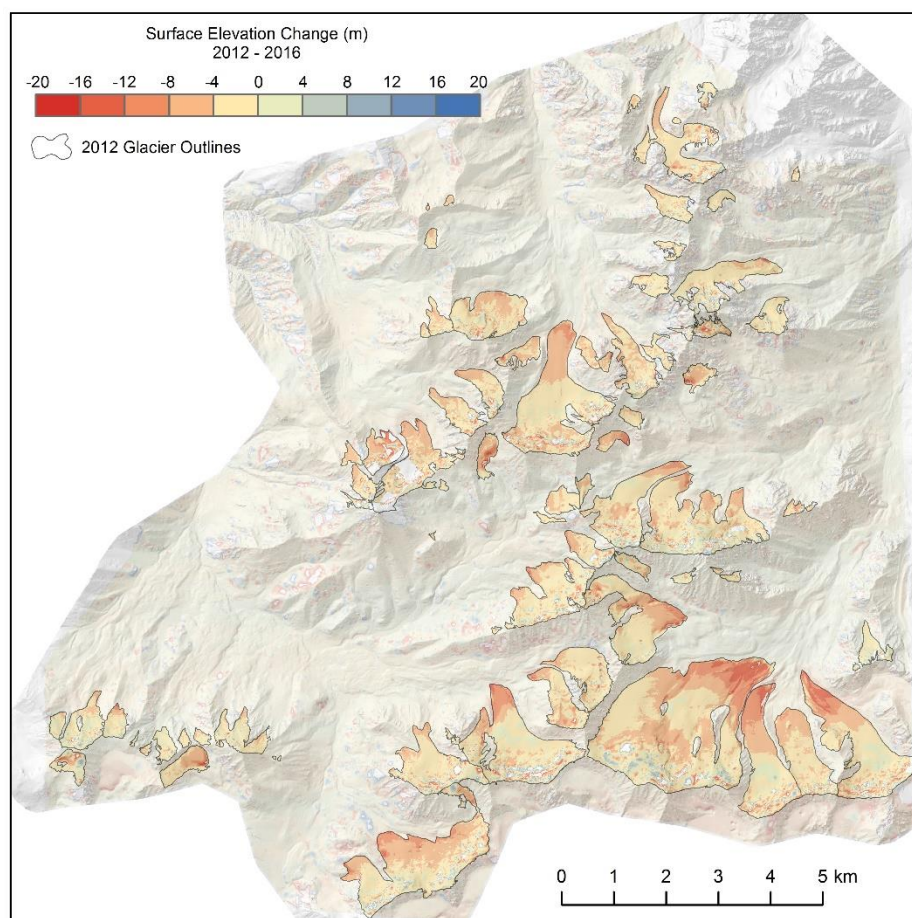


Figure 36: Difference between 2012 GeoEye-1 DEM and 2016 Pléiades DEM, with glacier areas highlighted. See Figure A3 in the Appendix for the full data.

The long term glaciological record of mass balance at Tuyuksu glacier is useful for comparison. The in situ measurements are carried out by researchers at the Institute of Geography, National Academy of Science of the Kazakh Republic, and the data is available through the WGMS. The Tuyuksu mass balance estimates from this study (Figure 37) are significantly lower than the WGMS record (Table 18) for both the 1971-2012 estimate and the 1971-2016 estimate. The geodetic results underestimate the glaciological results by about 35%. For the modern imagery, the geodetic results overestimate the glaciological measurements by about 37%, but the WGMS results are within the uncertainty of this study.

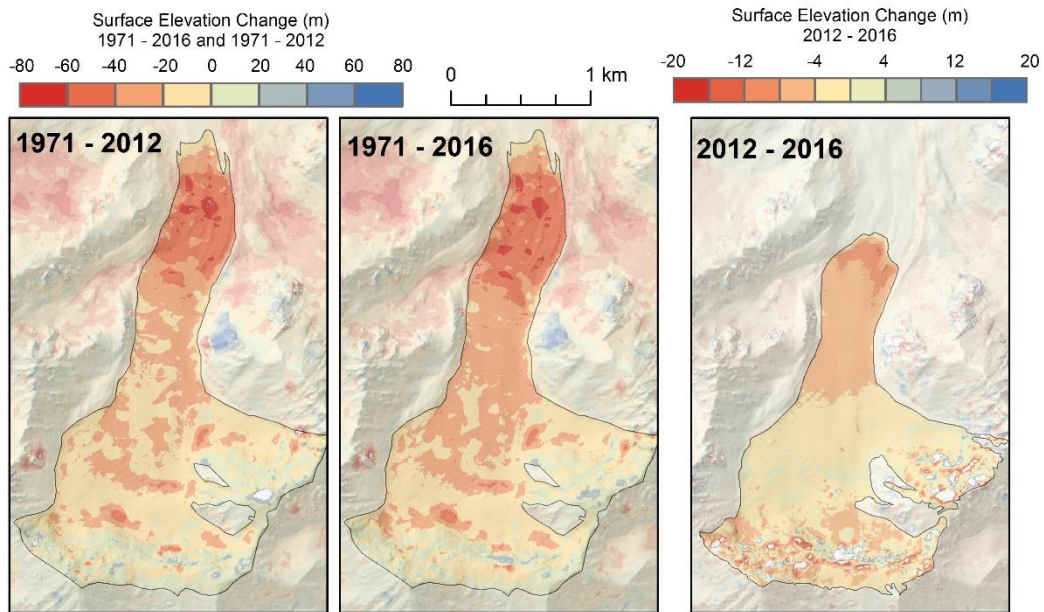


Figure 37: Surface elevation change at Tuyuksu Glacier. Note the different colour scales for the long term change (1971-2012 and 1971-2016; left and center) and the recent change (2012-2016; right).

The suspected reason for the discrepancies is a combination of factors leading to poor quality in the accumulation zone, where DoDs appear splotchy and the results may be unreliable. The first problem is low image contrast, especially in the CORONA imagery. Data gaps were interpolated during DEM generation in RSG, which may have led to false values. This problem is exacerbated by the lower accuracy in steep slopes of all DEMs. Steep slopes comprise large areas of the accumulation zone not only at Tuyuksu Glacier, but for many of the study area glaciers. Over decadal time scales, surface lowering high in the accumulation zone may be very low compared to areas in the ablation zone, even during glacier retreat (Maurer et al., 2016). However, it is unlikely that surface elevation gain would occur when mass balance is consistently negative. Positive elevation change observed in the accumulation zone of Tuyuksu Glacier and elsewhere in the study area between the 1971 and the 2012/2016 data, are therefore indicative of DEM error. DEMs created from optical imagery often are inaccurate in the accumulation zone (Racoviteanu et al., 2009). It is possible that better handling of outliers within specific elevation bands could correct this problem. Alternatively, simply removing values in very steep slopes could also improve accuracy.

For the modern imagery, again, the steep slopes of the accumulation area are a likely cause of errors in the DEMs, which are seen in the patchy and highly variable elevation differences of the upper part of the glacier. The overestimation of mass balance in recent years could also be related to the location of in situ measurements, which are biased towards the lower reaches of the glacier. The high, steep slopes of glaciers are generally under-sampled or not measured at all due to accessibility.

Table 18: Tuyuksu Glacier (Tsentralniy Tuyuksuyskiy) geodetic annual mass balance with comparison to WGMS glaciological record.

Year range	Geodetic Mass balance (m w.e. a ⁻¹)	WGMS Glaciological Mass Balance (m w.e. a ⁻¹)	Relative Difference (%)
1971-2012	-0.33 ± 0.14	-0.51	-35%
1971-2016	-0.32 ± 0.12	-0.50	-36%
2012-2016	-0.65 ± 0.43	-0.41	+37%

It is also worth noting that Hagg (2004) found a similar 33% difference between the geodetic method and the glaciological method for Tuyuksu glacier for the time period 1958-1998. Over those 40 years, Hagg (2004) calculated an annual mass balance of -0.32 m w.e. a⁻¹.

6.2 Rock glaciers

6.2.1 Rock glacier inventory

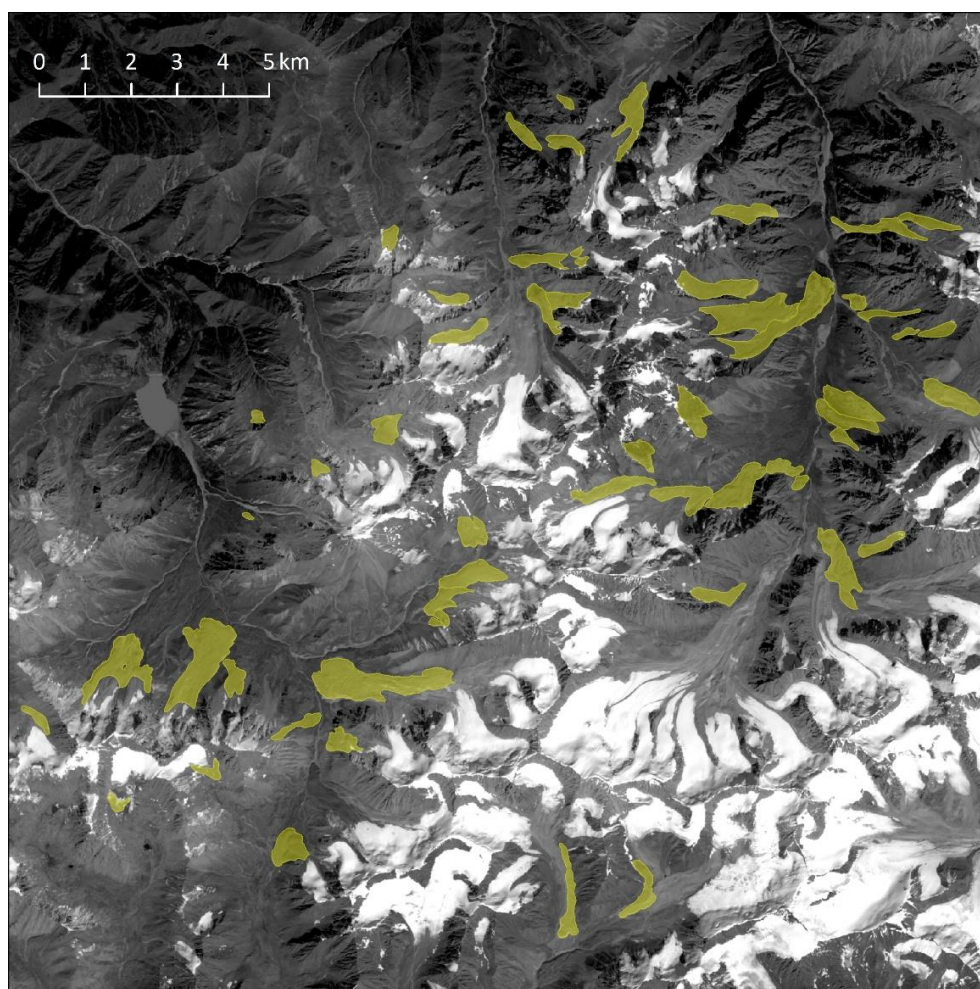


Figure 38: Rock glaciers identified in the high resolution imagery. Landsat 8 panchromatic background image.

A total of 57 rock glaciers (Figure 38) were identified in the study area, ranging in size from 0.02 km² to 1.59 km². The total rock glacier area delineated is 19.34 km². 16 rock glaciers are located in the

Ulken Almaty valley, 12 in the Kishi Almaty valley, 24 in the Left Talgar valley and 5 on the south side of the study area in Kyrgyzstan. Moraine-type rock glaciers are more common (41) than talus-type rock glaciers (16). Activity level based on visual image interpretation alone led to a classification of 50 active, 2 slightly active and 5 inactive rock glaciers. This differentiation was based on the presence or absence of bright, steep frontal slopes, ridges and furrows, and vegetation. Rock glaciers in the study area range in elevation from 2711 m a.s.l to 3879 m a.s.l., with an average elevation of 3405 m a.s.l. Examples of delineated rock glacier features are shown in Figure 39.

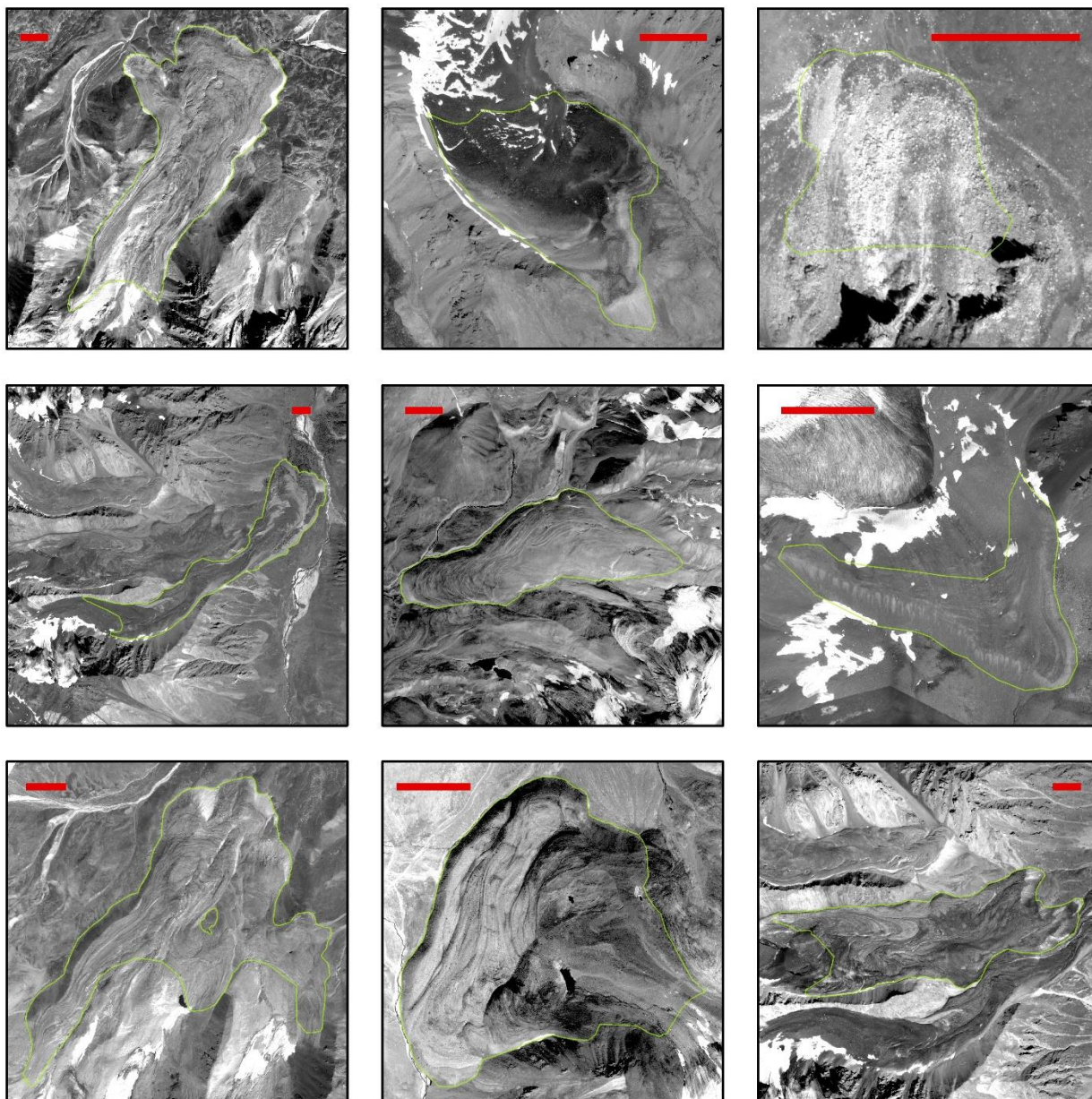


Figure 39: Rock glacier inventory examples. Red line indicates 200 m in each square.

The number of identified features in a rock glacier inventory inevitably depends on the definition of features and the classification of, or inclusion/exclusion of, features which are uncertain. Several features

which were indistinguishable as being rock glaciers or other processes (landslides, rockfall, solifluction, moraines) were excluded. Comparing these results to previous inventories, the number of delineated features is similar, but not identical, to that of Gorbunov et al. (1998). In the Ulken Almaty valley, Gorbunov et al. (1998) identified 16 rock glaciers (12 moraine- and 4 talus-type) while in this inventory 15 rock glaciers were identified (11 moraine- and 4-talus). In the Kishi Almaty valley, on the other hand, this study identified one more rock glacier than the Gorbunov et al. (1998) inventory. These small differences are likely a result of classification differences, or adjacent features being counted as a single rock glacier or multiple rock glaciers. Compared to the rock glaciers investigated by Bolch & Gorbunov (2014) using medium-resolution imagery, the higher resolution Pléiades and GeoEye-1 imagery allowed for mapping of significantly more features. Within the same area, only 25 rock glaciers were included when identification was based on 15m Landsat ETM+ imagery (Bolch & Gorbunov, 2014). The shape of mapped features also varies between the two delineations as features could be more accurately mapped with the higher resolution imagery.

6.2.2 Rock glacier surface elevation change

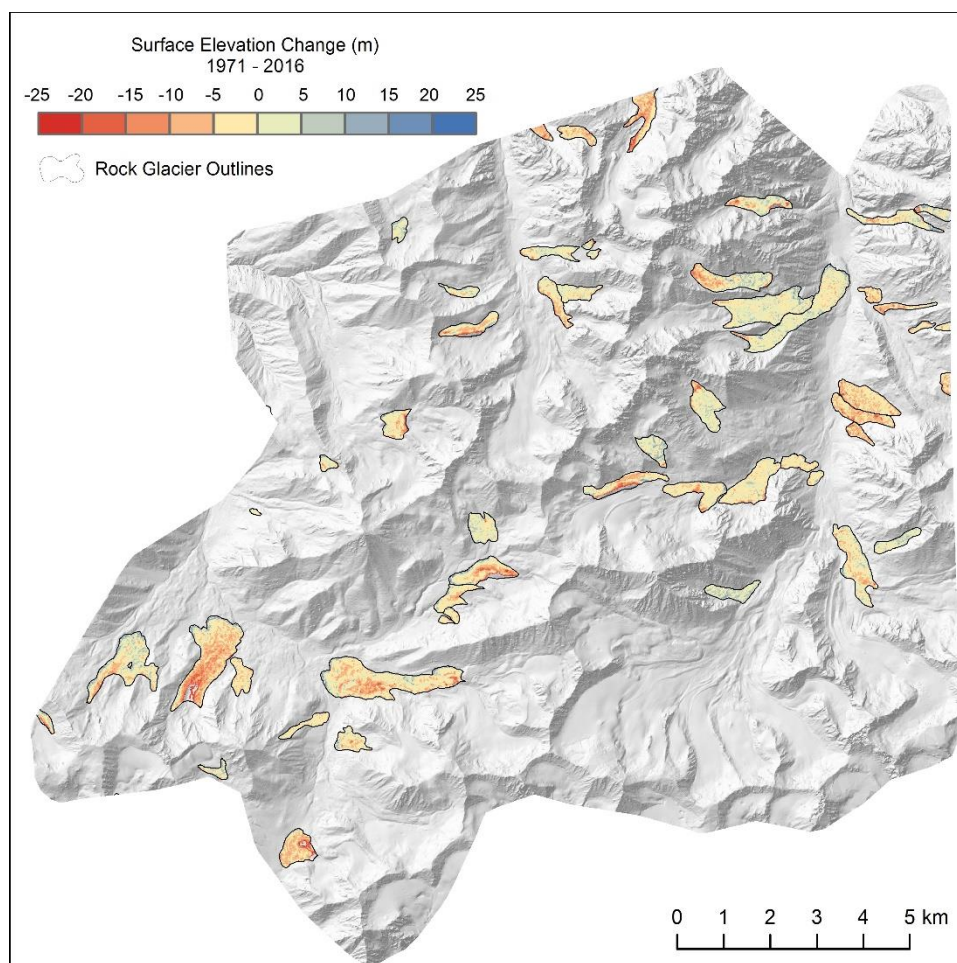


Figure 40: Surface elevation change of rock glaciers (1971-2016). See Figure A2 in the Appendix for full data.

Compared to the rapid surface lowering of glaciers, the total study area's rock glacier surface elevation remained relatively stable over the time period of investigation (Figure 40). The average surface

elevation change over the entire rock glacier area, with outliers removed, was -1.51 ± 6.30 m between 1971 and 2016 (Table 19). From 2012 - 2016, the average elevation change was 0.24 ± 2.02 m. Both of these values suggest an average annual change in the range of only a few centimeters per year.

Table 19: Surface elevation change of rock glaciers.

Measure	1971-2012	1971-2016	2012-2016
Average elevation change (m)	-1.65 ± 6.71	-1.51 ± 6.30	0.24 ± 2.02
Average annual elevation change (ma^{-1})	-0.04 ± 0.35	-0.03 ± 0.33	0.06 ± 0.08

Given the uncertainty of the measurements, and the very small magnitude of change, the 2012-2016 value is likely insignificant. For multi-decadal change, the average negative value of -1.51 ± 6.30 m is influenced by small areas of relatively rapid elevation change in the glacier-affected parts of rock glaciers (discussed below) or where areas, which were within the rock glacier delineation, likely included ice-cored moraines or debris-covered glacier ice. The average elevation change of rock glaciers is less than 1/12 the average elevation change of glaciers over the 45-year span. On an individual basis, some rock glaciers do demonstrate a measurable change. The average surface elevation change for individual rock glaciers (ignoring features which are only partially covered by the DEMs), varies from about -6.5 m to +3.5 m (1971-2016).

Although the signal-to-noise ratio is low, patterns of change for individual features are identifiable in the DoDs, corresponding to information in the imagery and understanding of ongoing processes. For example, surface elevation gain is seen in the DoDs in areas where frontal advance has occurred in recent decades. Similarly, pockets of surface lowering correspond to locations of visible thermokarst subsidence and pond formation. A greater focus is therefore given to individual features, rather than all rock glaciers together, and a more qualitative description of identifiable features is undertaken.

As discussed by Kääb et al. (1997), changes in surface elevation in rock glaciers result from a combination of processes. Sediment accumulation and evacuation, 3D deformation, subsidence from thawing, and frost heave due to freezing, can all be acting at the same time (Kääb et al., 1997). This simultaneous ‘growth and degradation of permafrost’ noted by Kääb et al. (1997; p. 425), is observable in several rock glaciers where both surface elevation gains and losses have occurred in recent decades (e.g. Figure 41).

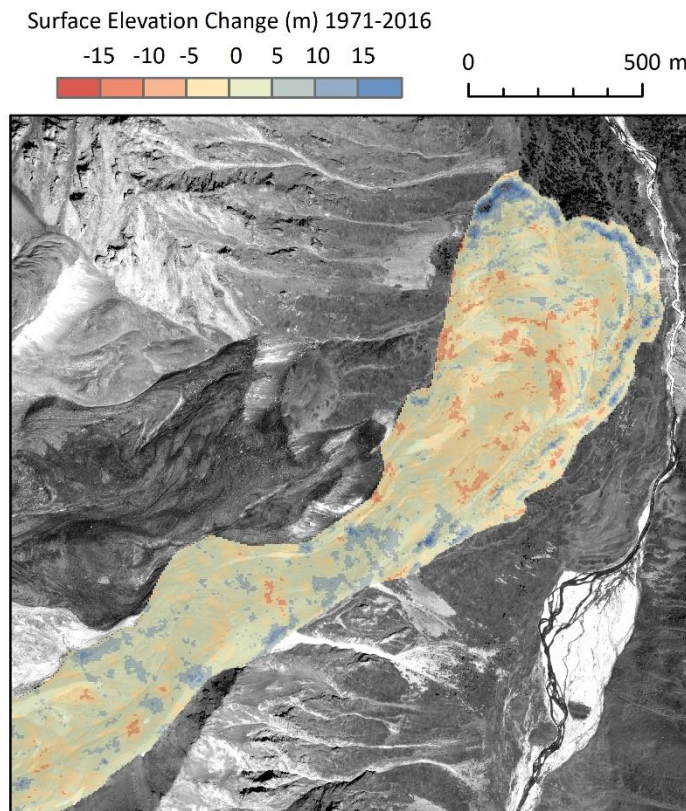


Figure 41: Ordzhonikidze Rock Glacier surface elevation change (1971-2016). Surface elevation gains and losses are heterogeneous. Front advance can be seen in high positive values at the toe.

Several of the large, moraine-type rock glaciers can be divided into two zones: a “glacier-affected” part and a periglacial part. The glacier-affected part, in the upper area of the feature, is dominated by surface subsidence and may have the appearance of thermokarst features. In contrast, the periglacial part, where ridges and furrows are common, generally shows no significant homogenous signal in surface elevation change. Kääb et al. (1997) described how Holocene advance and retreat cycles of the Gruben Glacier have affected the upper part of the Gruben Rock Glacier. Glacier advances overrode the upper part of the rock glacier, and, upon retreat, left behind massive dead-ice below a layer of debris. Surface subsidence is evidence of the dead ice, which is in thermal disequilibrium (Kääb et al., 1997). Similar processes were noted by Bolch et al. (2016) in the Ak-Shiirak Range of Inner Tien Shan, based on DEM differencing and ground penetrating radar (GPR) measurements. The GPR measurements at two moraine–rock glacier landforms in Ak-Shiirak confirmed the existence of massive ice in the glacier-affected parts of these features (Bolch et al., 2016). While no GPR measurements are available for this study, the similar pattern of surface lowering in the upper reaches of moraine-type rock glaciers is indicative of this process. Several rock glaciers, including Morenny, Gorodetsky and Perevallny, exhibit signs of having been overridden by glacier advance during the Little Ice Age (LIA), resulting in the surface subsidence and thermokarst features in the upper regions (e.g. **Figure 42**).

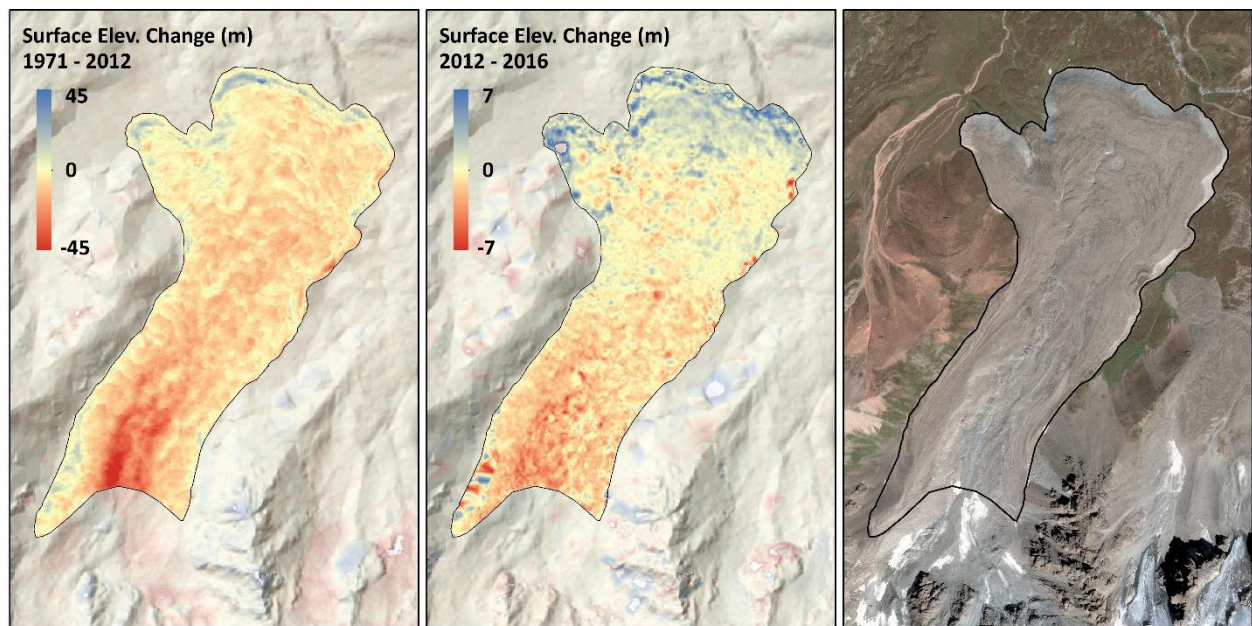


Figure 42: Morenny Rock Glacier. Left: surface elevation change (1971-2012). Middle: Surface elevation change (2012-2016). Note the different elevation change scales for the two different time periods. Surface elevation change is mostly negative, with greatest elevation losses in the upper glacier-affected region. Right: A slight colour variation is noticeable in the glacier-affected part of Morenny rock glacier and signs of thermokarst are present. The periglacial part shows deformation features (ridges and furrows).

6.2.3 Rock glacier horizontal surface displacement

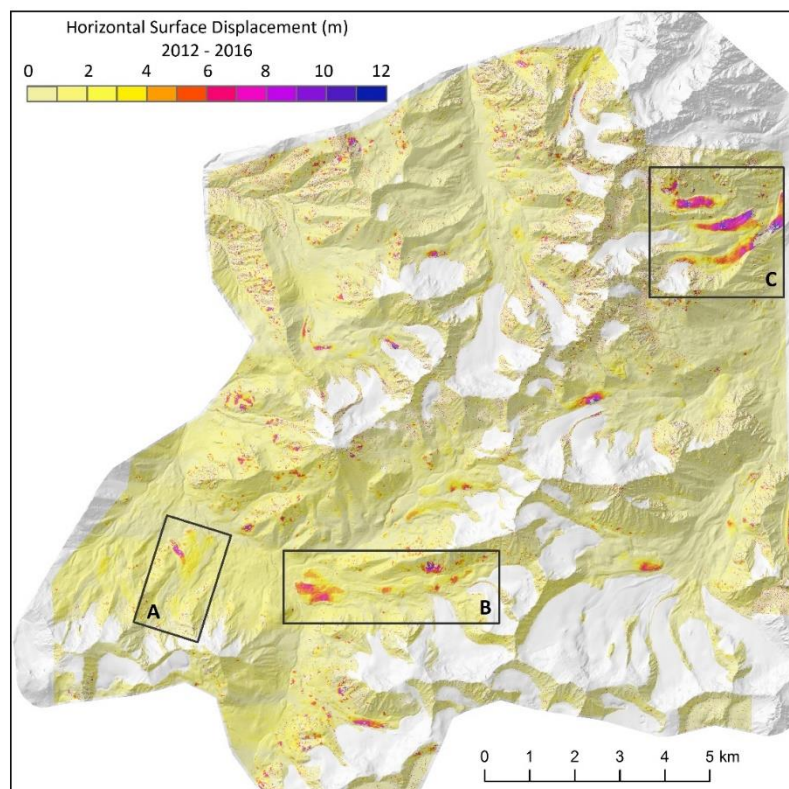


Figure 43: Overview of COSI-Corr image tracking results showing horizontal surface displacement between 2012 and 2016. Highlighted areas A, B, and C are shown in more detail in Figures 41, 42, and 43, respectively. See Figure A4 in the Appendix for data.

Horizontal surface displacements as high as ~ 12 m were identified through image matching of the 2012 and 2016 imagery. This indicates surface displacement rates of up to 3 m per year in some highly active areas. These movement rates are remarkable compared to, for example, the well-studied rock glaciers of the Swiss Alps, where annual surface displacements are generally only a few tens of centimeters (Kääb, 1998). Ignoring inactive rock glaciers and features not fully covered by the displacement raster, the average displacement (2012-2016) was 1.78 ± 1.20 m, or 0.44 ± 0.30 m per year. In general, the results shown in **Figure 43** match well with the InSAR-based displacement rates of Strozzi et al. (2017), which classifies rock glacier polygon activity levels as cm/year, cm/month, or dm/month.

Looking at individual features, the COSI-Corr results demonstrate the spatial variability of rock glacier movement. At Morenny rock glacier for example (**Figure 44**), the western tongue shows displacement as high as ~ 10 m, while the main lobe has maximum displacements of ~ 5 m (2012-2016). The glacier-affected part of Morenny rock glacier, where melt of debris-covered ice is causing subsidence, shows almost no horizontal displacement. The same is true of other glacier-affected areas of rock glaciers.

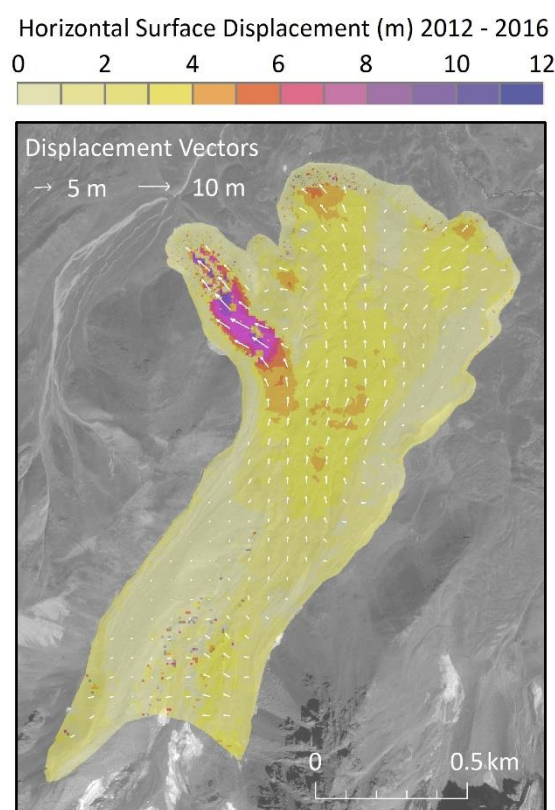


Figure 44: Horizontal surface displacement (2012 - 2016) at Morenny Rock glacier (inset A from Figure 40). Uncertainty of displacement measurements is ± 0.69 m E/W and ± 0.98 m N/S.

The maximum surface displacements at Gorodetsky rock glacier were slightly lower than at Morenny, with values of about 7 m (2012 – 2016). The area of greatest displacement was in the southern half of the tongue, where the frontal advance is also most evident between 1971 and 2016. Gorodetsky

rock glacier and the glacier forefields above it are shown in **Figure 45**. Areas dominated by thermokarst activity show little horizontal displacement.

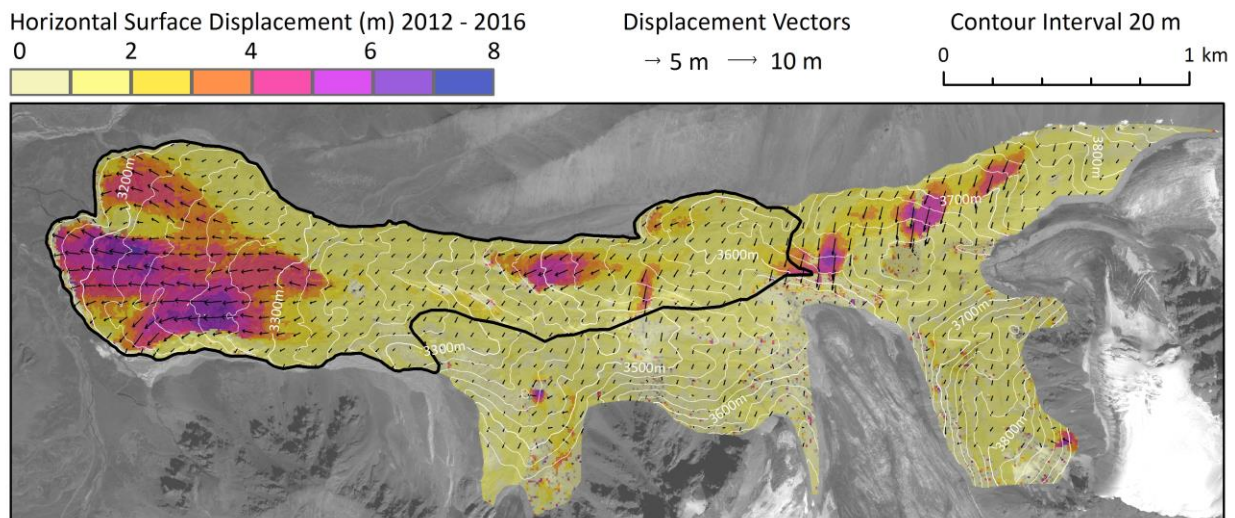


Figure 45: Horizontal surface displacement (2012 – 2016) at Gorodetsky rock glacier (black outline) and the glacier forefield area above (inset B from Figure 40). Uncertainty of displacement: ± 0.69 m E/W and ± 0.98 m N/S.

The greatest horizontal displacements were observed in the area of Ordzhonikidze Rock Glacier in the Left Talgar valley (**Figure 47**). Here, surface displacements are as high as ~ 12 m (2012–2016). For the 2009–2013 time period, Sorg et al. (2015; supplementary material) found average annual displacements of about 1.18 m/a in the lower part, 0.5 m/a in the middle part, and 1.8 m/a in the upper part of Ordzhonikidze (**Figure 46**). The lower part is not fully covered by the GeoEye-1 (2012) imagery and therefore cannot be compared. The 1971–2016 results are shown for the lower, middle, and upper parts, and the 2012–2016 results are shown for the middle and upper parts, for comparison to results from Sorg et al. (2015; (**Figure 46**). (The COSI-Corr results combining GeoEye-1 and CORONA imagery were less successful and are not presented).

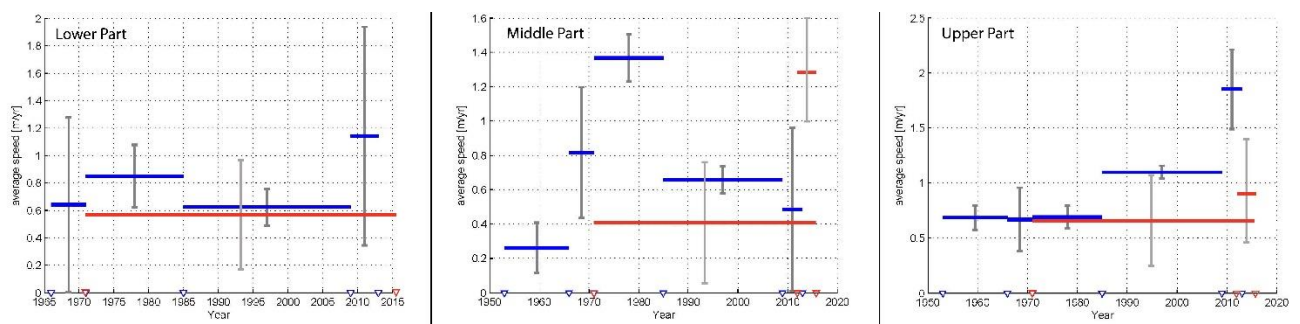


Figure 46: Ordzhonikidze rock glacier average surface speeds. Results of Sorg et al. (2015) in blue. Results from this study in red. Note the different axes for the three regions (lower, middle, and upper). Region divisions were created based on figure S13 from Sorg et al. (2015). Figure modified from Sorg et al. (2015, supplementary materials).

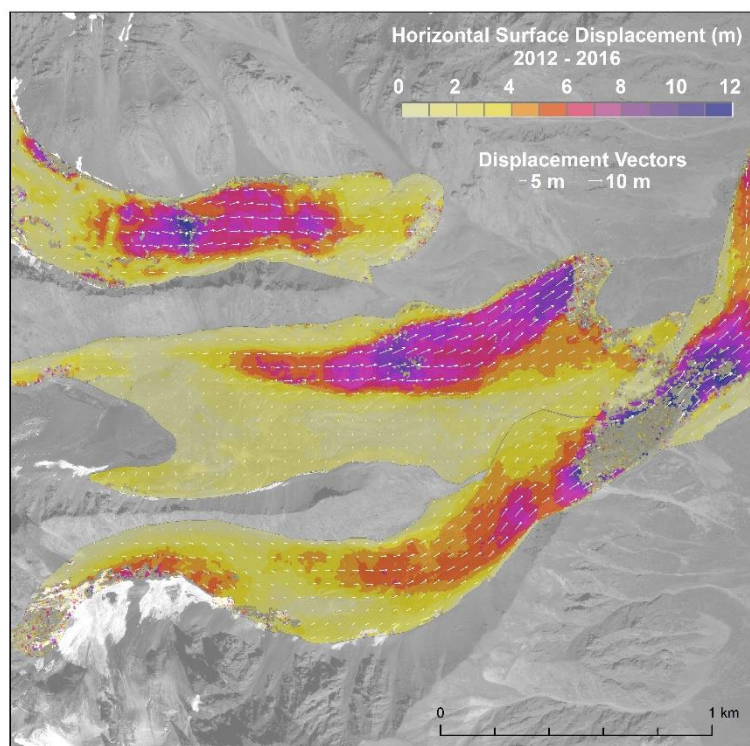


Figure 47: An area of high activity (inset C from figure 40), including Ordzhonikidze rock glacier. Uncertainty of displacement measurements is ± 0.69 m E/W and ± 0.98 m N/S.

Displacement results for the 1971-2016 time period were generally quite noisy but some areas showed reasonable patterns. Displacement results for four areas are shown in **Figure 48** (see Figure A5 in the Appendix for full data).

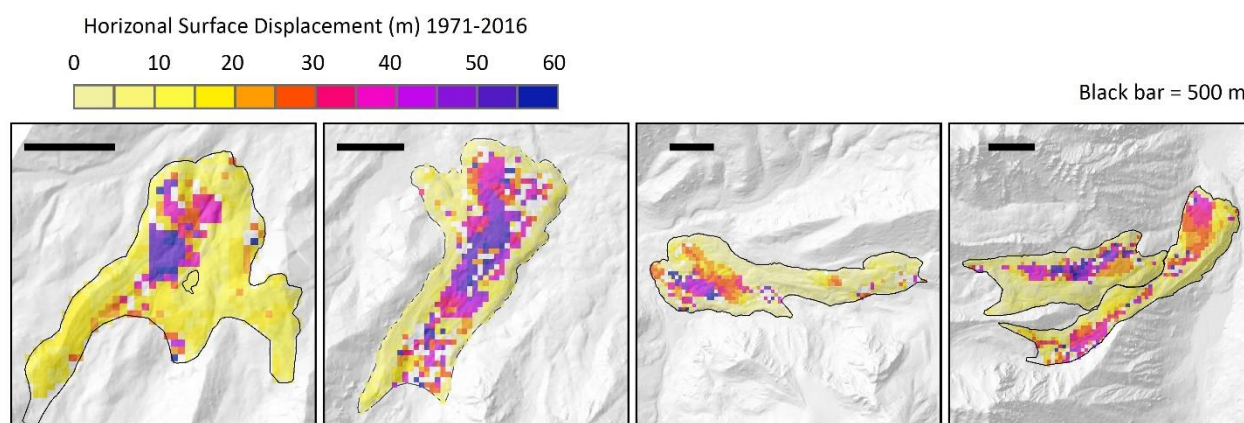


Figure 48: Horizontal surface displacements for 4 regions (1971-2016). Uncertainty of displacement measurements is ± 5.05 m E/W and ± 3.15 m N/S.

Ideally the long-term displacement measurements between the CORONA and Pléiades imagery provide an opportunity to identify changes in surface displacement rates over time. **Figure 49** shows the COSI-Corr results, converted to average annual displacement, of three areas for both the modern satellite imagery (2012-2016) and the CORONA imagery (1971-2016). The accuracy and completeness of the

CORONA-Pléiades displacements is questionable. The longer the interval between images, the more likely it is that the appearance of features will not be preserved. However, the comparison does perhaps show changes in displacement patterns over time. For example, at Morenny rock glacier, the western branch shows very low annual displacement in the long term record but rapid movement in the recent time period, indicating a change in dynamics.

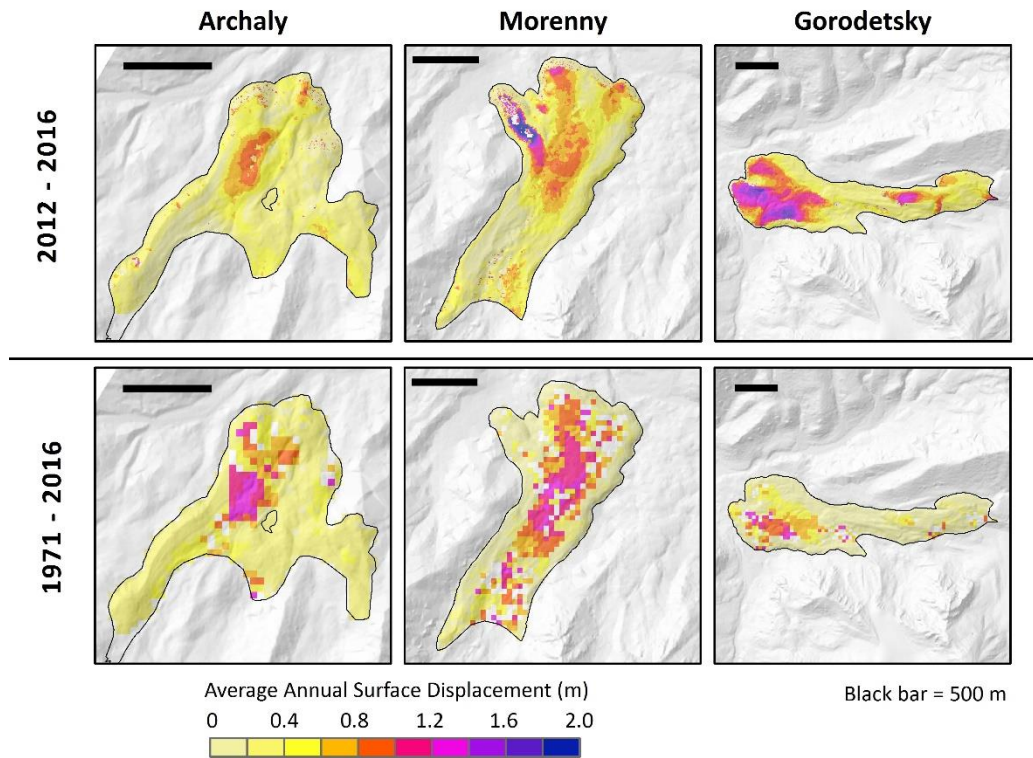


Figure 49: Comparison of COSI-Corr displacement results for three rock glacier areas for the 2012-2016 time period (top) and 1971-2016 period (bottom).

6.3 Additional identifiable features

Along with glacier and rock glacier surface elevation change, some other interesting features could be detected and measured from the DEMs. Significant erosion scars (6.3.1) are notable along the banks of several streams, indicative of flooding or mudslide events. The surface lowering of ice-cored moraines (6.3.2) can be identified in multiple locations.

6.3.1 Debris flows

Several areas along streams show evidence of flood or debris flow events, which removed vegetation and left behind steep, incised banks. One example is seen in the northwest part of the study area, where a region of surface elevation lowering clearly corresponds to bank erosion in the modern satellite imagery (Figure 52). The volume of material removed within the delineated area is approximately $4.29 \times 10^6 \text{ m}^3$ and further indications of erosion are also present upstream and downstream from this most

prominent feature. This stream joins the outflow of Big Almaty Lake about 4 km downstream. A roadway and numerous buildings are located along the river bank a short distance down river. Upstream lay the Sovjetov, Gorelnik and Lokomotiv Glaciers, and several lakes, as well as a large area of debris-covered ice. The lakes were identified as potentially dangerous and were classified as level 3 (medium dangerous), in an assessment of potentially dangerous glacier lakes in Northern Tien Shan (Bolch et al., 2011). A glacier lake outburst flood (GLOF) triggered this event (Blagoveshchenskiy & Yegorov, 2009; Blagoveshchenskiy et al., 2015).

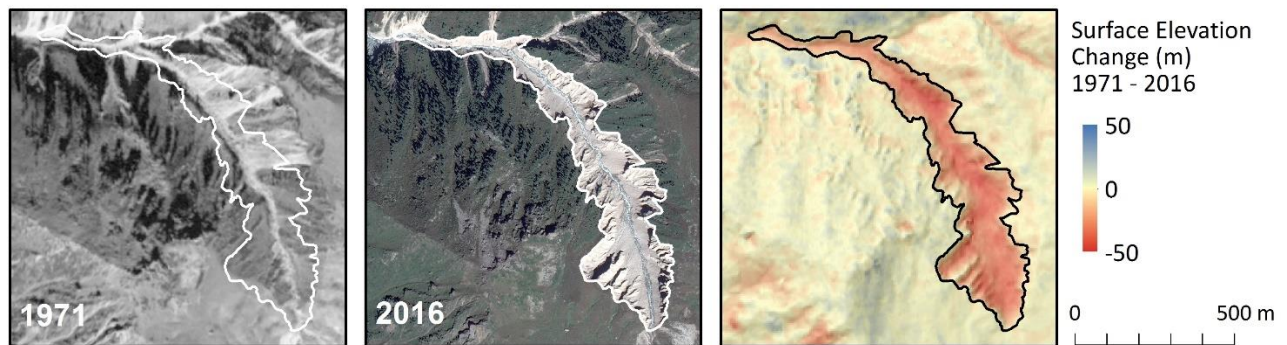


Figure 50: Erosion along a stream in the northwest part of the study area. The clear scarp in the 2016 imagery (centre) can be compared to the same area in 1971 (left), before the erosion took place. The elevation difference between the CORONA DEM and the Pléiades DEM illustrates the degree of material removed.

Debris/mudflows and flash flooding events like this are common in Northern Tien Shan (Thurman, 2011) and several anti-mudflow dams are in place to protect Almaty, including down valley from this erosion scar. The Medeu dam lies further east below the Kishi Almaty valley and was critical in protecting the city from a large 1973 mudslide. A similar event in 1921 killed over 500 people. A report by the government of Kazakhstan (Ministry of Environment Protection, 2009) states that mudslide activity like the 1921 event will become increasingly likely with continued deglaciation. The Medeu dam mudflow storage capacity is expected to be exceeded by 2030-2040 (Ministry of Environment Protection, 2009).

Glacier retreat over the past several decades has led to the formation of numerous new lakes in this region (examples in **Figure 51**). Glacier lake outburst floods (GLOF, or jökullhlaup), could be triggered by a number of processes including moraine failure, degradation of permafrost, or increased water pressure (Bolch et al., 2011). Based on a quick visual search, at least 29 new lakes and ponds were identified in the proglacial areas in the modern satellite imagery that were not present in the CORONA imagery.

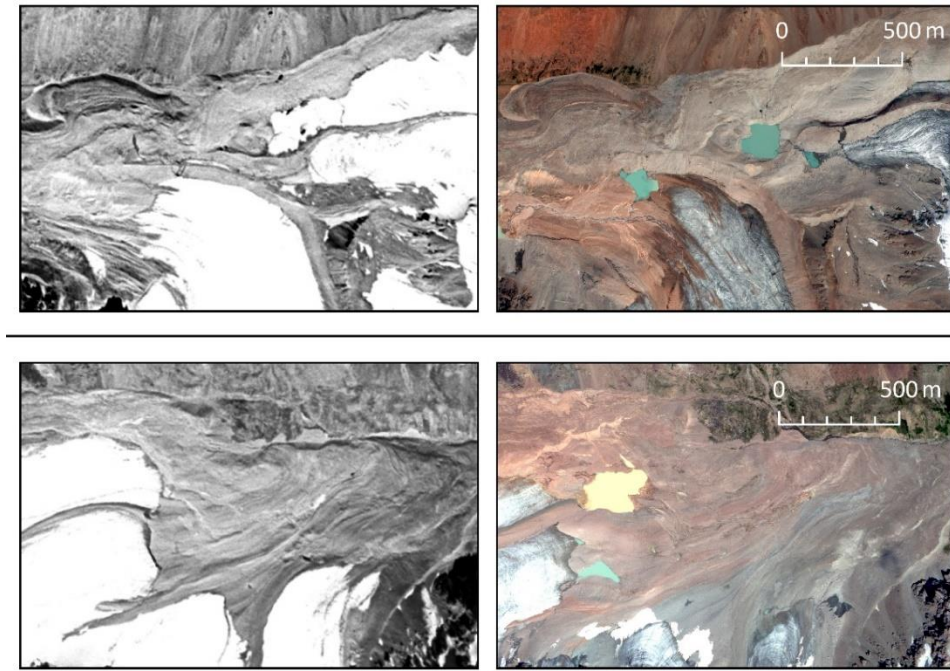


Figure 51: Lake formation following glacier retreat. Left: two pro-glacial areas as seen in the 1971 CORONA imagery. Right: the same areas in 2012 with multiple lakes. These lakes are potential sources of flood or mudslide hazards.

Evidence of another debris flow event is found directly below one of the inventoried rock glaciers in the Left Talgar valley (**Figure 51**). The toe of the rock glacier itself was largely eroded away between 1971 and 2016. Surface elevation change was in the range of -25 m to -50 m in the newly formed gorge. The volume of debris evacuated could cause significant infrastructure damage and potentially loss of life.



Figure 52: A rock glacier with a large debris flow scar. The lower part of the rock glacier was washed away.

6.3.2 Surface lowering of ice-cored moraines

Surface elevation change is also visible in proglacial areas where debris-covered dead ice and ice-cored moraines have downwasted in recent decades. In some of these debris-covered areas, the magnitude of surface lowering is as great as ~-50 m. A few prominent linear features are notable in the DoDs as ice-cored moraines, including the medial moraines which extend from the terminus of Dmitrieva Glacier in Left Talgar. The moraines show significant surface lowering between 1971-2012 (**Figure 53**), but the same

pattern is not observable between 2012 and 2016. This suggests that the ice-core has either largely melted or is now insulated by a thicker debris mantle and the melt-rate has significantly slowed.

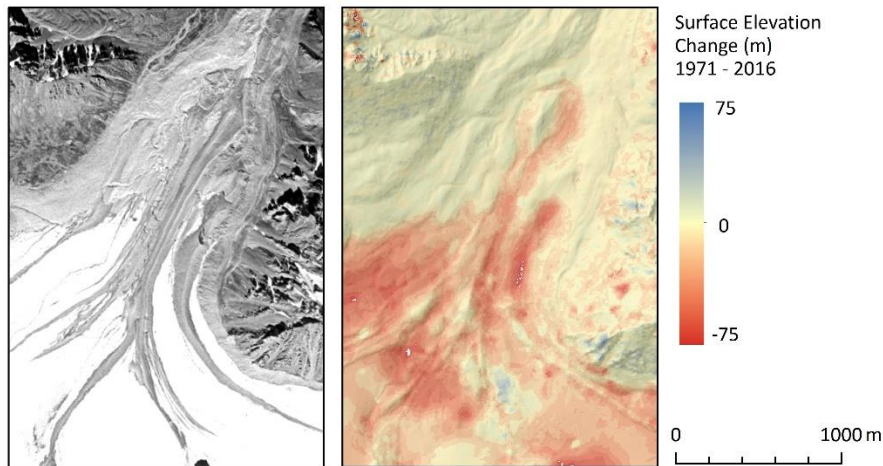


Figure 53: CORONA 1971 image of Dmitrieva Glacier, showing position of medial moraines (left). Surface elevation change (1971-2016) showing lowering of ice-cored moraines.

Similar observations were made at the medial moraine between Tuyuksu Glacier and Igli Tuyuksu Glacier in Kishi Almaty (**Figure 54**). In this area, the surface lowering of the moraine was also visible in the 2012-2016 elevation difference raster.

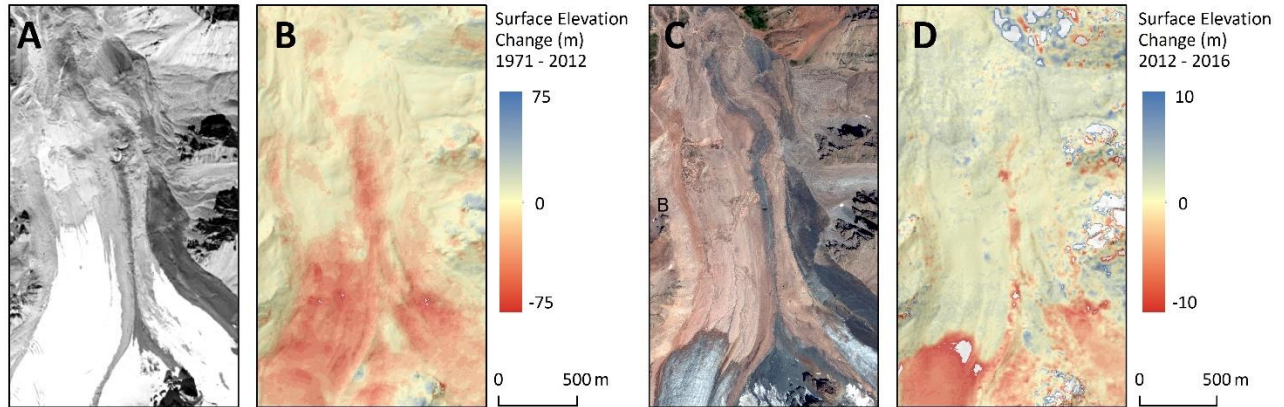


Figure 54: Surface elevation change near the Tuyuksu Glacier terminus. 1971 CORONA imagery (A) shows location of medial moraine. Surface lowering of the moraine was as great as -50 m between 1971 and 2012 (B). GeoEye-1 imagery (C) shows the terminus position in 2012 and the moraine. Average surface elevation lowering of the moraine is about -5 m between 2012 and 2016 (D). Note the different colour scales for the two surface elevation change rasters.

6.4 Discussion of all results and findings

As glaciers continue to shrink in this region, the relative area of rock glaciers compared to glaciers is increasing. In Ulken Almaty valley, the rock glacier area was about 32 % of the glacier area in 1971, and is now over 48 % of the current glacier area. Similarly, in Kishi Almaty valley, the rock glacier/glacier area percentage was about 25 % in 1971 and is now closer to 37%. (Note that these are rough estimates because

rock glaciers were not delineated based on the 1971 imagery, but in general, area changes of rock glaciers have been very small compared to area changes of glaciers. Also, Left Talgar valley is not discussed in this context because it is only partially covered by the modern satellite imagery.) Rock glacier to glacier area ratios reported by Bolch & Marchenko (2007) suggested lower values, because fewer rock glaciers could be identified using lower resolution imagery. Their estimate of the rock glacier area compared to glacier area was 29% in Ulken Almaty and 9% in Kishi Almaty. Even with these lower values, they estimated that rock glacier ice was equivalent to 9.4% of the glacier ice in Ulken Almaty and 2.5 % in Kishi Almaty. Given the ongoing loss of glacier ice ($-0.31 \pm 0.11 \text{ km}^3$ in these two valleys alone, 1971-2016), and the relatively slow changes in rock glaciers, it is likely that the ice stored in rock glaciers, as a percentage of the total ice in the valley, is increasing. The significance of this is perhaps greatest in Ulken Almaty valley, where not only is the ratio of rock glacier ice to glacier ice the greatest, but the valley is also a crucial water source for the city of Almaty (Bolch & Marchenko, 2007).

Based on the 45-year surface elevation change observations, rock glaciers are also predominantly subsiding, albeit at a much slower rate than glaciers. **Figure 55** illustrates surface elevation change and horizontal displacements at Gorodetsky Rock Glacier and the glacier forefields above it (the numbers from the upper part of the figure are referenced in the following paragraphs with #). The patterns of surface elevation change observed for rock glaciers are quite different from those of glaciers. Glaciers typically have greatest elevation losses at lower elevations in the ablation zone (Fig. 55, #7). Rock glaciers, on the other hand, show heterogeneous elevation gain and loss in the lower periglacial part (Fig. 55, #2), and greatest elevation change was found in the glacier-affected parts of moraine-derived rock glaciers, closer to the head (Fig. 55, #3). These areas of substantial subsidence reflect, as described by Kääb et al. (1997), debris-covered dead glacier ice in thermal disequilibrium. Further evidence of dead ice downwasting is seen at #6 (Fig. 55). Elevation gain is also seen at the fronts of advancing rock glaciers (Fig. 55 #1) or advancing lobes within rock glaciers (Fig. 55, #4 & #5).

Horizontal surface displacements of rock glaciers are also heterogeneous within the study area and within individual features. The surface velocities were greatest in the periglacial part (Fig. 55, #2), but the level of activity varies, and at Gorodetsky Rock Glacier, the displacements along the northern side of the frontal lobe are very low compared to the southern and central parts. Where pockets of high displacement exist within the rock glacier, they may correspond to advancing lobes with positive surface elevation change (Fig. 55, #4). In the glacier forefield area, the direction of displacement is toward the area of subsidence where lakes and ponds have formed (Fig. 55, #8). Horizontal surface displacements are generally low in the glacier-affected parts of rock glaciers, and where surface lowering is greater.

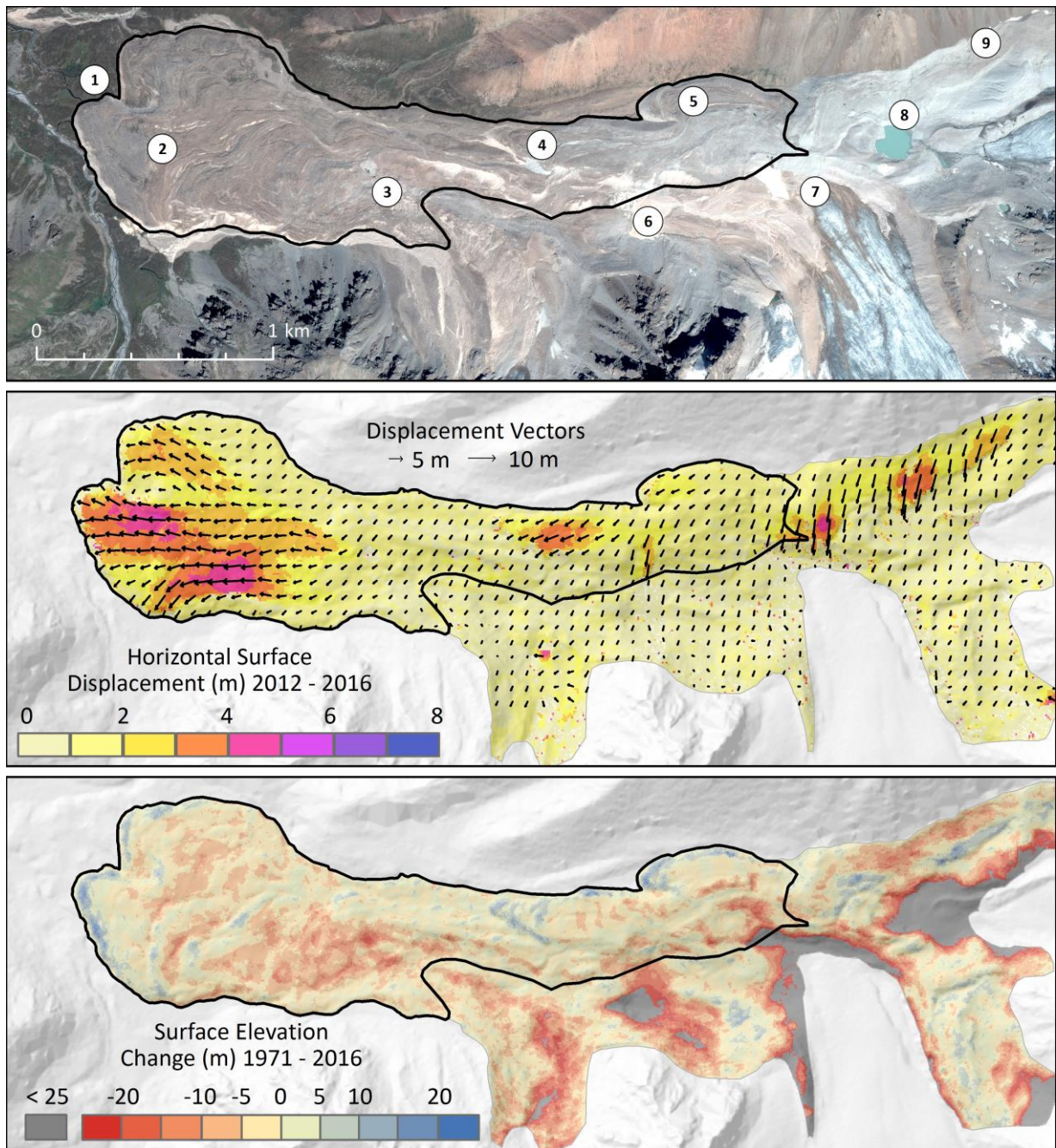


Figure 55: Gorodetsky Rock glacier. Top: Orthoimage with numbers corresponding to notes in the text. Middle: Horizontal Surface Displacement (2012-2016). Bottom: Surface elevation change (1971-2016).

Beyond the features delineated as glaciers and rock glaciers, it is clear that there is a significant amount of ice elsewhere in the study area. Debris-covered dead ice is found in glacial-forefields where thermokarst features are visible, and in ice-cored moraines which experienced significant surface lowering in the range of 10s of meters over several decades. These areas (e.g. Fig. 55, # 9) represent another component of cryosphere change in these valleys, which could be overlooked if observations focus only on glaciers and rock glaciers. These regions are also associated with hazards: potentially dangerous lakes have formed, and evidence of outburst floods and debris flows, large enough to cause serious damage to people or infrastructure, can be seen in several locations.

7 CONCLUSION

This thesis investigates glacier and rock glacier change in a region of Northern Tien Shan, where glacial and periglacial processes are important factors in local water supply and hazard management. The high resolution of the employed satellite imagery, and the long temporal window afforded by declassified CORONA KH-4B imagery, allow for both recent and long-term change detection and measurement.

7.1 Key findings

- Total **glacier area** over the full 45-year time period of investigation (1971 – 2016) decreased from 55.5 ± 3.8 km² to 39.1 ± 1.4 km², a relative loss of 29.3 ± 2.1 %. The average rate of relative area loss per year in the 2012-2016 period (-1.4 % / year) was more than two times higher than the average of the previous four decades (-0.6 % / year).
- **Geodetic mass balance** for the study area was -0.34 ± 0.14 m w.e. a⁻¹ (1971-2012) and, again, significantly higher in recent years, at -0.62 ± 0.43 m w.e. a⁻¹ (2012-2016). The earlier geodetic mass (1971-2012), which uses a digital elevation model derived from declassified CORONA imagery, underestimates the mass balance by 34% compared to WGMS glaciological measurements at Tuyuksu Glacier. The 2012-2016 geodetic mass balance corresponds well to the glaciological record, within 7%.
- Compared to the rapid retreat and surface lowering observed at glaciers, the **surface elevation change of rock glaciers** is very low (-1.51 ± 6.30 m, 1971-2016), indicating a much slower response to climate forcing. Individual features show areas of both surface elevation gain and loss. The overall pattern of elevation change is significantly different from that of glaciers.
- **Rock glacier horizontal surface displacements** indicate rapid movement of some rock glaciers, with annual displacements as high as 3 m. Active and inactive parts of individual features can be identified.
- Some moraine-type rock glaciers show evidence of a **glacier-affected part** in the upper reaches, where the rock glacier was overridden by previous advances of the up-valley glacier. These areas are characterized by surface subsidence related to downwasting of debris-covered dead ice, and are in contrast to the **periglacial part** which exhibits ridges and furrows and no clear elevation gain or loss trend.
- The relative importance of **freshwater** contributions from rock glaciers and ground ice may increase in the future if glacier retreat continues to a point where their input to stream flow is significantly reduced.
- Glacier retreat, melt of debris-covered dead-ice, and degradation of ice-rich permafrost features may increase the risk of glacier lake outburst floods and other **periglacial hazards**. Evidence of past flood/mudslide events are seen in the optical imagery and the surface elevation change. New lakes, some of which may be prone to outburst floods, have formed in several pro-glacial areas following glacier retreat.

7.2 Study limitations

Ideally the generation of digital elevation data from stereo satellite imagery would be optimized using high-accuracy differential GPS (dGPS) ground control points, distributed evenly throughout the study area. For

this thesis, the available GCPs were limited to a small area of the total study area and did not have the accuracy of dGPS measurements. Furthermore, the points were not identifiable in all imagery sets. The use of Landsat imagery and SRTM elevation data for GCP generation has been shown to be effective in other studies and was also sufficient here. However, the absolute accuracy of orthoimages, DEMs, and the derived information would be improved with better GCPs.

One major limitation of modern high-resolution satellite imagery (in this case GeoEye-1 and Pléiades) is the high cost compared to freely available medium-resolution imagery and elevation data such as Landsat and SRTM data. While the level of detail and accuracy possible with this imagery is greatly improved, it is also limited by costs to a small spatial area. High variability in climatic and other factors in Tien Shan make it impossible to extrapolate results from one small area to the region as a whole. In this regard, studies which rely on coarser-resolution imagery have an advantage, as the coverage is generally larger.

7.3 Future research

While investigations of this type can provide detailed information, the spatial coverage is small and the manual workload is large. Therefore, automation of processes such as rock glacier identification would be key in expanding studies to a regional scale. InSAR-based methods of semi-automated rock glacier identification (e.g. Strozzi et al., 2017 and Wang et al., 2017) are a major step towards this. The new, high-resolution TanDEM-X global DEM could be a useful tool for monitoring surface elevation change of periglacial environments over a larger area.

This thesis did not focus on climate data and the connection between climate trends and rock glacier behaviour. A better understanding of this relationship would aid predictions of future implications to water resources from ground-ice sources. Similar monitoring methods could be used to measure how surface elevation change and horizontal surface displacements are related to changes in climate.

8 BIBLIOGRAPHY

- Abermann, J., Fischer, A., Lambrecht, A., & Geist, T. (2010). On the potential of very high-resolution repeat DEMs in glacial and periglacial environments. *The Cryosphere*, 4(1), 53-65.
- Aguilar, M. A., del Mar Saldaña, M., & Aguilar, F. J. (2013). Assessing geometric accuracy of the orthorectification process from GeoEye-1 and WorldView-2 panchromatic images. *International Journal of Applied Earth Observation and Geoinformation*, 21, 427-435.
- Aizen, V. B. (2011). Tien Shan Glaciers *Encyclopedia of Snow, Ice and Glaciers* (pp. 1179-1181): Springer.
- Aizen, V. B., Kuzmichenok, V. A., Surazakov, A. B., & Aizen, E. M. (2006). Glacier changes in the central and northern Tien Shan during the last 140 years based on surface and remote-sensing data. *Annals of Glaciology*, 43(1), 202-213.
- Aizen, V. B., Kuzmichenok, V. A., Surazakov, A. B., & Aizen, E. M. (2007). Glacier changes in the Tien Shan as determined from topographic and remotely sensed data. *Global and Planetary Change*, 56(3-4), 328-340. doi:10.1016/j.gloplacha.2006.07.016
- Arendt, A., A. Bliss, T. Bolch, J.G. Cogley, A.S. Gardner, J.-O. Hagen, R. Hock, M. Huss, G. Kaser, C. Kienholz, W.T. Pfeffer, G. Moholdt, F. Paul, V. Radić, L. Andreassen, S. Bajracharya, N.E. Barrand, M. Beedle, E. Berthier, R. Bhambri, I. Brown, E. Burgess, D. Burgess, F. Cawkwell, T. Chinn, L. Copland, B. Davies, H. De Angelis, E. Dolgova, L. Earl, K. Filbert, R. Forester, A.G. Fountain, H. Frey, B. Giffen, N. Glasser, W.Q. Guo, S. Gurney, W. Hagg, D. Hall, U.K. Haritashya, G. Hartmann, C. Helm, S. Herreid, I. Howat, G. Kapustin, T. Khromova, M. König, J. Kohler, D. Kriegel, S. Kutuzov, I. Lavrentiev, R. LeBris, S.Y. Liu, J. Lund, W. Manley, R. Marti, C. Mayer, E.S. Miles, X. Li, B. Menounos, A. Mercer, N. Mölg, P. Mool, G. Nosenko, A. Negrete, T. Nuimura, C. Nuth, R. Pettersson, A. Racoviteanu, R. Ranzi, P. Rastner, F. Rau, B. Raup, J. Rich, H. Rott, A. Sakai, C. Schneider, Y. Seliverstov, M. Sharp, O. Sigurdsson, C. Stokes, R.G. Way, R. Wheate, S. Winsvold, G. Wolken, F. Wyatt, N. Zheltyhina. (2015). Randolph Glacier Inventory – A Dataset of Global Glacier Outlines: Version 5.0. Global Land Ice Measurements from Space, Boulder Colorado, USA. Digital Media.
- Altmaier, A., & Kany, C. (2002). Digital surface model generation from CORONA satellite images. *SPRS Journal of photogrammetry and remote sensing*, 56(4), 221-235.
- Arendt, A. A., Echelmeyer, K. A., Harrison, W. D., Lingle, C. S., & Valentine, V. B. (2002). Rapid wastage of Alaska glaciers and their contribution to rising sea level. *Science*, 297(5580), 382-386.
- Astrium, An EADS Company (2012). *PLÉIADES imagery user guide*.
- Avouac, J. P., Ayoub, F., Wei, S., Ampuero, J. P., Meng, L., Leprince, S., ... & Helmberger, D. (2014). The 2013, Mw 7.7 Balochistan earthquake, energetic strike-slip reactivation of a thrust fault. *Earth and Planetary Science Letters*, 391, 128-134.
- Ayoub, F., Leprince, S., & Keene, L. (2009). User's Guide to COSI-CORR Co-registration of Optically Sensed Images and Correlation. California Institute of Technology: Pasadena, CA, USA, 38.
- Azócar, G. F., & Brenning, A. (2010). Hydrological and geomorphological significance of rock glaciers in the dry Andes, Chile (27°-33°S). *Permafrost and Periglacial Processes*, 21(1), 42-53. doi:10.1002/ppp.669
- Bamber, J. L., & Rivera, A. (2007). A review of remote sensing methods for glacier mass balance determination. *Global and Planetary Change*, 59(1-4), 138-148. doi:10.1016/j.gloplacha.2006.11.031
- Barsch, D. (1992). Permafrost creep and rockglaciers. *Permafrost and Periglacial Processes*, 3(3), 175-188.
- Barsch, D. (1996). Rock glaciers—Indicators for the present and former geoecology. *High Mountain Environments*, 76-82.
- Baumann, S. (2017). Comparison of glacier mass balance data in the Tien Shan and Pamir, Central Asia. *Arctic, Antarctic, and Alpine Research*, 49(1), 133-146.
- Bellisario, A., Ferrando, F., & Janke, J. (2013). Water resources in Chile: the critical relation between glaciers and mining for sustainable water management. *Investig. Geogr*, 46, 3-24.
- Berthling, I. (2011). Beyond confusion: Rock glaciers as cryo-conditioned landforms. *Geomorphology*, 131(3-4), 98-106. doi:10.1016/j.geomorph.2011.05.002.
- Blagoveshchenskiy, V., Yegorov, A.B. (2009). The Ile Alatau Range Natural Hazards, in: Materials of the international conference "Mitigation of natural hazards in mountain areas" Bishkek, Kyrgyzstan. 15.-18.9.2009.
- Blagoveshchenskiy, V., Kapitsa, V., & Kasatkin, N. (2015). Danger of GLOFs in the Mountain Areas of Kazakhstan. *Journal of Earth Science and Engineering*, 5, 182-187.
- Bodin, X., Rojas, F., & Brenning, A. (2010). Status and evolution of the cryosphere in the Andes of Santiago (Chile, 33.5 S.). *Geomorphology*, 118(3), 453-464.
- Bodin, X., Schoeneich, P., Deline, P., Ravanel, L., Magnin, F., Krysiecki, J.-M., & Echelard, T. (2015). Mountain permafrost and associated geomorphological processes: recent changes in the French Alps. *Revue de géographie alpine*(103-2). doi:10.4000/rga.2885

- Bolch, T. (2004). *Using ASTER and SRTM DEMs for studying glaciers and rockglaciers in northern Tien Shan*. Paper presented at the Proceedings Part I of the Conference 'Teoreticheskiye i Prikladnyye Problemy geografii na rubeschje Stoletij' [Theoretical and Applied Problems of Geography on a Boundary of Centuries].
- Bolch, T. (2006). *GIS-und fernerkundungsgestützte Analyse und Visualisierung von Klima-und Gletscheränderungen im nördlichen Tien Shan (Kasachstan, Kyrgyzstan): mit einem Vergleich zur Bernina-Gruppe, Alpen*. Tobias Bolch.
- Bolch, T. (2007). Climate change and glacier retreat in northern Tien Shan (Kazakhstan/Kyrgyzstan) using remote sensing data. *Global and Planetary Change*, 56(1-2), 1-12. doi:10.1016/j.gloplacha.2006.07.009
- Bolch, T., Buchroithner, M., Pieczonka, T., & Kunert, A. (2008). Planimetric and volumetric glacier changes in the Khumbu Himal, Nepal, since 1962 using CORONA, Landsat TM and ASTER data. *Journal of Glaciology*, 54(187), 592-600.
- Bolch, T. (2015). Glacier area and mass changes since 1964 in the Ala Archa Valley, Kyrgyz Ala-Too, northern Tien Shan. *Ice and Snow*, 129(1), 28-39.
- Bolch, T., & Gorbunov, A. P. (2014). Characteristics and Origin of Rock Glaciers in Northern Tien Shan (Kazakhstan/Kyrgyzstan). *Permafrost and Periglacial Processes*, 25(4), 320-332. doi:10.1002/ppp.1825
- Bolch, T., Kamp, U., & Olsenholler, J. (2005). Using ASTER and SRTM DEMs for studying geomorphology and glaciation in high mountain areas. *New Strategies for European Remote Sensing*, 119-127.
- Bolch, T., & Marchenko, S. S. (2006). Significance of glaciers, rockglaciers and ice-rich permafrost in the Northern Tien Shan as water towers under climate change conditions.
- Bolch, T., Peters, J., Yegorov, A., Pradhan, B., Buchroithner, M., & Blagoveshchensky, V. (2011). Identification of potentially dangerous glacial lakes in the northern Tien Shan. *Natural Hazards*, 59(3), 1691-1714. doi:10.1007/s11069-011-9860-2
- Bolch, T., Pieczonka, T., & Benn, D. I. (2011). Multi-decadal mass loss of glaciers in the Everest area (Nepal Himalaya) derived from stereo imagery. *The Cryosphere*, 5(2), 349-358.
- Bolch, T., Yao, T., Kang, S., Buchroithner, M. F., Scherer, D., Maussion, F., Huintjes, & Schneider, C. (2010). A glacier inventory for the western Nyainqentanglha Range and the Nam Co Basin, Tibet, and glacier changes 1976-2009. *The Cryosphere*, 4(3), 419.
- Bolch, T. (2017). Hydrology: Asian glaciers are a reliable water source. *Nature*, 545(7653), 161-162.
- Brenning, A. (2009). Benchmarking classifiers to optimally integrate terrain analysis and multispectral remote sensing in automatic rock glacier detection. *Remote Sensing of Environment*, 113(1), 239-247.
- Chedija O.K. (1986) Morphostructures and recent tectogenesis of the Tien Shan (in Russian). Ilim:Frunse, 314.
- Chen, Y., Li, W., Deng, H., Fang, G., & Li, Z. (2016). Changes in Central Asia's Water Tower: Past, Present and Future. *Scientific reports*, 6.
- Delaloye, R., Perruchoud, E., Avian, M., Kaufmann, V., Bodin, X., Hausmann, H., . . . Krainer, K. (2008). *Recent interannual variations of rock glacier creep in the European Alps*. Paper presented at the Proceedings of the 9th International Conference on Permafrost, Fairbanks, Alaska.
- DigitalGlobe (2016). Accuracy of Worldview Products. <https://www.digitalglobe.com/resources/white-papers>. Accessed Feb. 13, 2017.
- Dozier, J. (2009). Remote Sensing of the Cryosphere, 397-410. doi:10.4135/9780857021052.n28.
- Dyurgerov, M. B. (2010). Reanalysis of glacier changes: from the IGY to the IPY, 1960–2008. *Data of Glaciological Studies*, 108, 1-116.
- Farinotti, D., Longuevergne, L., Moholdt, G., Duethmann, D., Mölg, T., Bolch, T., . . . Güntner, A. (2015). Substantial glacier mass loss in the Tien Shan over the past 50 years. *Nature Geoscience*, 8(9), 716-722. doi:10.1038/ngeo2513
- Frauenfelder, R., & Kääb, A. (2000). Towards a palaeoclimatic model of rock-glacier formation in the Swiss Alps. *Annals of Glaciology*, 31(1), 281-286.
- Galiatsatos, N., Donoghue, D. N., & Philip, G. (2007). High Resolution Elevation Data Derived from Stereoscopic CORONA Imagery with Minimal Ground Control. *Photogrammetric Engineering & Remote Sensing*, 73(9), 1093-1106.
- Gardner, A. S., Moholdt, G., Cogley, J. G., Wouters, B., Arendt, A. A., Wahr, J., ... & Ligtenberg, S. R. (2013). A reconciled estimate of glacier contributions to sea level rise: 2003 to 2009. *science*, 340(6134), 852-857.
- Glazovskiy, A.F. (1978). Kamenije Glechery Basseyna R Bolshoy Almatinka (=Rock Glaciers in the Large Almatinka Valley). In A.P. Gorbunov (Ed.), *Kriogennyye Jablenia Visokogorij* (pp. 85–92): Akademia Nauk SSSR.
- Goerlich, F., Bolch, T., Mukherjee, K., & Pieczonka, T. (2017). Glacier Mass Loss during the 1960s and 1970s in the Ak-Shirak Range (Kyrgyzstan) from Multiple Stereoscopic CORONA and Hexagon Imagery. *Remote Sensing*, 9(3), 275.
- Golosokov, V. (1949). Derevnije ledniki v Zailijskom Atalau (=Old Glaciers in Zailijskij Alatau). *Vostochnik Akademia Nauk KasSSR*, 1, 80–82.
- Gorbunov, A.P. (1979). Kamennije Glechery Zailijskogo Alatau (= Rock Glaciers of Zailiskiy Alatau). In *Kriogennyye Javlnija Kasakhstana i Crednej Asii* (pp. 5–34). Yakutsk: Akademia Nauk SSSR

- Gorbunov, A. P. (1983). *Rock glaciers of the mountains of middle Asia*. Paper presented at the Proc. 4th Int. Conf. on Permafrost, Fairbanks, Alaska. National Academic Press, Washington.
- Gorbunov, A. P., Marchenko, S. S., & Severskiy, E. V. (2004). The thermal environment of blocky materials in the mountains of Central Asia. *Permafrost and Periglacial Processes*, 15(1), 95-98. doi:10.1002/ppp.478
- Gorbunov, A. P., Severskiy, E. V., Titkov, S. N., Marchenko, S. S., & Popov, M. (1998). *Rock glaciers, Zailiyskiy Range, Kungei Ranges, Tienshan, Kazakhstan*. Retrieved from: http://nsidc.org/data/docs/fgdc/ggd501_rockglac_kazakh/
- Gorbunov, A. P., & Severskiy, E. (1998). Otcenka zapasov podzemnykh l'dov Severnogo Tan-Shanya. (= The estimation of ground ice volume in the Northern Tien Shan). *Hydrometeorology and ecology*, 3-4.
- Gorbunov, A. P., & Severskiy, E. V. (1999). Solifluction in the mountains of Central Asia: distribution, morphology, processes. *Permafrost and Periglacial Processes*, 10(1), 81-89.
- Gorbunov, A., & Titkov, S. (1989). Kamennyye Gletchery Gor Srednej Azii (=Rock Glaciers of the Central Asia Mountains). Irkutsk: Akademia Nauk SSSR.
- Gorbunov, A. P., Titkov, S. N., & Polyakov, V. G. (1992). Dynamics of rock glaciers of the northern Tien Shan and the Djungar Ala Tau, Kazakhstan. *Permafrost and Periglacial Processes*, 3(1), 29-39.
- Granshaw, F. D., & Fountain, A. G. (2006). Glacier change (1958–1998) in the north Cascades national park complex, Washington, USA. *Journal of Glaciology*, 52(177), 251-256.
- Grodecki, J., & Dial, G. (2003). Block adjustment of high-resolution satellite images described by rational polynomials. *Photogrammetric Engineering & Remote Sensing*, 69(1), 59-68.
- Haeblerli, W. (1985). Creep of mountain permafrost: Internal structure and flow of alpine rock glaciers.
- Haeblerli, W. (2000). Modern research perspectives relating to permafrost creep and rock glaciers: a discussion. *Permafrost and Periglacial Processes*, 11(4), 290-293.
- Haeblerli, W., Hallet, B., Arenson, L., Elconin, R., Humlum, O., Kääb, A., . . . Mühll, D. V. (2006). Permafrost creep and rock glacier dynamics. *Permafrost and Periglacial Processes*, 17(3), 189-214. doi:10.1002/ppp.561
- Hagg, W. J., Braun, L. N., Uvarov, V. N., & Makarevich, K. G. (2004). A comparison of three methods of mass-balance determination in the Tuyuksu glacier region, Tien Shan, Central Asia. *Journal of Glaciology*, 50(171), 505-510.
- Hagg, W., Braun, L., Weber, M., & Becht, M. (2006). Runoff modelling in glacierized Central Asian catchments for present-day and future climate. *Hydrology Research*, 37(2), 93-105.
- Hamilton, S. J., & Whalley, W. B. (1995). Rock glacier nomenclature: A re-assessment. *Geomorphology*, 14(1), 73-80.
- Harris, S. A., French, H. M., Heginbottom, J. A., Johnston, G. H., Ladanyi, B., Sego, D. C., & van Everdingen, R. O. (1988). Glossary of permafrost and related ground-ice terms. *Permafrost Subcommittee. Associate Committee on Geotechnical Research, National Research Council of Canada, Ottawa*, 156.
- Heid, T. (2011). *Deriving glacier surface velocities from repeat optical images*. University of Oslo.
- Heid, T., & Kääb, A. (2012). Evaluation of existing image matching methods for deriving glacier surface displacements globally from optical satellite imagery. *Remote Sensing of Environment*, 118, 339-355. doi:10.1016/j.rse.2011.11.024
- Höhle, J., & Höhle, M. (2009). Accuracy assessment of digital elevation models by means of robust statistical methods. *ISPRS Journal of Photogrammetry and Remote Sensing*, 64(4), 398-406.
- Hughes, P., Gibbard, P., & Woodward, J. (2003). Relict rock glaciers as indicators of Mediterranean palaeoclimate during the Last Glacial Maximum (Late Würmian) in northwest Greece. *Journal of Quaternary Science*, 18(5), 431-440.
- Humlum, O. (2000). The geomorphic significance of rock glaciers: estimates of rock glacier debris volumes and headwall recession rates in West Greenland. *Geomorphology*, 35(1), 41-67.
- Huss, M. (2013). Density assumptions for converting geodetic glacier volume change to mass change. *The Cryosphere*, 7(3), 877-887.
- Imbery, S. (2014). Development of a high resolution permafrost distribution model in the Aksu catchment, Central Tian Shan.
- IPCC. (2014). *Climate Change 2013: The Physical Science Basis. Contribution of Working Group I to the Fifth Assessment Report of the Intergovernmental Panel on Climate Change* (T. F. Stocker, D. Qin, G.-K. Plattner, M. Tignor, S. K. Allen, J. Boschung, A. Nauels, Y. Xia, V. Bex, & P. M. Midgley Eds.). Cambridge, United Kingdom and New York, NY, USA: Cambridge University Press.
- Iveronova, M. (1950). Kamennyye gletchery severnogo Tyan'-Shan [Rock glaciers in north Tien Shan]. *Inst. Geogr. Akad. Nauk SSSR, Trudy*, 45(1), 69-88.
- Jacob, T., Wahr, J., Pfeffer, W. T., & Swenson, S. (2012). Recent contributions of glaciers and ice caps to sea level rise. *Nature*, 482(7386), 514-518.
- Kääb, A. (1998). Rock glaciers Gruben, Muragl and Murtel, Switzerland: Area-wide flow fields. In: International Permafrost Association, Data and Information Working Group, comp. Circumpolar Active-Layer Permafrost

- System (CAPS), version 1.0. CD-ROM available from National Snow and Ice Data Center, nsidc@kryos.colorado.edu. Boulder, Colorado: NSIDC, University of Colorado at Boulder.
- Kääb, A. (2002). Monitoring high-mountain terrain deformation from repeated air- and spaceborne optical data: examples using digital aerial imagery and ASTER data. *ISPRS Journal of Photogrammetry and Remote Sensing*, 57(1), 39-52. doi:10.1016/S0924-2716(02)00114-4
- Kääb, A. (2005). *Remote sensing of mountain glaciers and permafrost creep* (Vol. 48): Geograph. Inst. d. Univ.
- Kääb, A., Frauenfelder, R., & Roer, I. (2007). On the response of rockglacier creep to surface temperature increase. *Global and Planetary Change*, 56(1-2), 172-187. doi:10.1016/j.gloplacha.2006.07.005
- Kääb, A., Haeberli, W., & Gudmundsson, G. H. (1997). Analysing the creep of mountain permafrost using high precision aerial photogrammetry: 25 years of monitoring Gruben rock glacier, Swiss Alps. *Permafrost and Periglacial Processes*, 8, 409-426.
- Kellerer-Pirklbauer, A., Lieb, G. K., & Kleinfierchner, H. (2012). A new rock glacier inventory of the eastern European Alps. *Austrian Journal of Earth Sciences*, 105(2), 78-93.
- Kinworthy, B. (2016). *New Mexico Rock Glacier Inventory: Analysis of Geomorphology and Paleogeography*.
- Kogutenko, L., Severskiy, I., Shahgedanova, M., Armstrong, R. L., Kokarev, A., Raup, B. H., ... & Kapitsa, V. (2015, December). Tuyuksu glacier as an indicator of change in the Zailiyskiy-Kungei Alatau glacial system during the last 60 years. In *AGU Fall Meeting Abstracts*.
- Krainer, K., & Ribis, M. (2012). A rock glacier inventory of the Tyrolean Alps (Austria). *Austrian Journal of Earth Sciences*, 105(2), 32-47.
- Kutuzov, S., & Shahgedanova, M. (2009). Glacier retreat and climatic variability in the eastern Terskey–Alatau, inner Tien Shan between the middle of the 19th century and beginning of the 21st century. *Global and Planetary Change*, 69(1), 59-70.
- Lehner, B., Verdin, K., Jarvis, A. (2008): New global hydrography derived from spaceborne elevation data. *Eos, Transactions, AGU*, 89(10): 93-94
- Leprince, S., Ayoub, F., Klinger, Y., & Avouac, J.-P. (2007). Co-Registration of Optically Sensed Images and Correlation (COSI-Corr): an operational methodology for ground deformation measurements. 1943-1946. doi:10.1109/igarss.2007.4423207
- Li, B., Zhu, A., Zhang, Y., Pei, T., Qin, C., & Zhou, C. (2006). Glacier change over the past four decades in the middle Chinese Tien Shan. *Journal of Glaciology*, 52(178), 425-432.
- Lucchitta, B., & Ferguson, H. (1986). Antarctica: measuring glacier velocity from satellite images. *Science*, 234(4780), 1105-1108.
- Marchenko, S. S. (2003a). *Borehole and active-layer monitoring in the northern Tien Shan (Kazakhstan)*. Paper presented at the Proceedings of the 8th International Conference on Permafrost, Zürich, Schweiz.
- Marchenko, S. S. (2003b). Kriolitozona Severnogo Tyan-Shanya: proshloe, nastoyaschchee, budushchee. *Permafrost of the Northern Tien Shan: past, present and future*. *Siberian Branch of Russian Academy of Sciences, Yakutsk*.
- Marchenko, S. S., Gorbunov, A. P., & Romanovsky, V. E. (2007). Permafrost warming in the Tien Shan Mountains, Central Asia. *Global and Planetary Change*, 56(3-4), 311-327. doi:10.1016/j.gloplacha.2006.07.023
- Maurer, J. M., Rupper, S. B., & Schaefer, J. M. (2016). Quantifying ice loss in the eastern Himalayas since 1974 using declassified spy satellite imagery. *The Cryosphere*, 10(5), 2203.
- McClellan, J. H., Schafer, R. W., & Yoder, M. A. (2003). *Signal processing first*. Pearson/Prentice Hall.
- Millar, C. I., & Westfall, R. D. (2008). Rock glaciers and related periglacial landforms in the Sierra Nevada, CA, USA; inventory, distribution and climatic relationships. *Quaternary International*, 188(1), 90-104.
- Ministry of Environment Protection. (2009). Kazakhstan's Second National Communication to the Conference of the Parties to the United Nations Framework Convention on Climate Change. Ministry of Environment Protection, Astana.
- Mukherjee, K., Bolch, T., Goerlich, F., Kutuzov, S., Osmonov, A., Pieczonka, T., & Shesterova, I. (2017). Surge-type glaciers in the Tien Shan (Central Asia). *Arctic, Antarctic, and Alpine Research*, 49(1), 147-171.
- Müller, J., Vieli, A., & Gärtner-Roer, I. (2016). Rock glaciers on the run—understanding rock glacier landform evolution and recent changes from numerical flow modeling. *The Cryosphere*, 10(6), 2865-2886.
- Narama, C., Kääb, A., Duishonakunov, M., & Abdrakhmatov, K. (2010). Spatial variability of recent glacier area changes in the Tien Shan Mountains, Central Asia, using CORONA (~1970), Landsat (~2000), and ALOS (~2007) satellite data. *Global and Planetary Change*, 71(1-2), 42-54. doi:10.1016/j.gloplacha.2009.08.002
- Necsoiu, M., Onaca, A., Wigginton, S., & Urdea, P. (2016). Rock glacier dynamics in Southern Carpathian Mountains from high-resolution optical and multi-temporal SAR satellite imagery. *Remote Sensing of Environment*, 177, 21-36.
- Niederer, P., Bilenko, V., Ershova, N., Hurni, H., Yerokhin, S., & Maselli, D. (2007). Tracing glacier wastage in the Northern Tien Shan (Kyrgyzstan/Central Asia) over the last 40 years. *Climatic Change*, 86(1-2), 227-234. doi:10.1007/s10584-007-9288-6

- Noetzli, J., Hoelzle, M., & Haeberli, W. (2003). *Mountain permafrost and recent Alpine rock-fall events: a GIS-based approach to determine critical factors*. Paper presented at the Proceedings of the 8th International Conference on Permafrost.
- Nuimura, T., Sakai, A., Taniguchi, K., Nagai, H., Lamsal, D., Tsutaki, S., ... & Tsunematsu, K. (2015). The GAMDAM glacier inventory: a quality-controlled inventory of Asian glaciers. *The Cryosphere*, 9(3), 849.
- Nuth, C., & Kääb, A. (2011). Co-registration and bias corrections of satellite elevation data sets for quantifying glacier thickness change. *The Cryosphere*, 5(1), 271-290. doi:10.5194/tc-5-271-2011
- Palgov, N. (1948). Bolshe almatinskij Uzel Oledenija v Khrebet Zailijskij Alatau (=Glaciation of the Bolshaya Almatinka junction in the Zailijskij Alatau mountain range). *Izvestija Akademija Nauk KazSSR, Geografija*, 58, 39–71.
- Paul, F., Barrand, N. E., Baumann, S., Berthier, E., Bolch, T., Casey, K., . . . Winsvold, S. (2013). On the accuracy of glacier outlines derived from remote-sensing data. *Annals of Glaciology*, 54(63), 171-182. doi:10.3189/2013AoG63A296
- Paul, F., Bolch, T., Kääb, A., Nagler, T., Nuth, C., Scharrer, K., ... & Berthier, E. (2015). The glaciers climate change initiative: Methods for creating glacier area, elevation change and velocity products. *Remote Sensing of Environment*, 162, 408-426.
- Pellicciotti, F., Stephan, C., Miles, E., Herreid, S., Immerzeel, W. W., & Bolch, T. (2015). Mass-balance changes of the debris-covered glaciers in the Langtang Himal, Nepal, from 1974 to 1999. *Journal of Glaciology*, 61(226), 373-386.
- Pieczonka, T., & Bolch, T. (2015). Region-wide glacier mass budgets and area changes for the Central Tien Shan between ~1975 and 1999 using Hexagon KH-9 imagery. *Global and Planetary Change*, 128, 1-13. doi:10.1016/j.gloplacha.2014.11.014
- Pieczonka, T., Bolch, T., & Buchroithner, M. (2011). Generation and evaluation of multitemporal digital terrain models of the Mt. Everest area from different optical sensors. *ISPRS Journal of photogrammetry and remote sensing*, 66(6), 927-940.
- Pieczonka, T., Bolch, T., Junfeng, W., & Shiyin, L. (2013). Heterogeneous mass loss of glaciers in the Aksu-Tarim Catchment (Central Tien Shan) revealed by 1976 KH-9 Hexagon and 2009 SPOT-5 stereo imagery. *Remote Sensing of Environment*, 130, 233-244. doi:10.1016/j.rse.2012.11.020
- Pfeffer, W. T., Arendt, A. A., Bliss, A., Bolch, T., Cogley, J. G., Gardner, A. S., Hagen, J.O., Hock, R., Kaser, G., Kienholz, C., & Miles, E. S. (2014). The Randolph Glacier Inventory: a globally complete inventory of glaciers. *Journal of Glaciology*, 60(221), 537-552.
- Potter, N. (1972). Ice-cored rock glacier, Galena Creek, northern Absaroka Mountains, Wyoming. *Geological Society of America Bulletin*, 83(10), 3025-3058.
- Pritchard, H. D., Luthcke, S., & Fleming, A. H. (2010). Understanding ice-sheet mass balance: progress in satellite altimetry and gravimetry. *Journal of Glaciology*, 56(200), 1151-1161.
- Pritchard, H. D. (2017). Asia's glaciers are a regionally important buffer against drought. *Nature*, 545(7653), 169-174.
- Racoviteanu, A. E., Paul, F., Raup, B., Khalsa, S. J. S., & Armstrong, R. (2009). Challenges and recommendations in mapping of glacier parameters from space: results of the 2008 Global Land Ice Measurements from Space (GLIMS) workshop, Boulder, Colorado, USA. *Annals of Glaciology*, 50(53), 53-69.
- Rangecroft, S., Harrison, S., & Anderson, K. (2015). Rock glaciers as water stores in the Bolivian Andes: an assessment of their hydrological importance. *Arctic, Antarctic, and Alpine Research*, 47(1), 89-98.
- Rangecroft, S., Harrison, S., Anderson, K., Magrath, J., Castel, A. P., & Pacheco, P. (2013). Climate change and water resources in arid mountains: an example from the Bolivian Andes. *Ambio*, 42(7), 852-863. doi:10.1007/s13280-013-0430-6
- Rangecroft, S., Harrison, S., Anderson, K., Magrath, J., Castel, A. P., & Pacheco, P. (2014). A first rock glacier inventory for the Bolivian Andes. *Permafrost and Periglacial Processes*, 25(4), 333-343.
- Rees, W. G. (2005). *Remote sensing of snow and ice*: CRC press.
- Rees, W. G., & Arnold, N. S. (2007). Mass balance and dynamics of a valley glacier measured by high-resolution LiDAR. *Polar Record*, 43(04), 311-319.
- Roer, I., Avian, M., Delaloye, R., Lambiel, C., Dousse, J., Bodin, X., . . . Damm, B. (2005). *Rockglacier "speed-up" throughout European Alps—a climatic signal*. Paper presented at the Proceedings of the second european conference on permafrost, Potsdam, Germany.
- Roer, I., Haeberli, W., Avian, M., Kaufmann, V., Delaloye, R., Lambiel, C., & Kääb, A. (2008). *Observations and considerations on destabilizing active rock glaciers in the European Alps*. Paper presented at the Ninth International Conference on Permafrost.
- Savoskul, O. S., & Smakhtin, V. (2013). *Glacier systems and seasonal snow cover in six major Asian river basins: hydrological role under changing climate* (Vol. 150). IWMI.

- Schmid, M. O., Baral, P., Gruber, S., Shahi, S., Shrestha, T., Stumm, D., & Wester, P. (2014). Assessment of permafrost distribution maps in the Hindu Kush–Himalayan region using rock glaciers mapped in Google Earth. *The Cryosphere Discussions*, 8(5), 5293–5319. doi:10.5194/tcd-8-5293-2014
- Schmidt, M., Goossens, R., & Menz, G. (2001). Processing techniques for CORONA satellite images in order to generate high-resolution digital elevation models (DEM). *Observing Our Environment from Space: New Solutions for a New Millennium*, 191–196.
- Scotti, R., Crosta, G. B., & Villa, A. (2016). Destabilisation of Creeping Permafrost: The Plator Rock Glacier Case Study (Central Italian Alps). *Permafrost and Periglacial Processes*. doi:10.1002/ppp.1917
- Seppi, R., Carton, A., Zumiani, M., Dall'Amico, M., Zampedri, G., & Rigon, R. (2012). Inventory, distribution and topographic features of rock glaciers in the southern region of the Eastern Italian Alps (Trentino). *Geografia Fisica e Dinamica Quaternaria*, 35, 185–197.
- Severskiy, I., Vilesov, E., Armstrong, R., Kokarev, A., Kogutenko, L., Usmanova, Z., ... & Raup, B. (2016). Changes in glaciation of the Balkhash–Alakol basin, central Asia, over recent decades. *Annals of Glaciology*, 57(71), 382–394.
- Sohn, H., Kim, G., Yom, J. (2004). Mathematical Modelling of Historical Reconnaissance Corona KH-4B imagery. *The Photogrammetric Record*, 19, 51–66.
- Solomina, O., Barry, R., & Bodnya, M. (2004). The retreat of Tien Shan glaciers (Kyrgyzstan) since the Little Ice Age estimated from aerial photographs, lichenometric and historical data. *Geografiska Annaler: Series A, Physical Geography*, 86(2), 205–215.
- Sorg, A., Bolch, T., Stoffel, M., Solomina, O., & Beniston, M. (2012). Climate change impacts on glaciers and runoff in Tien Shan (Central Asia). *Nature Climate Change*, 2(10), 725–731. doi:10.1038/nclimate1592
- Sorg, A., Kääb, A., Roesch, A., Bigler, C., & Stoffel, M. (2015). Contrasting responses of Central Asian rock glaciers to global warming. *Sci Rep*, 5, 8228. doi:10.1038/srep08228
- Strozzi, T., Caduff, R., Kääb, A., & Bolch, T. (2017, April). Inventory and state of activity of rockglaciers in the Ile and Kungöy Ranges of Northern Tien Shan from satellite SAR interferometry. In EGU General Assembly Conference Abstracts (Vol. 19, p. 13283).
- Takeuchi, N., Fujita, K., Aizen, V. B., Narama, C., Yokoyama, Y., Okamoto, S., . . . Kubota, J. (2014). The disappearance of glaciers in the Tien Shan Mountains in Central Asia at the end of Pleistocene. *Quaternary Science Reviews*, 103, 26–33. doi:10.1016/j.quascirev.2014.09.006
- Tedesco, M. (2014). *Remote sensing of the cryosphere*: John Wiley & Sons.
- Thurman, M. (2011). Natural disaster risks in Central Asia: a synthesis. Online source: <http://europeandcis.undp.org/uploads/public1/files/vulnerability/Senior, 20>.
- Toutin, T. (2004). Review article: Geometric processing of remote sensing images: models, algorithms and methods. *International Journal of Remote Sensing*, 25(10), 1893–1924.
- Unger-Shayesteh, K., Vorogushyn, S., Farinotti, D., Gafurov, A., Duethmann, D., Mandychev, A., & Merz, B. (2013). What do we know about past changes in the water cycle of Central Asian headwaters? A review. *Global and Planetary Change*, 110, 4–25. doi:10.1016/j.gloplacha.2013.02.004
- USGS. (2008). Declassified Intelligence Satellite Photographs (2008-3054). Retrieved from Reston, VA: <http://pubs.er.usgs.gov/publication/fs20083054>
- Wahrhaftig, C., & Cox, A. (1959). Rock glaciers in the Alaska Range. *Geological Society of America Bulletin*, 70(4), 383–436.
- Wang, X., Liu, L., Zhao, L., Wu, T., Li, Z., & Liu, G. (2017). Mapping and inventorying active rock glaciers in the northern Tien Shan of China using satellite SAR interferometry. *Cryosphere*, 11(2).
- Weng, Q. (2002). Quantifying uncertainty of digital elevation models derived from topographic maps. In *Advances in spatial data handling* (pp. 403–418). Springer Berlin Heidelberg.
- Westermann, S., Duguay, C. R., Grosse, G., & Kääb, A. (2015). Remote sensing of permafrost and frozen ground. *Remote Sensing of the Cryosphere*, 307–344.
- WGMS (2015, updated, and earlier reports): Global Glacier Change Bulletin No. 1 (2012–2013). Zemp, M., Gärtnner-Roer, I., Nussbaumer, S.U., Hüsler, F., Machguth, H., Mölg, N., Paul, F., and Hoelzle, M. (eds.), ICSU(WDS)/ IUGG(IACS)/ UNEP/ UNESCO/ WMO, World Glacier Monitoring Service, Zurich, Switzerland, 230 pp., publication based on database version: doi:10.5904/wgms-fog-2016-08.
- Wilson, R. (2015). *Quantifying Himalayan glacier change from the 1960s to early 2000s, using CORONA, glims and aster geospatial Data* (Doctoral dissertation, University of Salford).
- Wirz, V., Gruber, S., Purves, R. S., Beutel, J., Gärtnner-Roer, I., Gubler, S., & Vieli, A. (2016). Short-term velocity variations at three rock glaciers and their relationship with meteorological conditions. *Earth Surface Dynamics*, 4(1), 103–123. doi:10.5194/esurf-4-103-2016
- Zemp, M., Hoelzle, M., & Haeberli, W. (2009). Six decades of glacier mass-balance observations: a review of the worldwide monitoring network. *Annals of Glaciology*, 50(50), 101–111.

APPENDIX

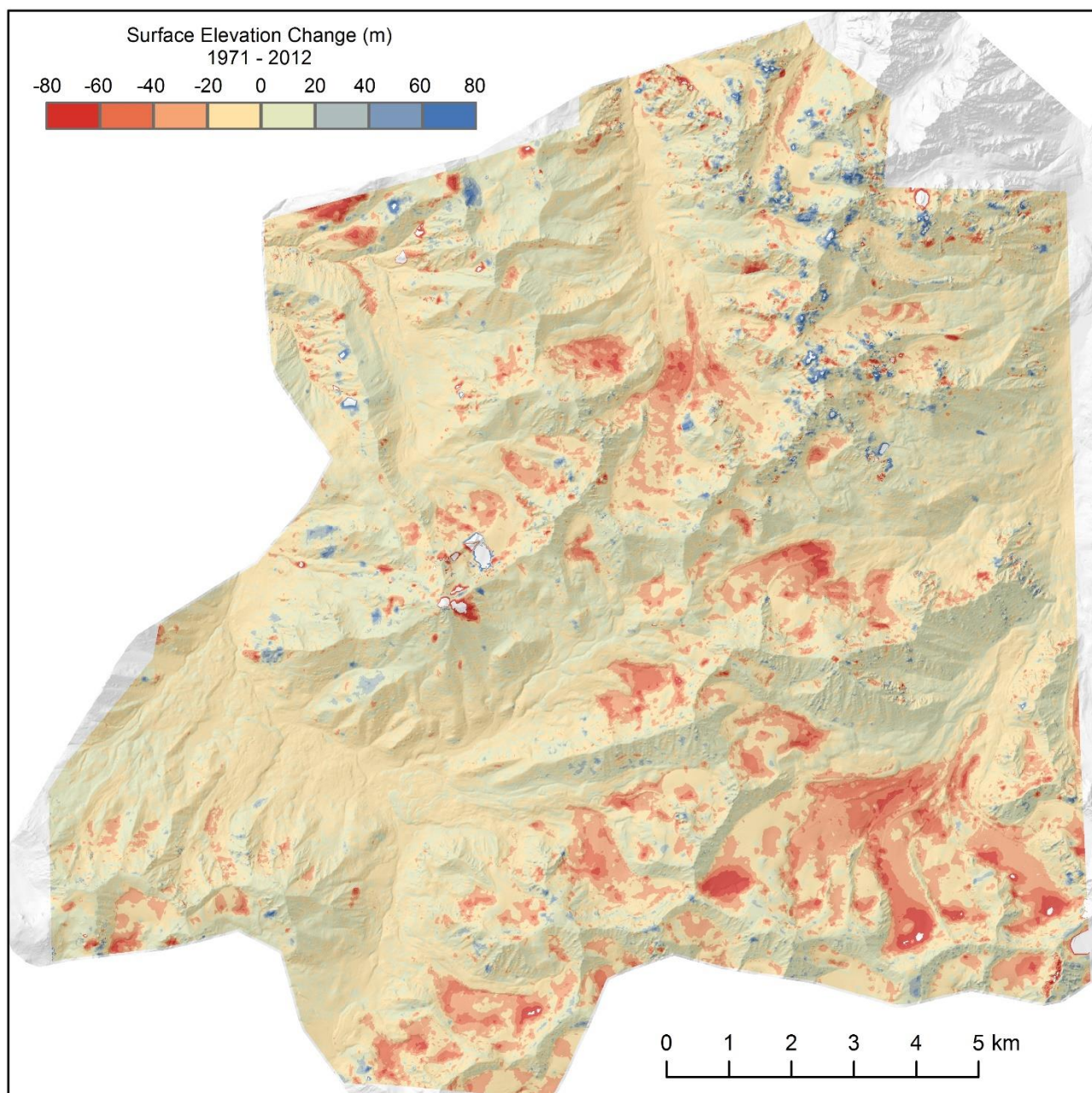


Figure A1: Surface elevation change (1971-2012).

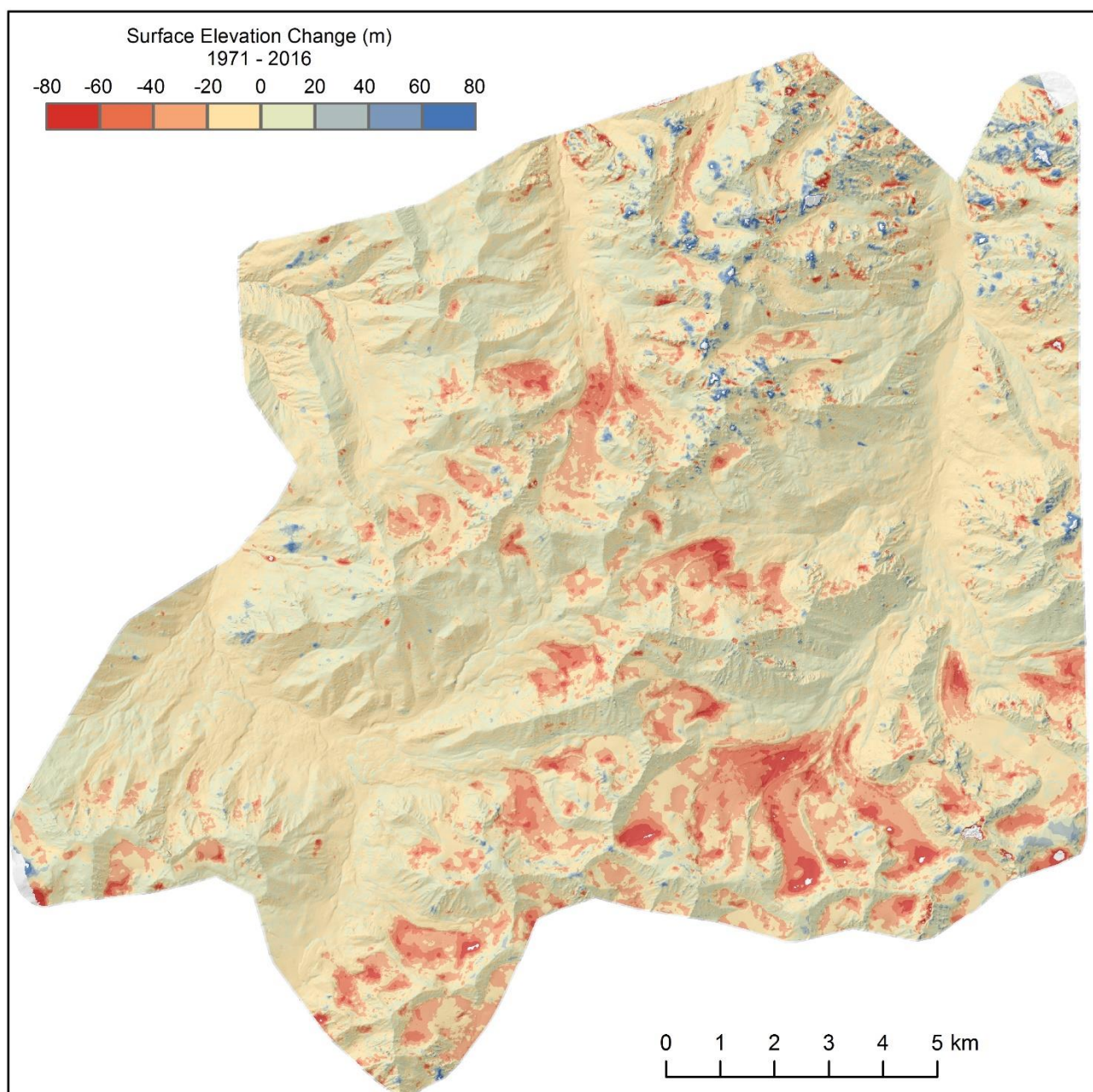


Figure A2: Surface elevation change (1971-2016).

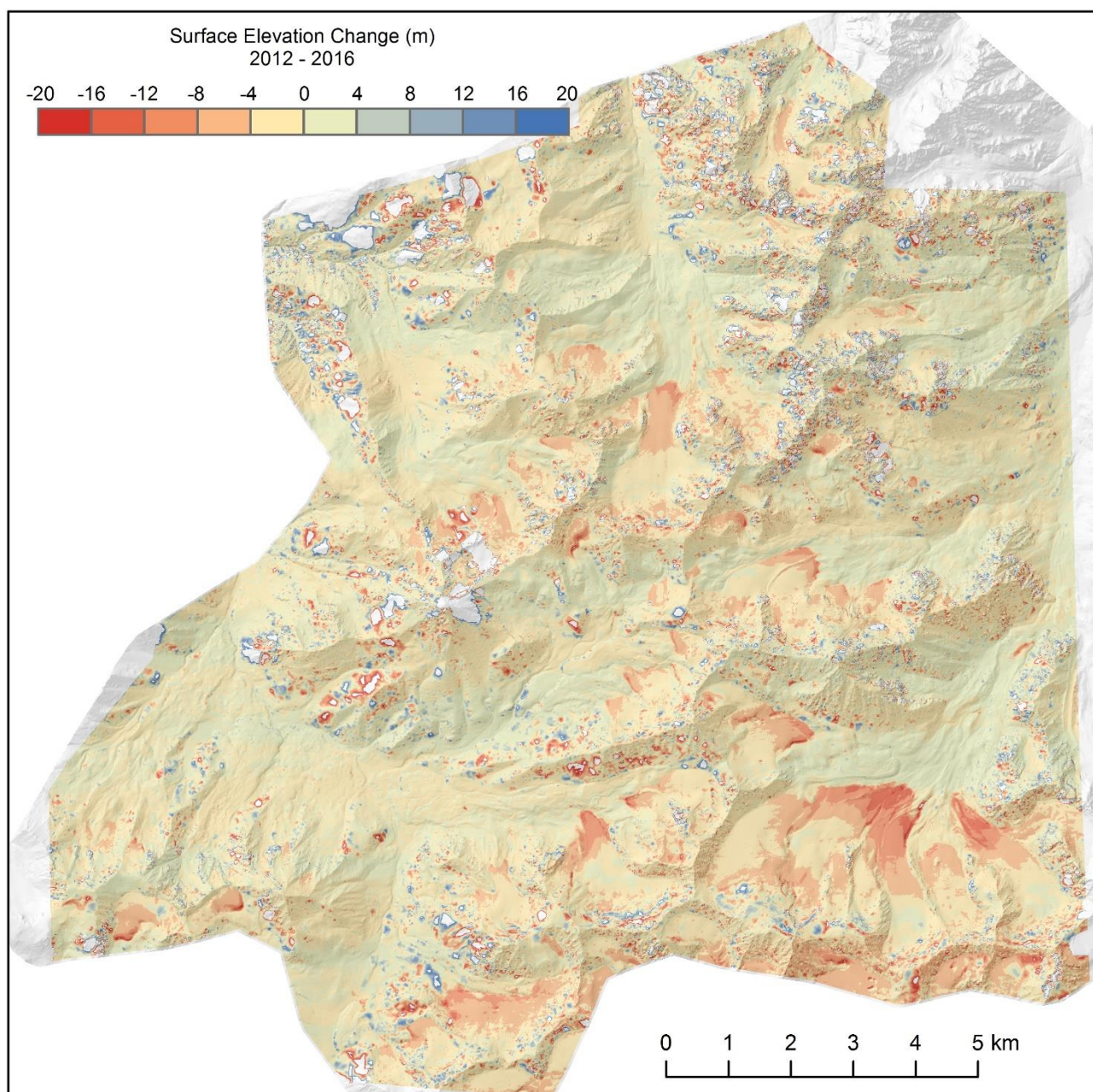


Figure A3: Surface elevation change (2012-2016).

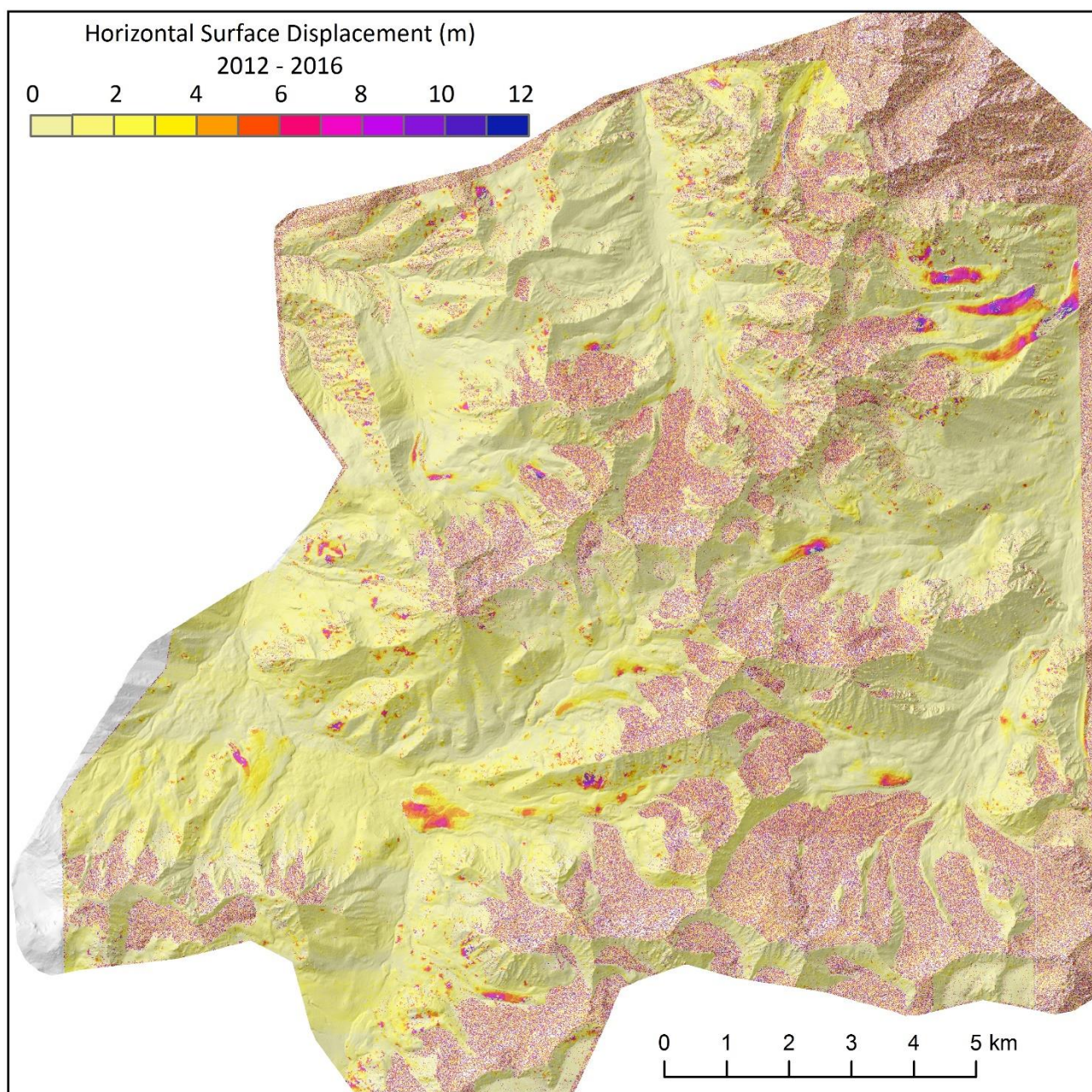


Figure A4: Horizontal surface displacements (2012-2016).

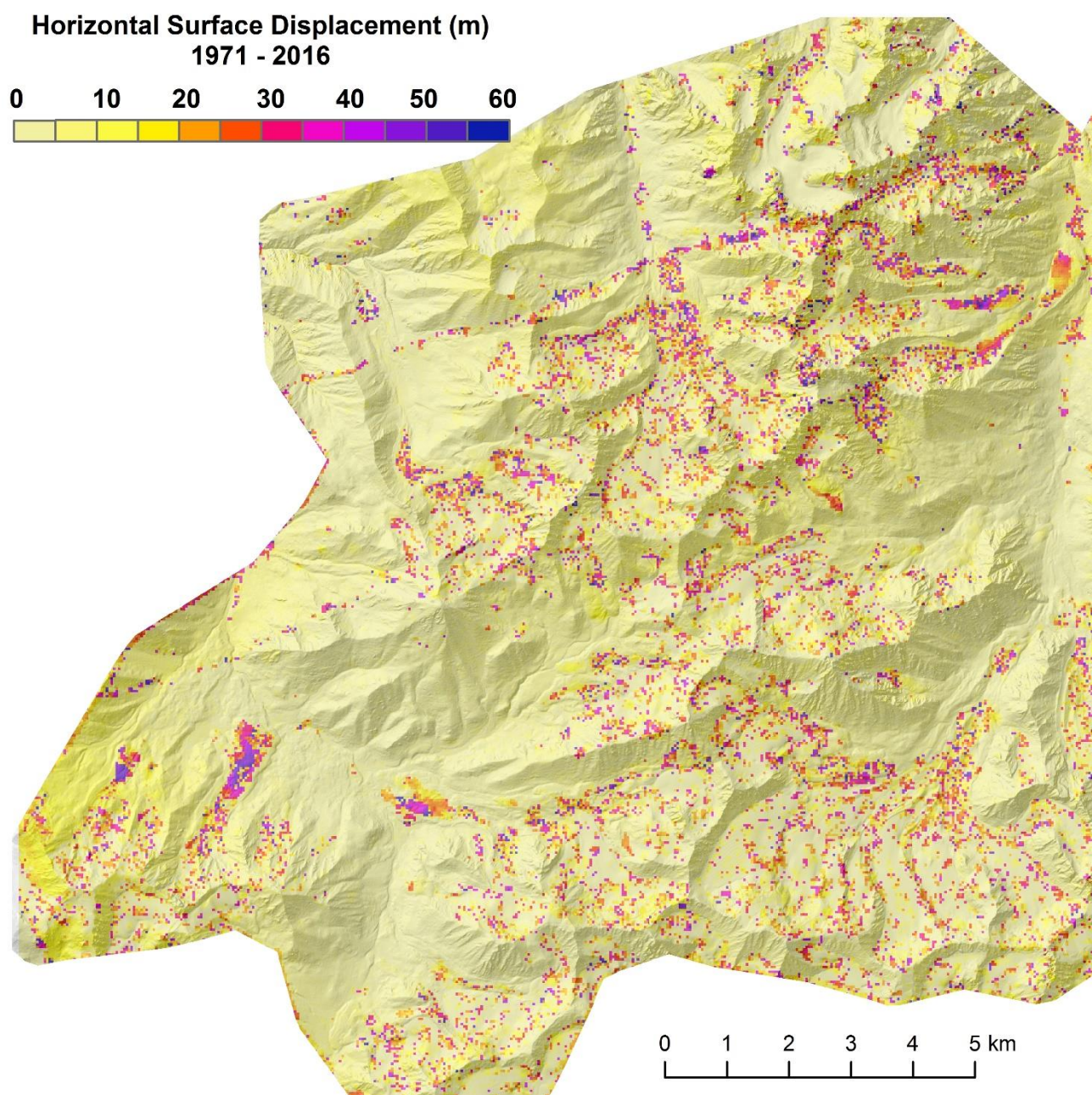


Figure A5: Horizontal surface displacements (1971-2016).